From the Institute of Experimental Cardiovascular Imaging, Institute for Molecular Cardiology at Heinrich Heine University Düsseldorf

Novel Biomarkers for the Outcome after Acute Myocardial Infarction

Dissertation

to obtain the academic title of Doctor of Philosophy (PhD) in Medical Sciences from the Faculty of Medicine at Heinrich Heine University Düsseldorf

Submitted by
Marwan Ahmed Ahmed Hamid
(2023)

My family

Zusammenfassung

Der ischämische Schaden, der während eines Myokardinfarkts (MI) auftritt, löst eine massive Immunantwort mit Induktion einer Notfall-Hämatopoese im Knochenmark aus. Dabei spielt das Mark der Röhrenknochen eine wichtige Rolle, aber auch das Brustbein ist blutbildend aktiv und liegt anatomisch in unmittelbarer Nähe zum Herzen. Dennoch wurde sein Beitrag zur Notfall-Hämatopoese nach MI bislang noch nicht untersucht. Hierfür untersuchten wir das Brustbein von Patienten mit ST-Strecken-Hebungs-Myokardinfarkt (STEMI) und in einem murinen MI-Modell mittels nicht-invasiver Magnetresonanztomographie (MRT) einschließlich kardialer Funktionsanalyse und parametrischer Kartierung (T1+T2). Unsere Daten zeigten einen signifikanten Anstieg des sternalen T2 an Tag 1 nach STEMI, der an 5. Tag wieder abnahm und sich während der Nachbeobachtung von 6 Monaten nahezu den Werten gesunder Kontrollpersonen näherte. Die MI-Induktion im Mausmodell führte zu ähnlichen Ergebnissen mit einem Anstieg des sternalen T2 an Tag 1 nach MI. Wichtig ist, dass dieser Anstieg von T2 spezifisch für das sternale Knochenmark war, da eine parallele Messung der Tibia das gegenteilige Verhalten zeigte. Dies spiegelte sich auch in durchflusszytometrischen Analysen des Neutrophilengehalts wider. Während die Tibia erst 1 Tag nach MI eine signifikante Freisetzung von Neutrophilen zeigte, war die entsprechende Reaktion des Brustbeins bereits nach 3 Stunden detektierbar. Mittels $^{1}H/^{19}F$-MRT konnte parallel dazu gezeigt werden, dass die ^{19}F-Markierung von Neutrophilen im Brustbein vor MI bei einer erneuten Untersuchung nach MI ein deutliches ^{19}F-Signal im Herzen ergab, das exakt mit dem LGE-positiven Myokard übereinstimmte. Bei weiterer Analyse der Humandaten stellten wir einen Trend zu einer positiven Korrelation von T2 mit der Menge zirkulierender Neutrophilen 1 Tag nach STEMI fest, was darauf hindeutet, dass sich der Grad der sternalen Notfall-Hämatopoese in einer Veränderung von T2 widerspiegelt. Darüber hinaus zeigte der Fettgehalt eine umgekehrte Korrelation mit T2, was höchstwahrscheinlich auf einen erhöhten Substratverbrauch im Zusammenhang mit der Stimulierung der Hämatopoese zurückzuführen ist. Hinsichtlich des kardialen Remodellings beobachteten wir eine signifikante negative Korrelation mit T2 1 Tag nach STEMI und je größer der T2-Abfall von Tag 1 bis Tag 5, desto geringer war der Grad des Remodelling. Insgesamt deuten unsere Ergebnisse darauf hin, dass eine starke, frühzeitige Aktivierung der sternalen Notfall-Hämatopoese zur zügigen Entfernung von Zelldebris und deren anschließende schnelle Deaktivierung sich positiv auf das Remodelling des menschlichen Herzens nach STEMI auswirkt. Ob diese Effekte durch eine verstärkte Freisetzung von z.B. Neutrophile aus dem

Brustbein in den Kreislauf und/oder durch direkten Transport dieser Zellen in das verletzte Herz vermittelt sind, muß in zukünftigen Studien untersucht werden.

Summary

The extensive ischemic injury that occurs during myocardial infarction (MI) triggers a massive immune response with induction of emergency hematopoiesis in the bone marrow. For this, the marrow of the long bones is expected to play a major role, but also the sternum is haematopoietically active and anatomically in close vicinity to the heart. Nevertheless, its exact contribution to this process has not yet been investigated. To address this question, we investigated the sternum in patients with ST-segment elevation myocardial infarction (STEMI) and a murine model of MI by non-invasive Magnetic Resonance Imaging (MRI) including analysis of cardiac and parametric mapping (T1+T2). Our data showed a significant increase in sternal T2 at 1 day after STEMI, which decreased again at day 5 and continued to approach nearly baseline values of healthy controls during a follow-up of 6 months. Experimental induction of MI in the murine model resulted in similar findings with an increase of sternal T2 at day 1 after MI. Importantly, this rise in T2 was specific for the sternal bone marrow, since parallel measurement of the tibia demonstrated the opposite behavior. As expected, neutrophil levels in humans were elevated at day 1 post-STEMI which also normalized over time, and the differential behavior of the distinct hematopoietic niches was also reflected in flow cytometric analyses of their neutrophil content in mice. Whereas the tibia did not show significant neutrophils release until 1 day after MI, the corresponding response of the sternum was detectable as early as 3 hours after MI. Using $^{1}H/^{19}F$ MRI, it could be demonstrated that ^{19}F labeling of neutrophils in the sternum prior MI, on re-examination after induction of MI resulted in a clear ^{19}F signal within the heart, which exactly matched the LGE-delineated myocardium. In further investigation of the human data, we found a trend towards a positive correlation of T2 with the amount of circulating neutrophils 1 day after STEMI suggesting that the degree of sternal emergency hematopoiesis is mirrored by alteration in T2. Furthermore, fat content revealed an inverse correlation with T2, this most likely reflects an enhanced substrate consumption associated with the stimulation of hematopoiesis. For the degree of heart remodeling we observed a significant negative correlation with T2 1 day after STEMI with the higher sternal T2 and the larger its drop from day 1 to day 5, the less the adverse remodeling. Overall, our results suggest a strong early activation of sternal emergency hematopoiesis for quick removal of debris and its subsequent rapid de-activation as beneficial for the remodeling of the human heart after STEMI. Whether these effects are mediated via an enhanced release of e.g. neutrophils from the sternum into the circulation and/or by direct trafficking of these cells into the injured heart has to be investigated in future studies.

List of Abbreviations

^{19}FMRI	Fluorine magnetic resonance imaging
AMI	Acute myocardial infarction
ApoE	Apolipoprotein E
BM	Bone marrow
CADs	Coronary artery diseases
CAM	Cell adhesion molecular
CK	Creatine kinase
CRP	C-reactive protein
Ctl	Control
CVD	Cardiovascular disease
ECG	Electrocardiogram
FACs	Fluorescence activated cells sorting
HF	Heart failure
HR	Heart Ratio
hs-cTnl	Highly sensitive cardiac troponin I
hs-cTnT	Highly sensitive cardiac troponin T
HV	Healthy volunteers
I/R	Ischemic/Reperfusion
IHDs	Ischemic heart diseases
IMH	Intramyocardial hemorrhage
IS	Infarction size
ko	knockout
LAD	Left anterior descending artery
LDL	low-density lipoprotein
LGE	Late gadolinium enhancement

LV	Left ventricular
LSB	Left bundle branch
LVED	End-diastolic volume
LVEF	Left ventricular ejection fraction
LVESV	Left ventricular end-systolic volume
LVESVi	Index left ventricular end-systolic volume
mg	Milligram
MI	Myocardial infarction
MRA	Magnetic resonance angiography
MRI	Magnetic resonance Imaging
MRII	Cardiac magnetic resonance imaging
MVO	Microvascular obstruction
NSTEMI	Non-ST segment elevation myocardial infarction
PCI	Percutaneous coronary intervention
PFCs	Perfluorocarbon nanoemulsions
RBM	Red bone marrow
RT	Relaxation time
ROI	Region of interest
S.c	Subcutaneous
SCADs	Patients with stable coronary diseases
SD	Standard deviation
SV	Stroke volume
SI	Size intensity
SVi	Stroke volume index
STEMI	ST-elevation myocardial infarction
UKD	University clinic of Dusseldorf

WBC	White blood cell
WD	Western diet
WT	Wild type
YBM	Yellow bone marrow
ZETT	Central institution for animal research and animal welfare tasks

List of Figures

List of Tables

Table of Contents

1. Introduction

1.1. Overview of cardiovascular diseases

Cardiovascular disease (CVDs) can be inherited or acquired and represents statistically the leading cause of morbidity and mortality of around 17.8 million people in 2017 in the overall world [1]. It is predicted that in 2030 the number will reach over 24 million cases [2]. CVDs are involved in a variety of pathological conditions [3] affecting the heart and blood vessels, and cause death more than the next six causes of death combined (i.e accidents, cancer, Alzheimer, diabetes, chronic lower respiratory diseases) [4]. Different risk factors for CVDs like age, and genetic or age as well as modifiable factors such as lifestyle, hyperlipidemia, smoking, or physical inactivity. Coronary artery diseases (CADs) or ischemic heart diseases (IHDs) arise due to a reduction of blood flow in the coronary arteries and represent the deadliest form. The blockages or narrowing in the coronary artery cause an insufficient oxygen and nutrient supply of the myocardium or ischemia0[6]. A myocardial infarction (MI) is the consequence of 20 to 30 minutes of ischemia [7]. MI induces cardiac cell death and heart tissue gets more necrotic and severe damage. Depending on the area affected such an event can lead to death or contributes to complications like cardiogenic shock, myocardial rupture, or heart failure [8]. Left ventricular (LV) remodeling after acute MI (AMI) promotes a shortage in body metabolic demands as a result of an ischemic injury that in most cases develops into heart failure [9]. Despite myocardial muscle having some regenerative capacity and advanced therapy for MI many surviving patients still develop ventricular integrity, electrical uncoupling, cardiac arrhythmias, ventricular dysfunction, and ultimately cardiomyopathy.

The most common cause of CVDs is the development of atherosclerosis, which begins years before and is characterized by the enrichment of lipids and fibrous particles in large and medium-sized arteries [10,11]. Atherosclerosis starts in an initial phase, in which the tunica intima, the inner lining of the arteries gets irritated and damaged, mostly due to risk factors like smoking, hypertension, hyperglycemia, or hyperlipidemia [12]. The resulting endothelial cell damage and dysfunction facilitate the permeability and accumulation of plasma components like low-density lipoprotein (LDL) [13]. As the incidence and mortality rate of CVDs is practically high and will still rise in the next years, research in this field is of main relevance for the entire society. To study the outcomes or the influences of an acute MI, different MI models were generated, in which the LAD is

temporarily or permanently occluded [14]. Similar to the human situation, mice own two coronary arteries, the RCA and LCA, which are comparable branches [15]. In mice, the LAD is the easiest accessible coronary artery for surgeries and is also the most blocked artery in humans.

1.2. ST-elevated myocardial infarction

1.2.1. Pathophysiology and ECG diagnostic

According to the various pathophysiological mechanisms that can lead to an acute myocardial infarction, a distinction is made between different types of heart attack [16]:

- Type 1: Atherosclerotic plaque rupture with coronary thrombosis
- Type 2: Myocardial oxygen deficit
- Type 3: Cardiac death
- Type 4: PCI-associated
- Type 5: Bypass associated

Studies have shown that 84.6% of myocardial infarctions can be traced back to type 1 of infarction [17]. The blockages vary between the branches of the coronary arteries and the LAD is the most affected one as it is blocked in around 50% of cases [18]. Many symptoms attended with MI like chest pain, shortness of breath, sweating, nausea, fatigue, anxiety, and electroheart singal changes can be detected by an electrocardiogram (ECG) [19]. Thereby, it can be distinguished between a STEMI (ST-segment elevation myocardial infarction) or NSTEMI (non-ST-segment elevation myocardial infarction). STEMI is the most acute manifestation of coronary artery disease and is associated with great morbidity and mortality. The presence of a STEMI results from a complete thrombogenic blockage of a coronary artery (type 2) and is characterized by an ST-segment elevation higher than the baseline signal [19]. The predominant underlying mechanism of total coronary occlusion in STEMI is thrombosis developing on a coronary atherosclerotic plaque [20] and a few exceptions exist including spontaneous coronary artery dissection, coronary spasm, and coronary embolism [21]. In contrast, NSTEMIs do not show this typical elevation, moreover, they represent a depression, which can be explained by an incomplete blockage of the coronary artery or the occurrence of a coronary artery spasm [21,22].

Time delay to treatment is a relevant factor that greatly affects mortality in patients with STEMI; thus, early diagnosis is crucial. The working diagnosis is usually based on symptoms consistent with myocardial ischemia, that is persistent chest pain and new ST-segment elevation. If a heart attack is suspected, the field transmission of the ECG is recommended, first technical examination is to secure the diagnosis. If ECG interpretation is not possible on-site, the registration of a pre-hospital ECG improves clinical outcomes and time to reperfusion, particularly when coupled with communication of a STEMI diagnosis. In contrast to STEMI, the ECG in the NSTEMI is less specific. The diagnosis of STEMI can be particularly difficult in the presence of left ventricular hypertrophy, ventricular paced rhythm, and early repolarization patterns because these conditions interfere with classic ST-segment elevation patterns in the ECG. For the STEMI, the localization of the ST elevations in the ECG indicates the affected area of myocardial infarction (anterior, lateral, or posterior war). Early diagnosis and immediate reperfusion are the most effective ways to limit MI and infarct size and thereby reduce the risk of post-STEMI complication and heart failure [18].

1.2.2. Laboratory diagnostic

The main indicator of the destruction of heart muscle tissue is the release of myocardial infarction-specific heart proteins, which can be detected diagnostically in the blood. The most important acute marker is the cardiac troponin [23], which consists of the subunits T, I, or C. Due to their specificity in the heart muscle, the highly sensitive cardiac troponin T and I (hs-cTnT & hs-cTnl) for short should be emphasized here. The hs-cTnT is about 3-4 hours after the onset of infarction symptoms detectable [24]. The less specific indicators of myocardial damage are creatine kinase and myoglobin not listed further for the reason of clarity [25]. However, the biomarkers mentioned do not play a diagnostic role in the setting of unequivocal STEMI, since waiting for laboratory values would delay timely myocardial revascularization [26].

1.2.3. Clinic

The occurrence of myocardial ischemia results from an imbalance between oxygen supply and demand. In a clinical setting, MI can usually be identified based on clinical factors and ECG. The sudden onset of retrosternal chest pain lasting more than 20 minutes is typical of an acute coronary syndrome; often accompanied by vegetative symptoms such as nausea and cold sweat. Depending on the course, dyspnea, shock (hypotension and tachycardia), and restlessness are important accompanying symptoms [27]. Epigastric abdominal pain is characteristic of inferior posterior wall infarcts. Particular attention should be paid to

atypical symptoms, due to polyneuropathy, diabetics often do not feel any chest pain, which is why the working diagnosis of myocardial infarction can be overlooked. Women also represent a diagnostic risk population. It is not uncommon for MI with purely vegetative symptoms to appear, here are the most common STEMI characteristics:

- Heart attack symptoms lasting more than 20 minutes
- Specific ECG changes
- Positive troponin diagnostic

Patients with suspected acute coronary syndrome, in whom MI has been ruled out and who also have normal cardiac biomarkers, may have unstable angina or another diagnosis [28].

1.3. Inflammation markers

Acute myocardial infarction (AMI), especially STEMI and NSTEMI, results in the elevation of specific cardiac biomarkers [29]. The molecules or proteins including troponin, C-reactive protein (CRP), creatine kinase (CK), and others [30] in general blood circulation are markers of cardiotoxicity that have been studied in the context of myocardial infarction. They are integral to the diagnosis of MI and heart failure and elevations in these biomarkers have been demonstrated during and after MI [31] and many potential sources of inflammatory factors as well as cytokines that promote their products. Most include serum amyloid (IL-6 and PCT) and C-reactive protein (CRP) [32], which are very responsive and sensitive to the acute phase of the nonspecific phenomenon of low-grade systemic inflammation. Another source of inflammatory markers is the innate immune system (macrophages and related cells), for example, monocytes [33] including phospholipase A2, which stimulate the synthesis of platelet-activating factor, and neutrophils, which are considered the most and first arrival to the site of inflammation. Endothelial and vascular smooth muscle cells (the arterial wall itself) can be a source of inflammatory markers [34], including cell adhesion molecular family (CAMs), the distal indicator of inflammation [35]. In the context of heart injury, biomarkers can inform the diagnosis in patients with suspected MI and can confirm whether the presence or absence of inflammation in active myocardial tissue has not been established so far [36]. However, there is a knowledge gap on how the inflammatory milieu after AMI affects the outcome of patient and infarct characteristics, which hampers the identification of a biomarker for myocardial infarction that can inform the diagnosis in patients with suspected STEMI and help to determine the presence of active MI. Many studies [33-42] have demonstrated that blood biomarkers (such as troponin [43,44]) may not always be the most suitable candidate

by demonstrating that it is possible for it to rise independently of cardiotoxicity.

1.4. Heart remodeling

Despite modern reperfusion strategies [41], the damage caused by myocardial ischemia leads to left/right ventricular geometric adaptation (i.e. remodeling). This process involves changes in heart geometry, size, and function and can eventually lead to heart failure [42]. Left ventricular (LV) remodeling after MI is characterized by progressive dilatation, hypertrophy, and deterioration in contractile function [9]. In the early phase, the non-infarcted region also undergoes significant remodeling associated with secondary volume overload hypertrophy, which may be progressive. The extent of ventricular dilatation after infarction is related to the extent of initial myocardial damage and is associated with a worsened prognosis [43]. After MI, the development and stimulation of collagen-producing myofibroblasts lead to progressive fibrosis. The stretching and thus loading of the myocardial fibers and the presence of inflammation are essential factors for the activation of the myofibroblasts. The regulation of the inflammatory response is a finely tuned process since fibrosis is required for adequate scar formation, but excess leads to cardiac rigidity, which impairs oxygen diffusion and thus impedes adequate oxygenation [44]. In the context of remodeling, inflammation with activation of immune cells (derived from bone marrow) after MI plays a central role [45]. After MI, there is regional inflammation with a functionally meaningful correlation to edema, infarct size, microvascular obstruction, intramural hemorrhage, and regional and global LV function [46]. Peak levels of the inflammatory parameters predict the onset of heart failure in STEMI patients and are also a strong predictor of global and cardiovascular mortality in the following years after STEMI [47].

1.5. Bone marrow system

Bone marrow (BM) is a semi-solid tissue with highly vascular components that reside in bone cavities and mainly produces blood cells, while marrow adipocytes store significant quantities of fat. The structure of BM [48] is separated into 2 types of components: vascular and non-vascular [49]. The vascular component contains a large number of vessels to supply nutrients and transport blood cells from and into circulation [50]. The non-vascular is mainly responsible for immune cells (hematopoiesis) formation and contains fat cells, red blood cells, white blood cells, and branching fibers of connective tissue [51]. All blood cells are derived from bone marrow and some of them mature in the spleen [52], thymus gland [53], and lymph nodes. The main function of bone marrow is to produce and form immune cells. Bone marrow contains hematopoietic stem cells, which exist in red marrow

and are responsible for the formation and renewal of blood circulation. Also, bone marrow contains mesenchymal stem cells [54], which produce the non-blood cell components of marrow such as fat, cartilage, fibrous connective tissue, stromal cells, and bone cells.

1.5.1. Microenvironment of bone marrow

Bone marrow contains yellow (fatty) and red marrow. Fatty marrow consists of fat cells and inactive tissue, which has a poor vascular supply. The main function of yellow marrow is to store fats and to act as a regulator to maintain the correct environment for bone function [55]. In adults, fatty marrow tends to be located in spongy bones, particularly in the shaft of long bones [56] and it can be converted to red marrow in order to produce more blood cells such as with severe blood loss. In contrast, red marrow mostly exists in the skull, pelvis, spine, ribs, sternum, shoulder blades, and points between arms and legs [57]. It produces all red blood cells, platelets, and 60-70 % of lymphocytes and also removes the old cells from circulation. Red blood cells (or erythrocytes) mainly transport oxygen and deliver carbon dioxide from all cells to the lungs. Platelets or thrombocytes convert to megakaryocytes and break into fragments to form platelets, their main function is blood clotting and tissue healing. White blood cells or myeloblast granulocytes develop from myeloblast cells (including neutrophils, eosinophils, and basophils), these immune cells (Figure 1) defend the body from invaders (viruses, bacteria, and other pathogens) and also get active during allergic reactions [58]. Monocytes (the largest white blood cells) migrate from blood to damaged tissues and develop into dendritic and macrophage cells. They clear dead cells from damaged tissues, remove foreign substances, and phagocytose cancer cells from the body [59]. Antigen immunity can be developed by dendritic cells which present information to lymphocytes. Also, they initiate a primary immune response, commonly found in the respiratory tract, skin, and gastrointestinal tract. Mast cells (white blood cells granulocytes) can develop independently from myeloblast cells [60].

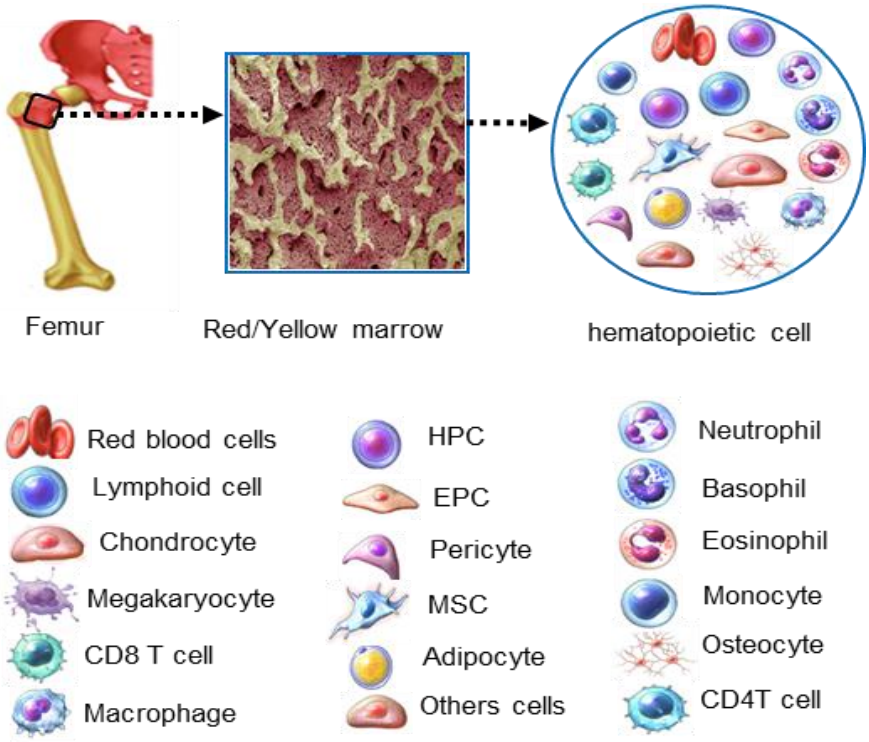

Fig. 1: Bone marrow microarchitecture. Bone marrow is a primary site of immune cells. On the left, a longitudinal view of an adult femur illustrates the arrangement of red and yellow marrow. On the middle, anterior view of immune cells as a result of the hematopoiesis process in the bone marrow to release myeloid progenitor cells into circulation. On the right, several hematopoietic cell types are regulated by bone marrow activity.

They exist throughout body tissues, specifically in the lining of the digestive system and skin. They mediate immune response by releasing chemicals (such as histamine) that primarily serve to heal wounds. Also, they involve in blood vessel generation and allergic diseases (such as eczema, asthma, and some others) [61]. The innate immune cells are mainly regulated by lymphoid stem cells which develop into lymphoblast cells. They produce lymphocytes (white blood cells) including B lymphocytes, T lymphocytes, and natural killer cells. They are responsible for pathogens, and tumor development, and destroy damaged or cancerous cells and infected cells [62].

1.5.2. Dynamic of bone marrow

Bone marrow is the mother bed of immune cells [63], it can be found in almost any bone that holds cancellous or spongy tissue [64]. During childhood (1-5 years), all bones are filled exclusively with red marrow, as we age it is mostly replaced by fatty marrow (yellow), as shown in Figure 2. This dynamic natural conversion of red into yellow marrow [65] can last until adulthood as a gradually, predictable pattern in the whole skeleton as well as in individual bones [66]. Conversion starts from the limbs proximally to the axial skeleton and is completed by the age of 25 years.

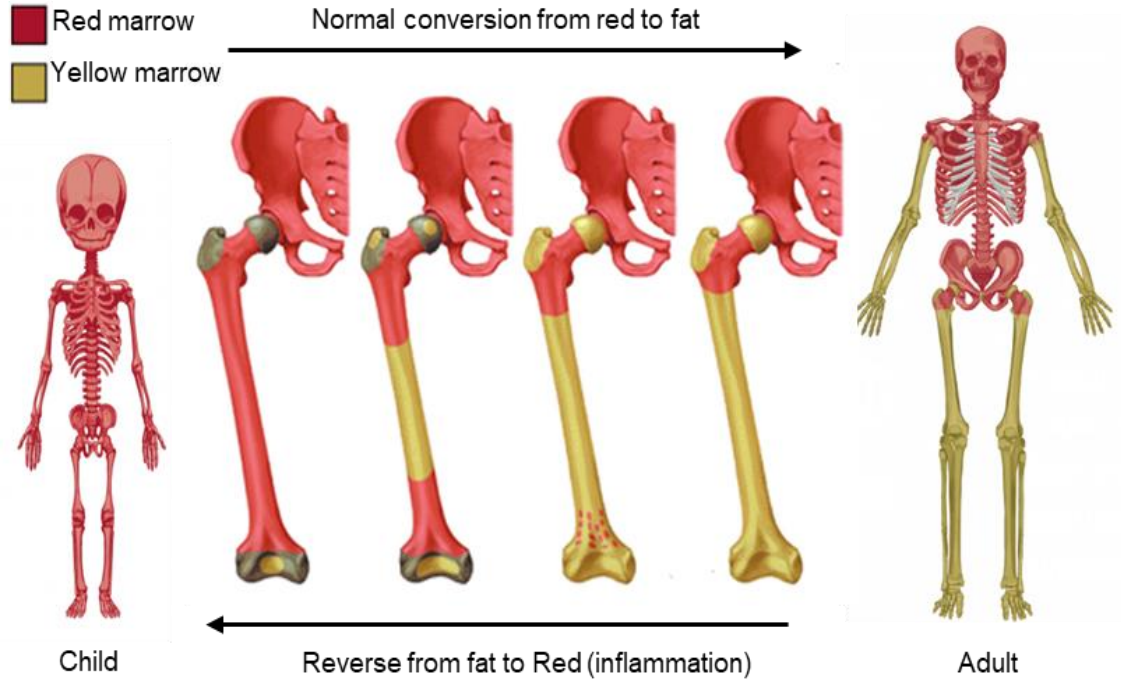

Fig. 2: Dynamic conversion of bone marrow. Throughout life, red marrow (hematopoietic cells) is constantly covered into yellow marrow (adipocytes) in the whole skeleton as well as in individual bones. This process of conversion begins early in life and generally occurs in a centripetal pattern, beginning in the distal bones. Expectedly, fatty marrow can reverse and become cellular during inflammation to when the body demands

Red marrow or Medulla ossium consists mainly of hematopoietic tissue (red blood cells, platelets, and other cells) [67] and can be found in the bones of ribs, sternum, vertebrae, the pelvic as well as some parts of the femur. Medulla ossium *flava* or yellow marrow is mainly made up of fat cells [68] and mostly exists in long bones. The normal conversion of bone marrow is from red to fatty marrow throughout aging, but the reverse process of the natural replacement can occur when the body demands it. That developed fatty marrow over time (Figure 2) can be reconverted to red marrow (hematopoietic cells) to produce immune cells to supply the needs of the body during schematic injuries and other inflammations [69].

1.5.3. Sternum bone marrow

Sternum is the flat bone that lies vertically in the median and anterior part of the thorax, between the connected pairs of ribs. Due to the articulated connections to the ribs, the sternum stabilizes the thorax and at the same time provides flexibility and mobility in breathing. In the adult human, the sternum has three main parts: the manubrium, the body of the sternum, and the xiphoid process [70]. In mouse, the sternum starts from the manubrium [71], in the middle contains the sternerbra (several segments), and ends with the xiphoid process, as in Figure 3.

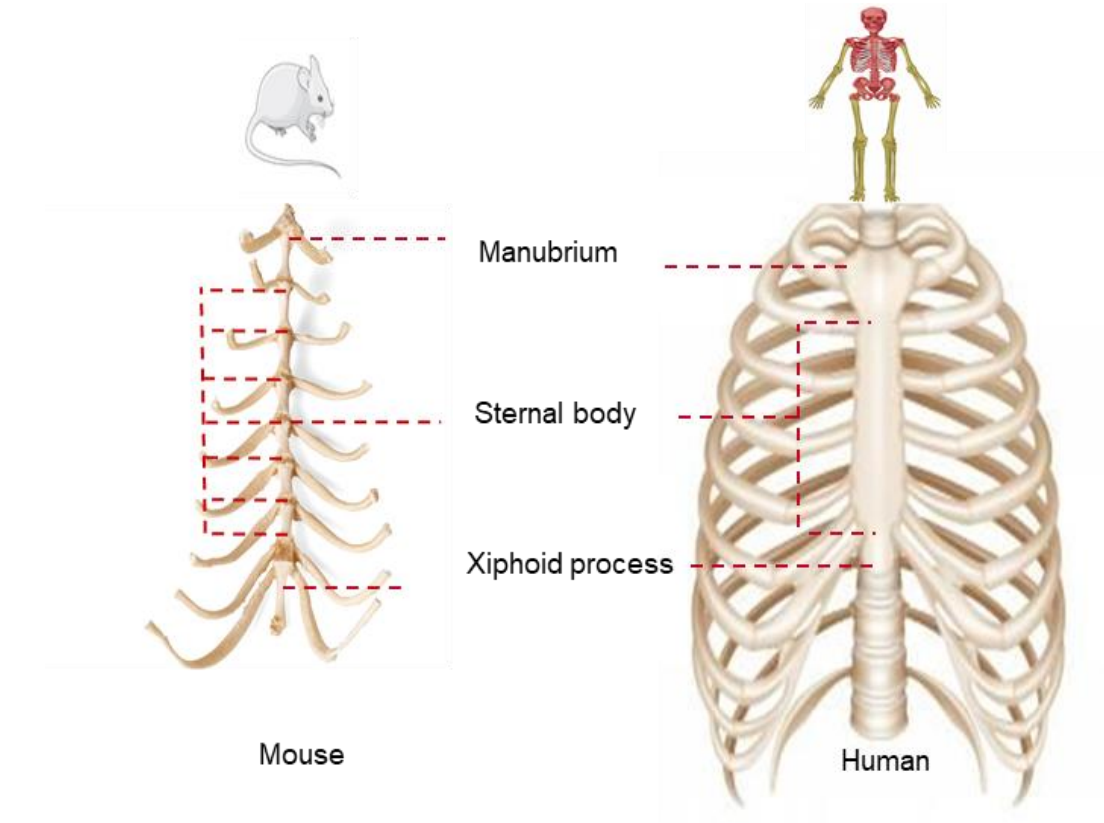

Fig. 3: Structure of sternum in mouse and human. The main parts of the sternum are the manubrium, body of the sternum, and the xiphoid process. On the left, the sternum in mice is segmented into many parts, which are distributed throughout the all sternum bone marrow. On the right, the sternum in humans is divided into three segments, usually connected to each other with aging.

The hematopoietic system, with its ability to produce an estimated half a trillion new cells per day in humans [72], is arguably the most prolific in a body, but the sternum remains cellular during aging [73] as shown in Figure 4. The entire bone marrow system supports the formation of immune cells, but sternum, cranium, ribs, and vertebrates, as well as ilium, are the major hematopoietic sites.

Functional and transcriptomic studies demonstrated the importance of bone marrow metabolic processes [74]. Most of the time bone marrow is quiescent, which protects it against proliferative and genotoxic stress effects harmful to the bone marrow system while allowing it to maintain its self-renewal potential [75].

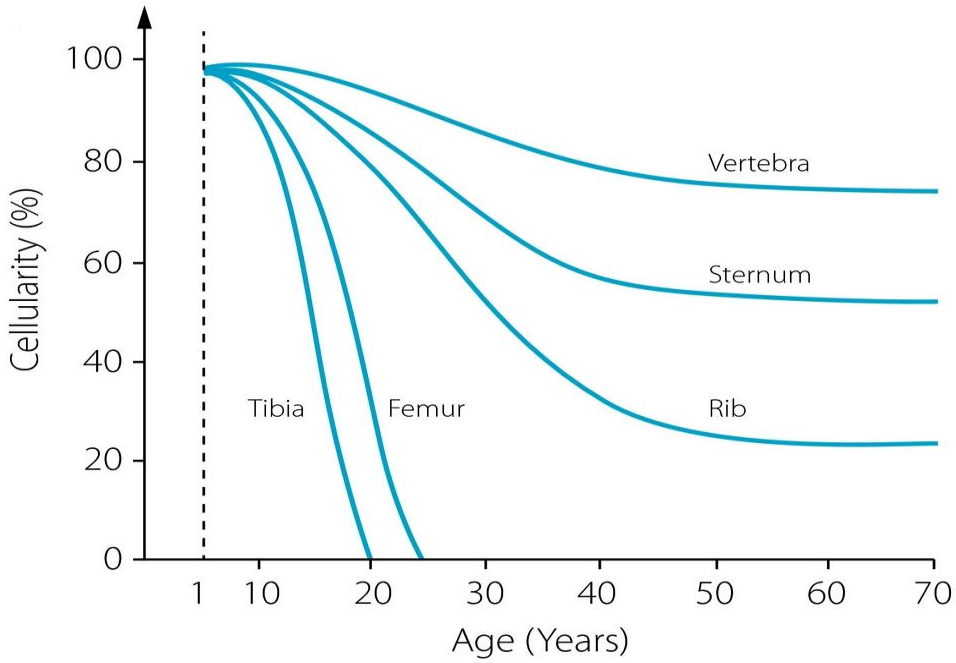

a)

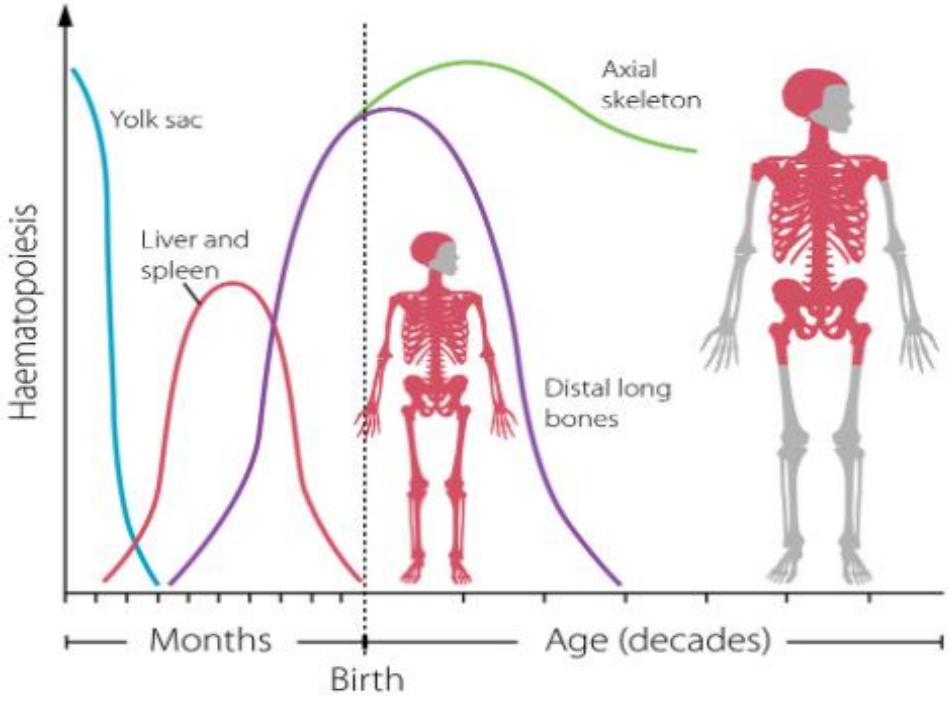

b)

Fig. 4: Bone marrow hematopoietic cellularity development. In the bone marrow system: a) cellularity of bone marrow throughout aging; b) natural conversion of red marrow into fat with aging. Sternum is cellular throughout different aging phases than the tibia or femur. The figures (a & b) from Veldhus Vlug AG, Rosen CJ. Clinical implications of bone marrow adiposity. J Intern Med 2018:283:121-139 [73].

.

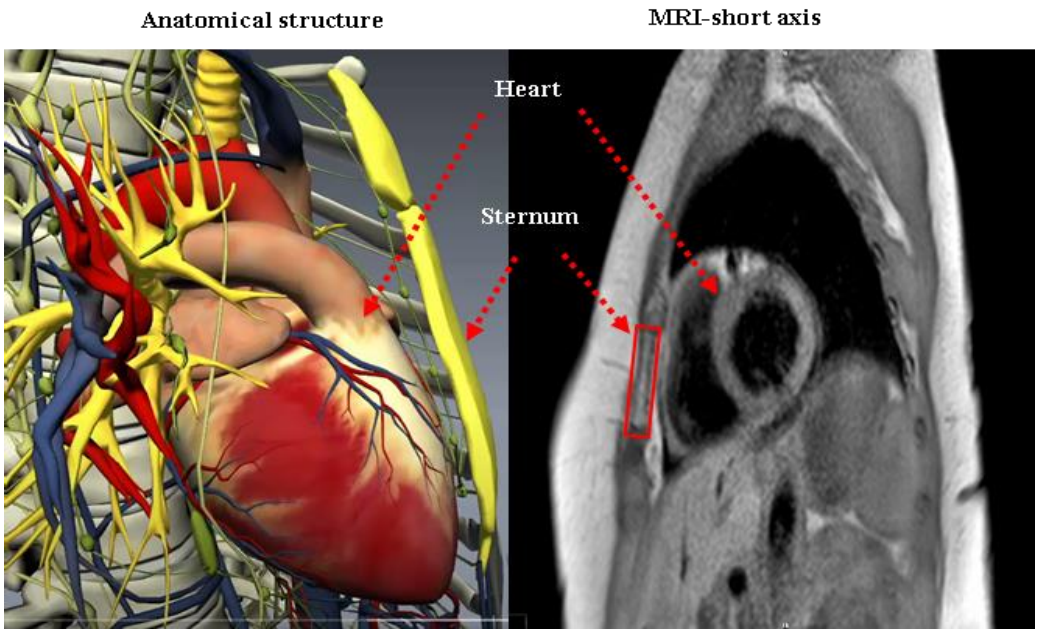

Fig. 5: Proximity of the heart to the sternum. On the right anatomical view represents the proximity of the sternum to the heart. On the left, sternum and heart on MRI short-axis slice. Left image from sternal angle - Angle of Louis - 3D Anatomy Tutorial-2017 - video Dailymotion

We always thought that immune cells from long bones (arms and legs) migrate via blood circulation to damaged tissues, but in 2018 a study of mice and humans [76] challenged this traditional view. Here, the authors described tiny vascular tunnels running from the skull bone marrow cavity to the outlining of the brain, which could be considered a short-cut route for immune cells responding to brain injuries, caused by stroke and other brain disorders. These findings indicate that immune cells may instead be taking a direct path to rapidly arrive at areas of inflammation. Further, the result of their study showed that during a stroke in the mouse brain, the skull bone marrow is more likely active to provide neutrophils than the tibia to the injured brain. In contrast, following a heart attack, the skull and tibia supply nearly similar numbers of neutrophils to the injured heart, which is far from both the tibia and skull. Further, they observed that 6 hours after the brain injury, there were fewer neutrophils in the skull than in the tibia, indicating that the skull bone marrow contributes more cells to the injured brain than the tibia. In conclusion, this study suggests that bone marrow does not uniformly contribute immune cells to injured or infected tissue brain, but there is a direct specific response from adjacent marrow tissue (skull) to the site of injury. We are thinking this might be happing also between the heart during MI and the sternum: since the sternum is located in close proximity to the heart (as in Figure 5) and always hematopoietic compared to long bones (as in Figure 4). So maybe the heart and sternum communicate in a similar way that causes more and quick release of immune cells from adjacent sternum marrow tissue to the infarcted heart.

1.6. Activation of bone marrow

Inflammation is the first response in many human diseases as an essential defense and repair mechanism [77]. After MI, immune cells including neutrophils and monocytes [78] are rapidly released into the blood [79]. Bone marrow provides most cellular components of sterile inflammation and the abundance of immune cells [80] in the circulation correlates with dramatic deterioration of the heart after MI [81]. The inflammation in the heart can be conceptually divided into three phases: an acute phase of the cell activation (between 1-7 days), a subacute phase with an adaptive immune response (last 1-4 weeks), and a chronic phase that can last from months to years [36]. Upon infarction, bone marrow is activated to release immune cells via recognition receptors [82]. The signaling pattern activates innate immune cells and cardiac cells to release different molecules such as cytokines, troponin, and creatine kinase, leading to further activation and homing of innate immune cells to the heart, including mast cells, neutrophils, and other immune cells [83]. The pain, anxiety, and released danger signals triggered by the cardiac damage induce emergency hematopoiesis in the bone marrow, leading to medullary monocytopoiesis [84], as illustrated in Figure 6. Neutrophils and other immune cells leave the bone marrow and mobilize to the damaged heart. Mast cells are among the first cells to respond to heart infarction and degranulate within 6 h of infarction and produce pro-inflammatory cytokines. Monocytes are crucial effector cells in MI [85], comprising a major proportion of infiltrating cells in the heart. They are a heterogeneous, multifunctional cell population with a crucial role in the pathogenesis of MI [86]. T cells and B cells [87] have been identified as critical mediators of cardiac healing in experimental models of MI [88]. Neutrophils are among the first lines of defense against infection and abundant mobilization to the damaged heart. This mobilization occurs earlier than that of any other infiltrated innate immune cells [36]. Up to now, most studies focused on innate immune cell recruitment from long bones (i.e. tibia and femur) after MI to inflammatory sites, but there is only limited knowledge about the contribution of other hemopoietic systems such as the sternum. In this study, we aimed to explore the interaction between the sternum and heart during infarction, to ultimately determine if the sternum tissue might be a potential new source of immune cells to the heart during injury. For this, we employed non-invasive magnetic resonance techniques as outlined in the next paragraphs.

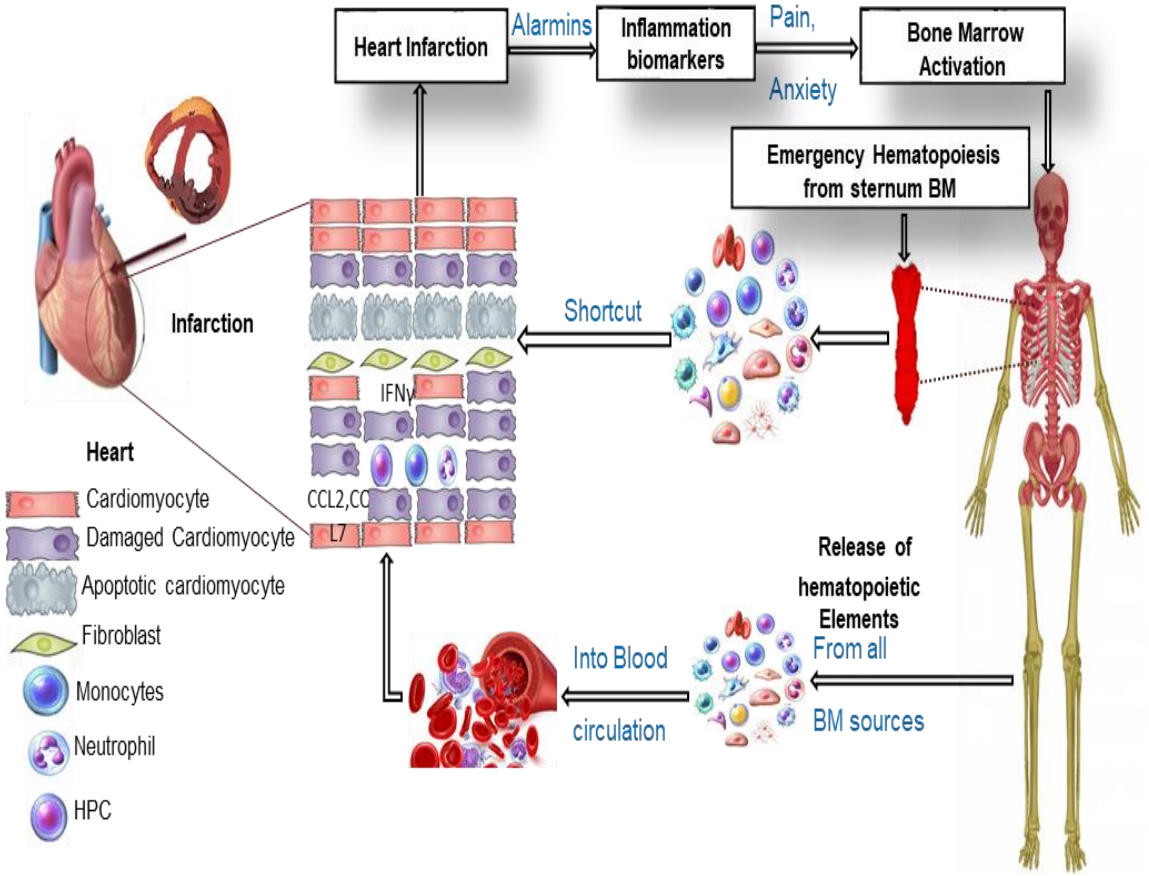

Fig. 6: Schematic connections of bone marrow activation during MI. In the heart, MI leads to cell damage and death and the release of alarmins, which trigger the recruitment and activation of cells from the innate immune system. Hematopoiesis in bone marrow, amplified by pain, anxiety, and the release of danger signals as a result of myocardial infarction, leads to extramedullary myelopoiesis as well as the release of myeloid progenitor cells into the circulation.

1.7. Magnetic resonance imaging (MRI)

Magnetic resonance imaging (MRI) is now a standard procedure in everyday clinical practice and in contrast to other imaging procedures such as SPECT, PET, or CT, does not require ionizing radiation or radioactive nuclei and is, therefore, gentler on the patient. MRI also offers excellent contrast between different tissues and enables the use of different mapping techniques and also spectroscopic investigations [89].

1.7.1. Bone marrow inside MRI

MRI is well suited for bone marrow imaging since the obtained images depend on the chemical composition of the soft tissue as shown in Table 1. Red and yellow bone marrows have different chemical compositions. Red marrow contains approx. 40% fat, 40% water, and 20% protein. Yellow bone marrow contains 80% fat, 15% water, and 5% protein [90]. As described above, in adult human, the normal bone marrow is characterized by a partial or complete fatty conversion and low cellularity, which leads to a relatively high signal

intensity on plain T1-MR images and low signal intensity on STIR or fat-saturated T2-MR images. And the opposite happens with children, their bone marrow is highly cellular, which leads to a low signal intensity on plain T1-MR images and a high signal intensity on STIR or fat-saturated T2-MR images [91].

Table 1 : Cellular components of the bone marrow in adults

Type of bone marrow	Cellular composition	Chemical composition
Yellow bone marrow	95% fat cells 5% non-fat cells	80% fat 15% water 5% protein
Red bone marrow	40% fat cells 60% hematopoietic cells	40% fat 40% water 20% protein

Conversion of bone marrow from red to yellow marrow occurs uniformly as a normal maturation process [92]. However, bone marrow is attentive to the human body and it responds to a demand when the body needs more hematopoietic elements to be produced, and that fatty marrow that developed over time turns over to hematopoietic marrow. The occurrence of reconversion in bone marrow leads to changes in signal intensity in MRI routine and these changes can cause suspicion of pathologic findings [69]. Therefore, the dynamic marrow reconversion during inflammations should be taken into consideration and the differences in bone marrow MRI signal can be used as a biomarker of what is going on with the human body.

1.7.2. Myocardial infarction by MRI

Magnetic resonance imaging (MRI) is an excellent tool for anatomical tissue characterization and offers different pathophysiological information after STEMI [93], including intramyocardial hemorrhage (IMH), microvascular obstruction (MVO), as well as myocardial edema and any development in the remote myocardial interstitial size. Furthermore, MRI provides information of MI size to be frequently used as a surrogate parameter and endpoint for different novel cardioprotective therapies in different controlled trials to reduce the size of infarction. In addition, novel parametric mapping techniques (relaxation time measurements) have evolved to detect myocardial edema (T2 mapping) and hemorrhage (T2* mapping) and both have proven of predictive value after STEMI. Taken together, MRI is well suited to provide a quantitative multiparametric characterization of the patients of myocardium after STEMI and to play a major role in the

evaluation of myocardial infarction along with its capability of comprehensive assessment of left ventricular function and morphology [94]. However, more focus and efforts are required to solve the timing of MRI acquisition after STEMI and to improve the time elapsed between contrast administration and acquisition of late gadolinium enhancement imaging in order to achieve a tool routinely used in clinical practice to improve accessibility for patients (do not need breath hold and minimize the scan time or cost) and to estimate the prognosis and guide treatment.

1.6.2.1 Relaxation time measurements

Quantitative MRI relaxometry, also called MRI mapping, is an excellent approach to precisely characterize different variations of tissue composition of the brain, heart as well as bone marrow. In fact, bone marrow implies different biochemistry and molecular alterations that can be detected on MRI mapping sequences. Currently, T1 and T2 mapping (Figure 7) sequences are being widely used as robust methods for the diagnosis of cardiomyopathies in parallel as predictive tools for treatment monitoring and prognosis [95]. These sequences aim to provide absolute values of tissue relaxation time that be used for detecting subtle variations in the considered tissues or for longitudinal studies. In addition, T1 and T2 can be used as reliable standardized methods for assessing myocardial infarction in practical clinical studies [96]. T1 mapping has been widely used in bone marrow or cardiovascular studies and has been shown to be correlated to water content [97]. However, MRI relaxation times are determined by a complex network of interactions from water content, fat, as well as proteoglycan fibers, which can provide information regarding the changes and mobility of water or fat molecules, then allows assessment of the tissue composition and characterization [98].

a) Sternum T1-weighted image in human

b) Sternum T2-weighted image in human

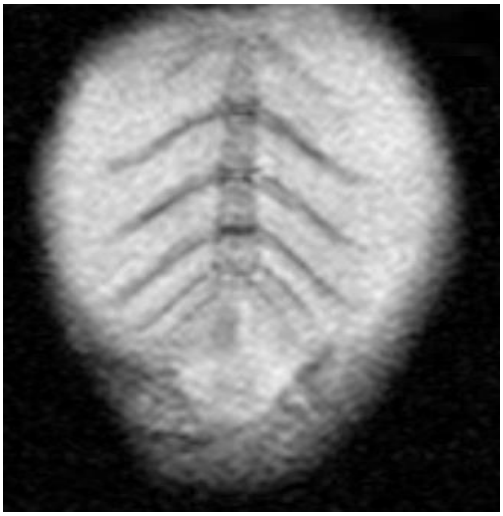

c) Sternum T1 map in mice

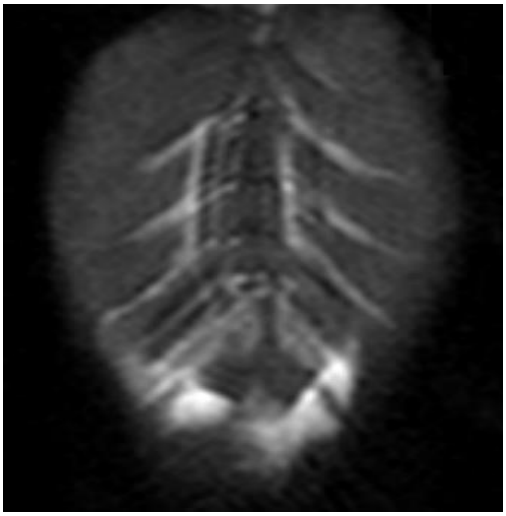

d) Sternum T2 map in mice

e) Long bones T1 map in mice

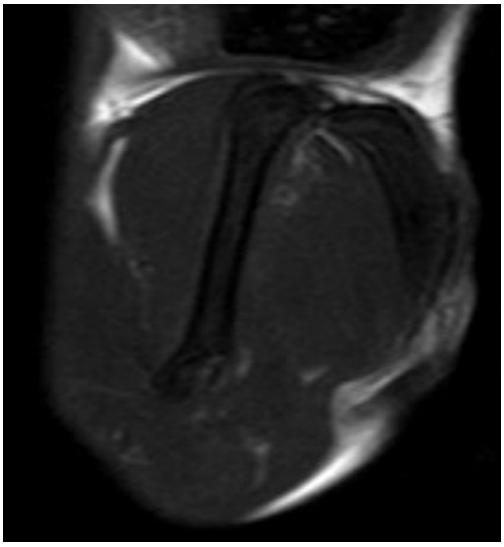

f) Long bones T2 map in mice

Fig. 7: Parametric mapping of bone marrow in human and mouse. On the left, bone marrow tissues on T1 map in human and mouse. On the right, bone marrow tissues on T2 map for both species.

Relaxometry is increasingly becoming the gold standard [99] of tissue characterization and has been integrated into routine cardiac examination protocols [100] in clinical practice as it allows quantitative analysis in a region of interest (ROI). In addition, its threshold-based methods can be used as an unlimited tool for the evaluation of diffuse myocardial changes such as myocarditis or diffuse fibrosis [101]. Moreover, it can be used to directly quantify extracellular volume fraction fractions of the tissues, further leading to the progressive integration of these sequences into routine cardiac magnetic resonance (MRI) settings [102]. Although T1 and T2 are parametric quantitative sequences [103], which provide tissue-specific T1 and T2 values, they always should be compared with normal reference values acquired under the same conditions such as scanner type, contrast agent, and scan time [104]. Another advantage of T1 and T2 mapping is the simplicity of T1 and T2 map acquisition [105] and parametric T1 and T2 value measurement [106].

1.6.2.2 Fat contents

All MRI techniques for estimating fat contents in tissue rely on proton density measurements inside the tissues. Currently, different methods of fat suppression have been used and developed over the years, each with its own advantages and limitations [107]. mDixon in MRI is a chemical shift method for the direct discrimination of the water and fat signal and was already used for the assessment of edema therapy, response, conspicuity, and characterization [108]. It is based on phase shift secondary to water-fat resonance frequency differences [109]. The principle of this method is allowing the separation of water and fat signals to be postponed to the image postprocessing phase and requires only a single data acquisition sequence with multiple echo times [110]. This method for fat suppression is highly homogeneous [111] on both T2 and T1 images in musculoskeletal protocols [111]. A combination of MRI relaxometry and fat determination should thus be well suited for the non-invasive assessment of the tissue alterations in the bone marrow associated with the activation of emergency hematopoiesis after myocardial infarction: The activation of the bone marrow for the formation and release of immune cells into circulation is assumed to be associated with substantial metabolic turnover. This will result in an enhanced consumption of oxygen, sugar, or fat to match the increased energy demand which in turn will rise perfusion for substrate supply. Altogether, this will alter the tissue properties in a way that is prone to readout by MR relaxometry.

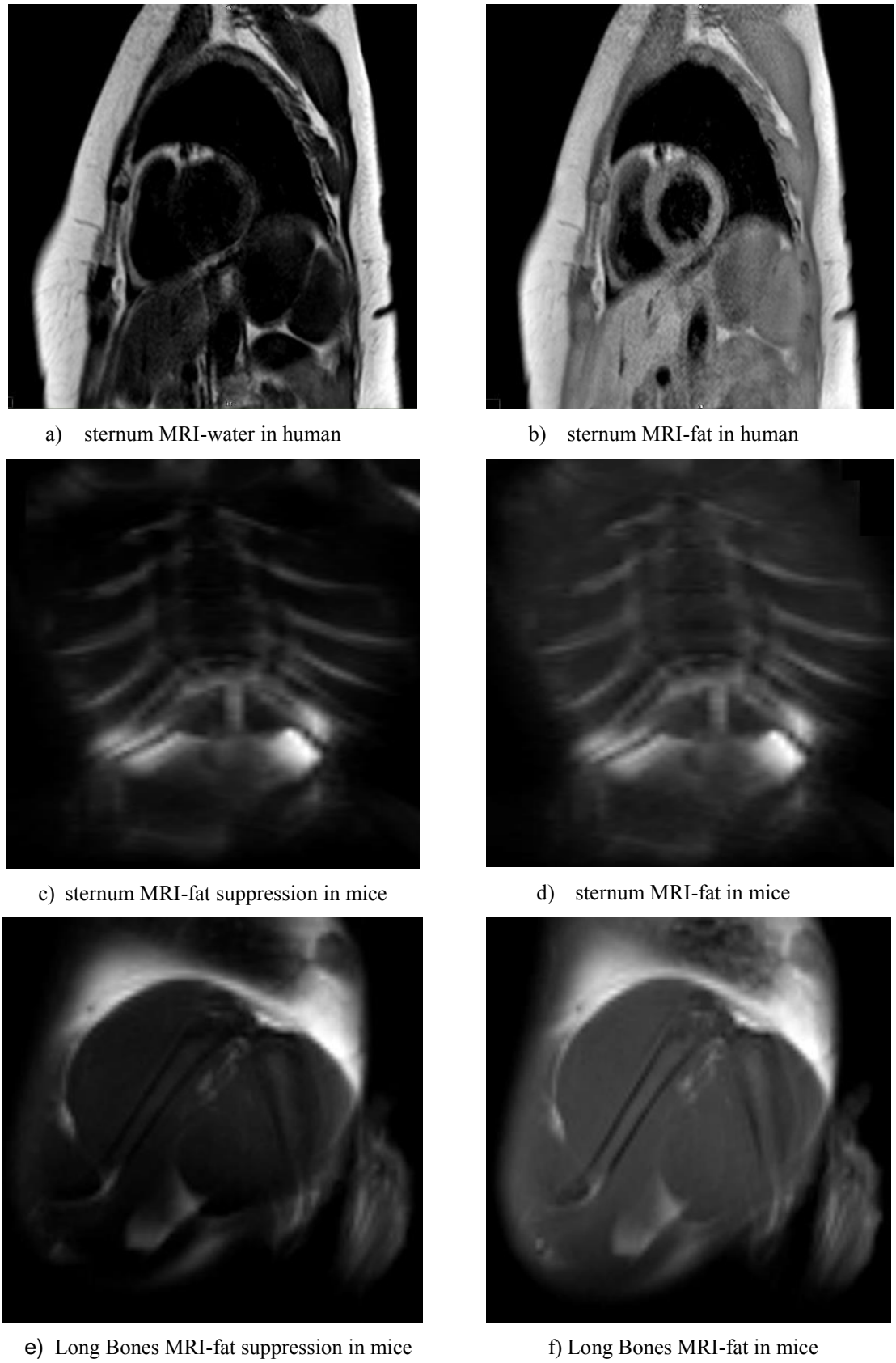

a) sternum MRI-water in human

b) sternum MRI-fat in human

c) sternum MRI-fat suppression in mice

d) sternum MRI-fat in mice

e) Long Bones MRI-fat suppression in mice

f) Long Bones MRI-fat in mice

Fig. 8: Fat of bone marrow tissues in human and mouse. On the left, is a view of the water sequence for bone marrow tissues in human and mouse. On the right, is the fat sequence for both species.

.

These changes will impact the homogeneity of the local magnetic field and thereby tissue relaxation times. Furthermore, substrate consumption can alter the tissue fat content and can be detected using MRI mDixon sequences.

1.8. Tracking of immune cells by ^{19}F MRI

1.8.1. Perfluorocarbon nanoemulsions (PFCs)

Perfluorocarbons are alkane molecules in which all hydrogen atoms have been replaced by fluorine and can exist in both linear and cyclic forms. With very short chain lengths, perfluorocarbons are gaseous at room temperature; with longer chain compounds, they are transparent, odorless liquids to solid compounds such as Teflon [112]. Due to their high ^{19}F content, these can be easily detected using ^{19}F MRI [113]. Perfluorocarbons have some special features, e.g. described as fluorophilic, mainly soluble in substances of their own compound family, but have a higher tendency to be lipophilic than hydrophilic. Perfluorocarbons can have a density of up to 2 g/ml and are also considered to be chemically inert and non-toxic, which makes them ideal for in vivo use. The C–F bond in particular plays an important role here, one of the strongest bonds described in organic chemistry. So far, no enzyme is known that would be able to split this compound and thus break down the perfluorocarbons [114]. Perfluorocarbons were produced on a large scale for industrial use by Minnesota Mining and Manufacturing as early as the 1950s [115]. Mainly perfluorooctanoic acid (PFOA) and perfluorooctanesulfonic acid (PFOS) were produced, both long-chain linear compounds. These were used e.g. in the production of Teflon, the impregnation of jackets, or as an addition to fire-fighting foam. There is now a controversial discussion about the extent to which these perfluorocarbons can affect human health[116]. Perfluorocarbon nanoemulsions (PFCs) are emulsions in which perfluorocarbons act as the dispersed phase and (phospho) lipids as emulsifier. PFCs have been intensively investigated as part of the development of artificial blood substitutes because of their high oxygen affinity However, this application has become less important in recent years since other functions besides oxygen binding could not be fulfilled by the PFCs. An important area of application is now imaging of inflammation using ^{19}F MRI [117].

1.8.2. Imaging of inflammatory processes by ^{19}F MRI

As pointed out above conventional ^{1}H MRI is an excellent tool for body imaging and observing biological and physiological processes with high resolution and contrast between different tissues [118]. However, it is somewhat limited in its potential to track the fate of immune cells from their sources to the site of inflammation. As an alternative,

recently the use of PFCs as tracer for cell tracking has been described [119]. PFCs mostly exhibit high fluorine pay-load and are one of the most biologically inert organic molecules that have ever been used [120]. After intravenous administration of PFCs [121], they are taken up by circulating, phagocytotically active immune cells. In the event of inflammation, these cells migrate from the bloodstream into inflamed tissue. Since there are almost no fluorine compounds in the body [122], this can be detected without background using ^{19}F MRI and anatomically assigned in combination with ^{1}H MRI. Our working group was able to adapt this method for a large number of different disease models, e.g. heart attack, atherosclerosis, stroke, or even thrombi [123]. Fluorine imaging is therefore an elegant method of non-invasively imaging inflammatory processes in vivo. However, this passive targeting is limited to phagocytic cell populations.

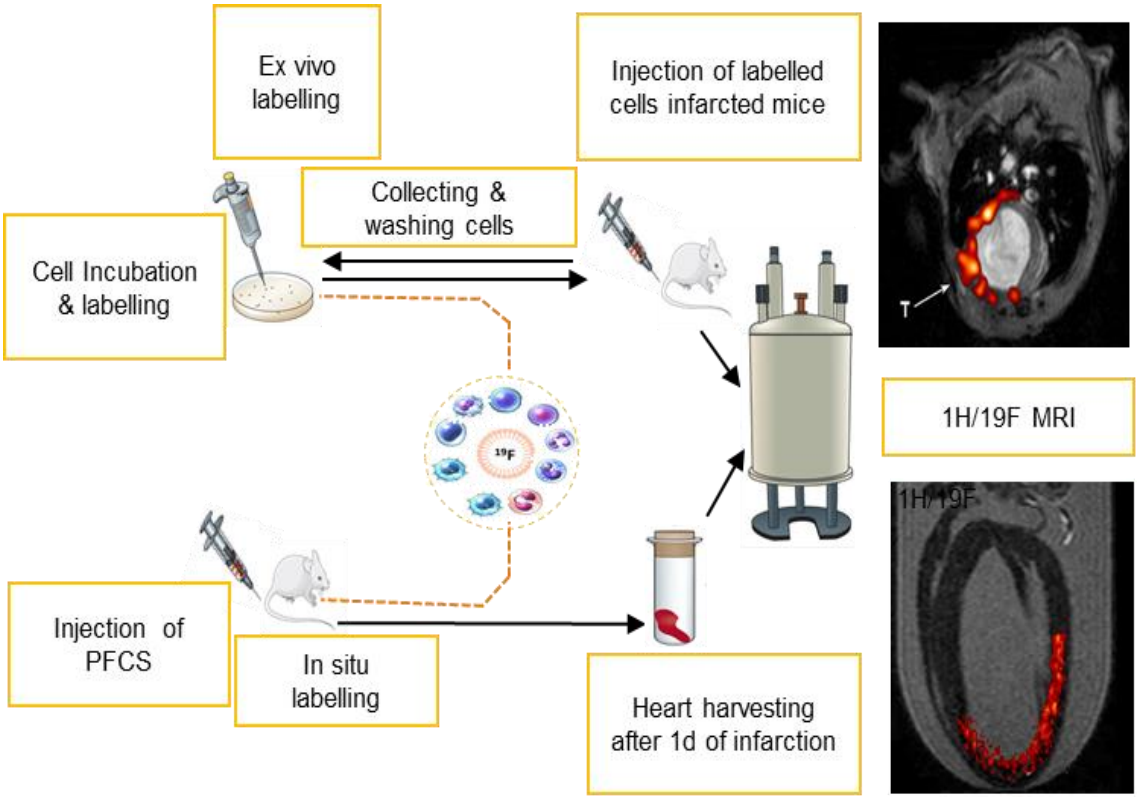

Fig. 9: ^{19}F MRI technique for tracking the fate of immune cells. Cell labeling can be done ex vivo using the cell of choice after culturing cells and adding a specific labeling reagent with perfluorocarbon (PFC) emulsion directly to the media followed by timing incubation to ensure labeling. Self-delivering formulations of PFC emulsions have also been devised that do not require a transfection agent. The administration is done after collecting and washing the labeled cells in the subject. Further labeling agents can be intravenously injected in situ labeling approach. These agents are intrinsically taken up by immune cells (monocytes and macrophages), which then migrate and accumulate at inflammatory sites. For both ex vivo and in vivo, labeling approaches a 1H MRI scan is then carried out to visualize the anatomy and then retuned for 19F MRI measurement for detecting 19F signal.

In order to extend this approach to distinct cell populations, specific targeting of the PFCs is required. The active targeting of immune cells can be done in two different ways: cells can be loaded ex vivo with suitable contrast agents and then re-implanted, or a targeted contrast agent can be administered directly in vivo, as shown in Figure 9. In contrast to ex vivo immune cell loading, for an in vivo approach, uptake by phagocytotically active cells must be prevented, since they are in constant competition with the target cells. The PFCs can be directed to the target cell of choice, which can be achieved by coupling antibodies, antibody fragments, or even peptides to the PFC surface after suitable surface PEGylation for shielding the particles.

1.9. Work objective

The aim of the present was to investigate the role of the sternum in emergency hematopoiesis after AMI. To this end, the sternum tissue characteristics were investigated in STEMI patients and a murine model of reperfused AMI by non-invasive MRI. Here, it was assumed that in particular the relaxation times T1 and T2 might be a sensitive quantitative measure for tissue alterations induced by the activation of emergency hematopoiesis in the sternum after AMI. Furthermore, ^{19}F MRI was employed to track the fate of sternal neutrophils after AMI in mice. These in vivo measurements were complemented by laboratory diagnostics in humans and flow cytometric analyses of bone marrow immune cells in mice.

2. Materials and Methods

2.1. Materials

2.1.1 Devices

Table 2 : Laboratory equipment and devices

Device	Manufacturer	Type designation
Analytical balance	Ohaus Europe (Greifensee, Switzerland)	PA214
	Kern (Balingen, Germany)	AEJ
Autoclave	F. & M Lautenschläger (Cologne, Germany)	5169
Chemiluminescence imager	Intas (Goettingen, Germany)	Intas ECL CHemilum Imager
Flow cytometer	BD Biosciences (San Jose, USA)	FACSCANTO II
Magnetic stirrer	MP Biomedicals (Santa Ana, USA)	FastPrep-24
Microfluidizer	IKA works (Staaufen, Germany)	Ultra Turrax TP 18/10
Microscope	Olympus (Hamburg, Germany)	BX 61
	Olympus (Hamburg, Germany)	CKX31
Microtiter shaker	IKA (Staufen, Germany)	MTS 2/4
MR microimaging system	Bruker (Rheinstetten, Germany)	Micro 2.5
MR resonators	Bruker (Rheinstetten, Germany)	25-0mm birdcage
MR spectrometer	Bruker (Rheinstetten, Germany)	400MHz Bruker AVANCE^{III} Widebore
Nano-Drop	Thermo Fisher (Rockford, USA)	NanoDrop2000

pH meter	Kink (Berlin, Germany)	766 Calimatic
Pipettes	Eppendorf (Hamburg, Germany)	Research
Plate shaker	IKA works (Staufen, Germany)	MTS 2/4
Polarizing filter	Olympus (Hamburg, Germany)	U-Ant, U-Pot
Roller mixer	CAT (Staufen, Germany)	RM5
Clean bench	Labogene (Lynge, Denmark)	Scanlaf Mars Pro Cytosafe Class 2
Transblot system	BioRad Laboratories (Hercules, USA)	Transblot turbo transfer system
Scanner	Canon (Krefeld, Germany)	Canon LiDE 700F
Vacuum suction system	HLC (Pforzheim, Germany)	AC 04
Centrifuges	Beckman Coulter (Brea, USA)	Allegra X-30R
	Eppendorf (Hamburg, Germany)	5415R
	Thermo Fisher (Rockford, USA)	Heraeus Megafuge 16R
	Thermo Fisher (Rockford, USA)	Heraeus Biofuge Primo P

2.1.2 Chemicals and reagents

Table 3 : Chemical and reagents used in laboratory

Designation	Manufacturer
Cholesterol-PEG2000-maleimide	Nanocs (USA)
Cholesterol-PEG2000-Biotin	Avantilipids (USA, Alabama)
Clostridium histolyticum collagenase	Serva, (Germany, Heidelberg)
DPBS	Biofroxx (Germany, Einhausen)
DSPE-FITC	Avantilipids (USA, Alabama)
DSPE-PEG2000	Avantilipids (USA, Alabama)
DSPE-PEG2000-Biotin	Avantilipids (USA, Alabama)
DSPE-PEG2000-Maleimid	Avantilipids (USA, Alabama)

DSPE-RhodaminB	Avantilipids (USA, Alabama)
FCS	Biochrom (Germany, Berlin)
Formaldehyde solution 4%	PanReac AppliChem (Germany, Darmstadt)
G-CSF	R&D System (USA, Minneapolis)
Glutamax	sigma-Aldrich (Germany, Darmstadt)
Gro-α	R&D System (USA, Minneapolis)
HEPES	Thermo Fisher (USA, Rockford)
Histopaque 1077	Sigma-Aldrich (Germany, Darmstadt)
Histopaque 1119	Sigma-Aldrich (Germany, Darmstadt)
IL-8	R&D System (USA, Minneapolis)
LPS Salmonella typhimurium	Calbiochem (Germany, Darmstadt)
Maleimid-PEG2000-Biotin	Thermo Fisher (USA, Rockford
Matrigel Matrix MEM NEAA	Corning (USA, Bedford) Thermo Fisher (USA, Rockford)
perfluorocrown ether	ABCR (Germany, Karlsruhe)

2.1.3 Consumables

Table 4: Consumables used in laboratory

Designation	Manufacturer
6- well plates	Greiner Bio One (Austria, Kremsmünster)
12- well plates	Greiner Bio One (Austria, Kremsmünster)
48-well plates	Greiner Bio One (Austria, Kremsmünster)
15 ml-Falcon	Greiner Bio One (Austria, Kremsmünster)
50 ml-Falcon	Greiner Bio One (Austria, Kremsmünster)
EASYstrainer 40 µm, 70 µm, 100 µm	Greiner Bio One (Austria, Kremsmünster)
Isofluran	Actavis GmbH (Österreich, Wien)

2.1.4 Antibodies

Table 5 : Antibodies used for flow cytometry analysis

Specificity	Fluorochrome	Clone	Reactivity	Company
CD45	PE-Cy7	30-F11	murine	BD Biosciences
CD11b	APC	M1/70	murine	Biolegend
Ly6G	PE	1A8	murine	BD Biosciences
Ly6C	APC-Cy7	AL-21	murine	BD Biosciences

2.1.5 Puffer

Table 6 : Puffer used in laboratory with the corresponding composition

Name	Additions	Concentration
Lysis buffer for erythrocytes	Ammoniumchloride	8.29 mg/ml
	Potasssiumhydrogencarbonate	1 mg/ml
	Sodium EDTA	0.0375 mg/ml
MACS buffer	PBS	
	BSA	2 %
	EDTA	1 mM
Phosphateglycerol buffer (pH 7.4)	Na_2HPO_4	7 mM
	NaH2PO4	3 mM
	Glycerol	2.5 vol%

2.1.6 Software programs

Table 7: Used software programs

Software program	Manufacturer
CV45	Circle Cardiovascular Imaging, Calgary, Canada
Excel 2020	Microsoft Corporation
GraphPad PRISM 6	GraphPad Software, Inc.
PowerPoint 2020	Microsoft Corporation
Flow Jo 2020	NovoExpress Software

2.2. Methods

2.2.1 Human

2.2.1.1 ST-Elevation myocardial infarction (STEMI)

The aim of the SYStemic organ communication in the ST-Elevation Myocardial Infarction (SYSTEMI) study is to identify patterns in the cross-talk of cardiac systemic metabolism, which influence survival and the development of heart failure after STEMI, in order to improve diagnostic and therapeutic algorithms in/after myocardial ischemia for patient-risk assessment and tailored therapy. The STEMI study was conducted in accordance with the declaration of Helsinki and approved by the local Ethics Committee of Heinrich Heine University (HHU) and the State Medical Association (HHU: ethics number 5961R and 2021055; North Rhine State Medical Association: 2021055). Registration was made at www.clinicaltrials.gov: NCT03539133. All patients gave their written informed consent to participate. SYSTEMI is an open, prospective, observational, multicenter cohort study on patients with STEMI (the study started in 2018), which is supported by the German Research Foundation (SFB 1116, grant number 236177352). As part of patient characterization, the patients received an MRI examination of the heart and vessels as part of their index hospitalization on days 1, and 5 after admission and 6 months follow-up. The MRI examination protocol includes the display of left, and right ventricular function, infarct characteristics using late gadolinium enhancement (LGE) and parametric mapping. As bystander in parametric mapping, the sternum bone marrow tissue was examined. In addition, on day 1, 5, and 6 months after admission, laboratory analysis of circulating biomarkers was also carried out at the same time. All examinations were carried out in the functional department of the Clinic for Cardiology, Pneumology, and Angiology of the UKD by medical staff qualified for the respective examination. The data collected was processed in pseudo-anonymized form as part of further evaluation.

2.2.1.2 Inclusion and exclusion criteria

According to Table 8, the SYSTEMI study included all patients who were admitted to our hospital with a STEMI older than 18 years. Informed consent was requested provided there were no exclusion criteria. ST-elevation myocardial infarction was determined according to the European Society of Cardiology guidelines as in [26]: ST-segment elevation in at least two adjacent ECG leads in patients with persistent chest discomfort or other symptoms suggestive of ischemia. In the ECG, the recorded standard is 10 mm/mV, measured at J-point according to the appropriate clinical context that has been considered indicative of acute coronary artery occlusion in the following cases.

- In the leads V2-V3 there are a minimum of two connected leads with an ST-segment elevation ≥ 1. 5 mm in women or ≥ 2.5 mm in men < 40 years, ≥ 2 mm in men ≥ 40 years in the leads V2-V3.
- ST elevation ≥ 1mm in the other leads is considered relevant in the absence of left ventricular hypertrophy or left bundle branch block (LSB).
- If the T wave is positive as a result of ST depression in leads V1-V3 or ST-segment elevation equivalent, the confirmation of concomitant ST-segment in leads V7-V9 is ≥ 0.5 mm and should be considered.
- A right precordial lead (V3R and V4R) was recorded in patients with inferior MI.

  ST-segment depression is ≥ 1 mm in eight or more superficial leads associated with ST-segment rise in V1 or aVR suggesting obstruction of the left main coronary artery, or severe ischemia in three coronary vessels. The following criteria were considered to improve the diagnosis of STEMI in LSB:
- Predominantly positive ST-segment elevation (1 mm in leads with positive QRS complex)
- Significant ST-segment depression 1 mm in V1-V3;
- Discordant ST-segment elevation ≥ 5 mm in leads with negative QRS complex.

  The primary percutaneous coronary intervention and any subsequent treatment were performed according to standard clinical care and guideline [26]. Patients who could not receive an MRI examination due to a prolonged stay in intensive care units, e.g. with cardiac shock complications, were excluded from the analysis.

Table 8 : Inclusion and exclusion criteria of the SYSTEMI cohort

Inclusion criteria	Exclusion criteria
STEMI	Age <18 years
Signed consent form SYSTEMI study	Residence abroad
	Poor neurological outcome
	Pregnancy
	Life-limiting disease with a life expectancy <1 year
	Contraindications to MRI examinations
	Sternum in MRI images could not be evaluated such as in T2 & T1 maps

General contraindications for performing an MRI were: pacemakers, metal vessel clips, metal splinters in the body, implanted insulin pumps, and claustrophobia. Patients whose MR images could not be evaluated were also excluded. Patients who withdrew from the study in the course of the study continued to be included in the analysis if they consented

to data processing. The inclusion and exclusion criteria for the patients evaluated for this work are summarized in the Table 8.

2.2.1.3 Medical history

The medical history of patients was taken uniformly using a case report form developed by the main examiner. In this questionnaire, socio-economic information was collected and questions about the current health-related quality of life were answered. The documentation and collection of the data were carried out by a study nurse and the STEMI doctors, who are integrated into SYSTEMI and supervise the study. First, the following demographic data was determined in the test form: known and treated arterial hypertension, T2DM, nicotine abuse, hyperlipidemia, chronic obstructive pulmonary disease, chronic renal insufficiency, atrial fibrillation, peripheral arterial occlusive disease, status post. Stroke/transient ischemic attack, known coronary artery disease, status post. Myocardial infarction (earlier), status post-PCI (formerly), bypass surgery, sleep apnea syndrome, family disposition (closest relative with a heart attack <65 years), other relevant previous illnesses. In addition, the time between the onset of the symptoms of the heart attack and the alarm of the emergency services was inquired about. Finally, the patient's home medication was documented.

2.2.1.4 Study design and population

For the human studies, we made use of the SYSTEMI cohort of the Department of Cardiology, Pneumology, and Angiology within the University Hospital of Dusseldorf (UKD). Patients (n=153 STEMI, age 62.8 ± 12.3 years) received MRI at 5 days and 6 months after STEMI and a sub-cohort (n=40) received another MRI at 1 day after STEMI, 5 days and 6 months of recovery.

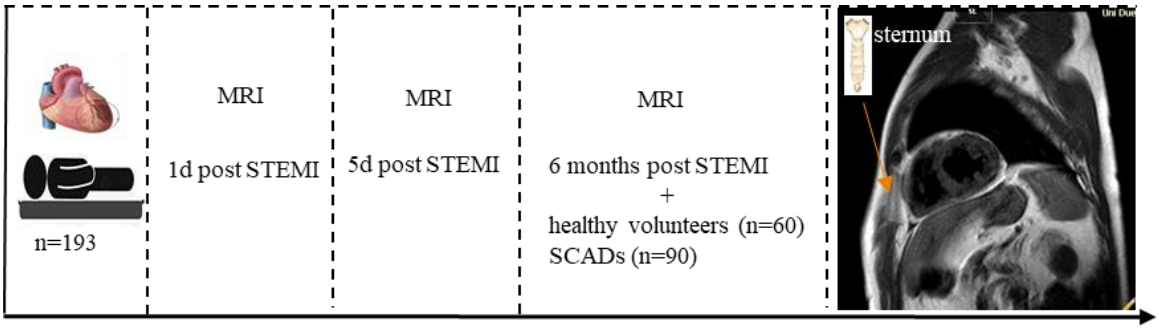

Fig. 10: Schematic design of STEMI study by MRI. The proposed study (n=193 STEMI patients) was evaluated by MRI at 3 times STEMI, day 1+5, and after 6 months of recovery measuring. Matched-age healthy volunteers (n=60) were included as well as patients with stable coronary disease (n=90 with SCADs).

In addition, healthy volunteers (n=60, age 59.2 ± 10.6 years), and patients with stable coronary artery disease (n=90, age 61.2 ± 14.6 years) were investigated. All were subjected to a standardized cardiac MRI protocol which includes functional assessment, LGE for infarct size (only for STEMI) measurements but also T1 and T2 relaxation maps for determination of myocardial fibrosis and edema, respectively. Since the heart is located in close anatomic proximity to the sternum, these measurements were evaluated for a comprehensive characterization of the bone marrow properties within the sternum. For this, sternal relaxation times and its fat content (proton density fat fraction (PDFF)) were determined. Consecutive participants enrolled from January 2018 to December 2022 were included in this study.

2.2.1.5 Cardiac MRI measurements

The MRI examinations were performed using a standard 1.5 Tesla scanner (Achieva, Philips, Best, the Netherlands) in the Department of Cardiology, Angiology, and Pneumology of the University Hospital Düsseldorf. The MRI examination and the preparations were carried out by qualified medical-technical radiology assistants under the supervision of a DGK and ESC Level III certified cardiologist. The duration of the MRI examination was about 60 minutes. The gadolinium-containing, cyclic contrast agent Calriscan®, Bracco IMAGING Deutschland GmbH, was used for LGE.

2.2.1.5. 1 MRI protocol to assess left ventricle

The functional and geometric assessment of the left ventricle was performed using electrocardiogram-triggered cine-steady-state-free-precession (SSFP) imaging in standard long-axis geometry (two-, three-, and four-chamber views) and in short-axis orientation covering of the ventricle from the base to apex (repetition time/echo time= shortest 3.2/1.6 ms, flip angle = 60°, reconstructed voxel size/spatial resolution = 8×1.2×1.2 mm^3, phases: 30, one respite per shift). LGE imaging was performed eight to ten minutes after gadolinium contrast agent injection (0.2 mmol/kg body weight) using a three-dimensional gradient-spoiled turbo fast-field echo sequence with a non-selective 180° inversion recovery prepulse triggered to end of diastole. SSFP images served as anatomical reference (repetition time = shortest, echo time = shortest, flip angle = 15°, spatial resolution = 5×1.5×1.5 mm^3, 2 stacks of 10 slices each for short-axis orientation, a breathing space per batch). Here, retrospective ECG gating was used.

2.2.1.5. 2 T2 and T1 relaxation times

T2-weighted single-shot turbo spin echo-SPIR sequence was used in short-axis orientation from base to apex (TR = 2 beats, TE = shortest, FA = 90°, spatial resolution = 8 × 0.9 × 0.9 mm^3, 10 slices, black-blood prepulse, breath-hold) or a standard T2-weighted turbo

spin-echo SPIR sequence (TR = 2 beats, TE = 90 ms, FA = 90°, spatial resolution = 8 × 0.6 × 0.6 mm^3, 10 slices, black-blood prepulse, breath-hold). T1 was acquired using prepared T2 sequence with the following parameters: TE/TR=TE/TR =2.2/1.03 ms, flip angle =35°, slice thickness= 10 mm, field-of-view =300×300 mm2, reconstructed matrix =256×256 pixels, total scan duration=35 min.

2.2.1.5. 3 MRI fat measurement

In a sub-cohort of patients, MRI fat measurements were performed using mDIXON in a transversal orientation covering the whole heart. The mDixon method is combining 2 Dixon-implemented methods with flexible echo times. The imaging parameter for the 3D_mDIXON-WH were as follows: Trigger time (TD) =739.00 msec, Echo time (TE) =0.0 msec, Flip angle (FA) =15º, Repetition time (TR) =5.73msec, slice thickness=1.50 mm^2 .

2.2.1.6 Image data analysis

2.2.1.6.1 Cardiac output

All left ventricular (LV) volumes and functions were calculated from short-axis SSFP images using automatic, computer-aided contour recognition. A manual correction was made when the contours were not correctly recognized by the computer. The cardiac volumes LV end-diastolic volume (LVEDV), LV end-systolic volume (LVESV), and stroke volume (SV) were related to body surface area (ml/m²). This results in the LVEDV index (=LVEDVi), the left ventricular end-systolic volume index (LVESVi), and the stroke volume index (SVi). After endocardial and epicardial segmentation of short-axis LGE images, semi-automated computerized threshold detection (>5 SD of uninjured myocardium) was used. The following variables could be derived from this: A) infarct size (IS) and microvascular obstruction (MVO) [126,127]. MVO visualized by LGE was defined as a region of hypo-enhancement within the hyper-enhanced area [126]. Infarction size (IS) and MVO were expressed as percentage of total left ventricular mass. The MVO was additionally expressed as percentage of the IS.

2.2.1.6.2 Sternal relaxation and fat evaluation

To assess sternum T1 and T2, a region of interest as large as possible was manually drawn in CVI45 software in short-axis slices, taking care to avoid other tissue signals. The average of values was taken in order to have a representative value of the sternum. Once the region around the sternum was drawn, T1 and T2 times were automatically displayed on the CV45 platform. As reference also for other tissues, T1 and T2 were determined (such as the liver, spleen, heart, and fat depots).

Data acquired with mDIXON sequences were reconstructed on the CVI45 system using

the available standard interface. Each data set yielded images for water only, fat only, in-phase, and out-phase. In DICOM fat or water images, a ROI was manually drawn around the sternum and signal intensity (SI) values were automatically displayed in a pixel-wise manner as mean and SD. From this, the fat percentage was calculated according to the following formula:

$$Fat\ percentage = \frac{SI(fat)\ X\ 100}{SI(Water + FAT)}$$

Images were independently analyzed and the ROI were carefully placed to avoid regions of other tissues or regions with artifacts.

2.2.1.7 Blood inflammation markers

Blood samples were taken immediately at days 1+5 post STEMI and after 6 months of follow-up . Blood samples were obtained by peripheral venipuncture and analyzed for high-sensitivity troponin, C-reactive protein (CRP), neutrophils, leukocytes, creatine kinase, and others. This was conducted in conformity with the declaration of UKD and proved by the local research committee.

2.2.2 Mice

2.2.2.1 Study population

2.2.2.1.1 C57BL/6J mice

Male mice (C57BL/6J, n=14, 20-25 g (body weight), 12-14 w (age)) used in this study were housed with a 12 hours light to 12-hour dark cycle at 22 ± 2 °C and humidity of 55% at the Tierversuchsanlage of Heinrich-Heine-Universität, Düsseldorf, Germany.

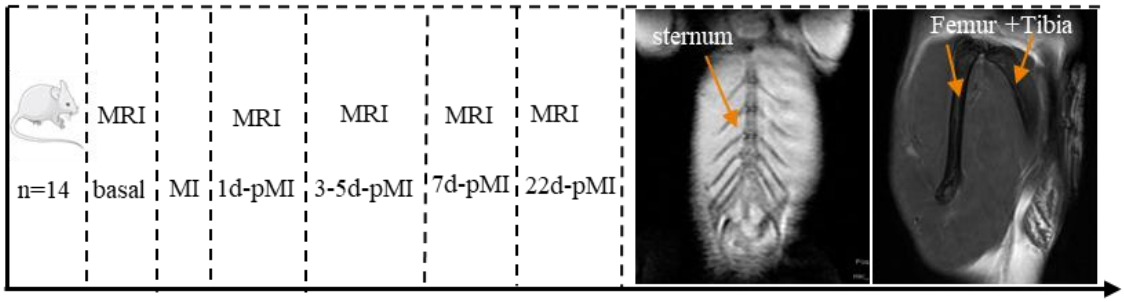

Fig. 11: Experimental design of MI mice model. The mice (n=14) were exposed to high-resolution 9.4 T MRI at baseline and on 1 day, 3-4 days, 7 days, and 22 days after MI. They were fed with a standard chow diet and received tap water ad libitum.

They were fed with a standard chow diet and received tap water ad libitum. Reperfused MI was provoked by a transient ligation (50 min) of the left anterior descending coronary artery (LAD) as previously described [127]. All mice received baseline ^{1}H MRI prior induction of MI, and on 1 day, 3-4 days, 7 days, and 22 days after MI, as shown in Figure 11. The reference number of the C57BL/6J mice testing permit is: 81-02.04.2018.A399.

2.2.2.1.2 ApoE mice

ApoE mice (ApoE-Rh/h, SR-BI−/−, n=14, 20-25 g (body weight), 12-14 w (age)) expressing a hylomorphic mutant and lacking the scavenger receptor class B type I were bred and housed with a 12 hours light (6:00-18:00) to 12-hour dark (18:00-6:00) cycle at 22 ± 2 °C and humidity of 55% at the central animal facility of the Heinrich Heine University Düsseldorf, Germany. For induction of the cardiovascular disease model [128], mice were exposed to a high fat/high cholesterol [129] (Western diet, containing 15% fat + 0.25% cholesterol).

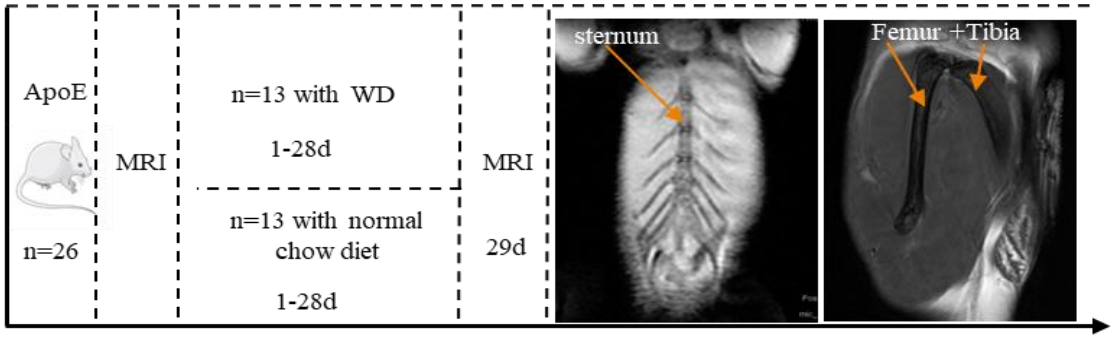

a)

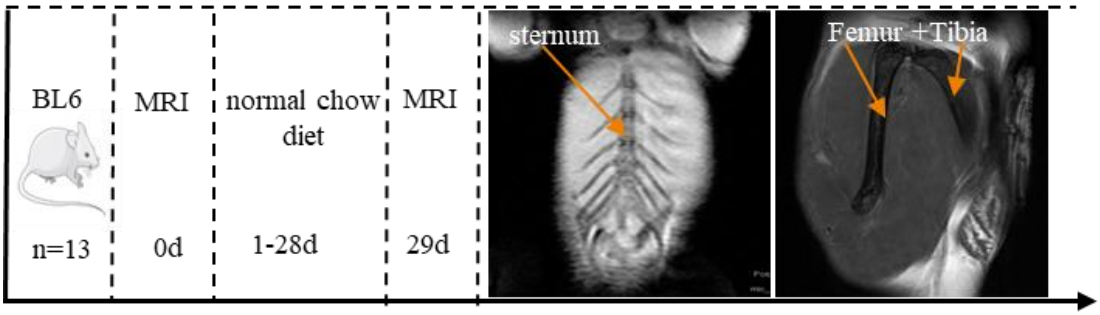

b)

Fig. 12: Experimental protocol of mice fed Western Diet. a)ApoE mice were investigated from day 0 to day 28 after the onset of the diet. **b**) The BL6 mice were exposed to a normal chow diet and measured at 0 days and after 28 days of the chow diet.

A total of 26 ApoE mice were used in this study, thirteen of them were subjected to a Western diet, and the other thirteen were kept with a normal standard diet. As additional control, 13 C57BL/6 mice were kept with a normal diet for 4 weeks. The reference number of the ApoE animal testing permit is: 81-02.04. 2020.A290. All mice received ^{1}H MRI for determination of sternal relaxation times and fat content at baseline to day 28 after the onset of the diet, as illustrated in Figure 12.

2.2.2.2 MRI protocol

The measurements for mice were carried out using a wide-bore NMR spectrometer (Bruker AVANCE^{III} 9.4T, at frequencies: ^{1}H=400.21 MHz; ^{19}F=376.54 MHz) [130]. Images were acquired with shielded gradients (1.5 T/m) using a microimaging unit Micro 2.5 and a 25 mm birdcage resonator tunable for both ^{1}H and ^{19}F [131]. Mice were anesthetized with 1.5% isoflurane (ing) and kept at an ambient temperature equal to 37 °C. For further prevention of eye dehydration and mucous membranes, the gas mixture of anesthesia was moisturized by passing the mixture through a gas-washing bottle filled with water. To record ECG, both front paws (left and right) were attached to ECG electrodes (Klear-Trace; CAS Medical Systems) and respiration was monitored by means of a pneumatic pillow positioned at the animal's chest or back. For fluorine measurements, we started with initial acquisition of ^{1}H scans to acquire the corresponding anatomical information for detected ^{19}F signals, then the resonator was tuned to ^{19}F for recording the ^{19}F images across the area of interest (in our case heart and sternum) [132].

2.2.2.2.1. Heart function measurement

Mouse heart function images were acquired using an ECG- and respiratory-gated segmented fast gradient echo cine sequence with steady-state precession (FISP). A flip angle (FA) of 15°, echo time (TE) of 1.2 ms, 128 segments, and a repetition time (TR) of about 6-8 ms (depending on the heart rate) were used to acquire 16 frames per heart cycle with a field of view (FOV), 30 × 30 mm^2; matrix size after zero filling (MS), 256 × 256; slice thickness (ST), 1 mm; the number of averages (NA), 2; acquisition time (TAcq) per slice for one cine loop, ∼1 min. In cases of inadequate ECG recording, images were acquired with a retrospectively gated fast low-angle shot sequence (Intragate FLASH, Bruker) using a FA 10°, TE 1.26 ms, TR 5.82 ms, FOV 30 × 30 mm2, MS 256 × 256, TAcq 1.5 min. For retrospective gating, a navigator slice was placed near the base of the heart, where the signal is primarily modulated by the periodically changing atrial and aortic blood [133]. Routinely, 8–10 contiguous short-axis slices were required for complete coverage of the LV. Longitudinal slices orientated perpendicular to the atrio-ventricular level served to ensure appropriate scanning of the entire heart from base to apex. For evaluation of functional parameters, ventricular demarcations in end-diastole and -systole were manually drawn with the ParaVision Region-of-Interest (ROI) tool.

2.2.2.2.2. Relaxation times

Relaxometric maps of T1 and T2 were taken in midventricular short-axis orientation., We used an approach introduced by Coolen [134] based on a retrospectively triggered fast low-angle shot sequence and different flip angles (2,5,8,11 and 14°). Image intensities were fitted to the Ernst equation in a pixel-wise manner for determination of T1 (see Haberkorn et al [135] for details). The navigator slice was placed near the base of the sternum to the top. Short echo times (1.26 ms) and repetition times (5,82 ms) preserved the steady state and allowed acquisition of excellent T1 maps without artifacts (in plane resolution, 117 x 177 μm^2; field of view, 30 x 30 mm^2; matrix size, 256 x256 after zero filling). T2 maps were calculated from images recorded with a gated multi-echo sequence (16 echoes, separated by an echo time (TE=5 ms), repetition time (TR)=500 ms, acquisition time (TAcq=2 min), slice thickness (ST=1mm), field of view (FOV=30x30mm), matrix size (MS=128 x 128), and scan number (NS=2). For details please refer to Bönner et al, 2014 [136].

2.2.2.3 ^{19}F MRI measurements

2.2.2.3.1. Functionalization of ^{mNP}PFCs

PFCs were equipped with peptide ligands using the sterol-based post-insertion technique (SPIT) [130]. For this, peptides were coupled via free cysteines to cholesterol-PEG2000 - maleimide anchors exploiting the formation of a stable thioether after the reaction of the cysteine SH-group with maleimide of the anchor. For conjugation, 280 µg of the peptide (suspended in phosphate glycerol buffer) was added to 300 µg of cholesterol- PEG2000 - maleimide (1 µg/µl, suspended in phosphate glycerol buffer), and the volume was adjusted to 650 µl with phosphate glycerol buffer. The solution was incubated overnight at 22 °C under constant stirring. On the next day, 650 µl of the cholesterol-PEG2000-peptide conjugate was mixed with 650 µl of preformed PFCs and incubated at 22 °C for 3 h which led to the spontaneous insertion of the cholesterol conjugate into the lipid layer of the PFCs [137]. For targeting neutrophils, PFCs were equipped with a unique murine neutrophil-specific peptide as previously described [138]. Functionalized PFCs were stored at 4 °C under light protection.

2.2.2.3.2. ^{mNP}PFCs sternal injection

Mice were anesthetized with isoflurane (2.0%) using a home-built nose cone. The reflexes pinching in the tail and hind feet were performed to make sure that mouse is sufficient anesthetized. Under microscopic view, between the 2rd and the 3th rib the hairs were removed, the tissue dissected, followed by a small cut to separate skin, muscle and tissue covering the sternum. Thereafter, a total volume of 4 µl of the PFC emulsion for targeting

neutrophils was injected directly into the 3 segments of the sternum before induction of MI using a Hamilton syringe, shown in Figure 13.

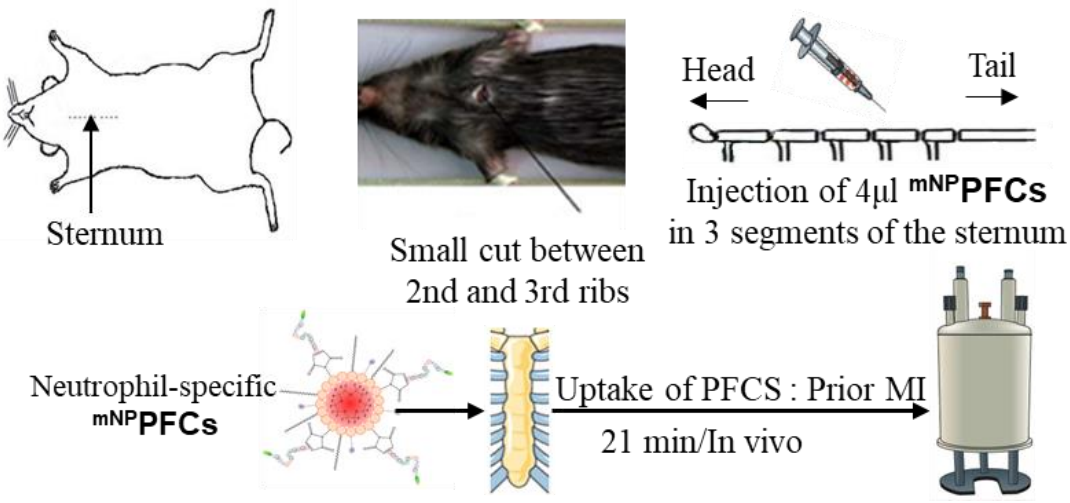

Fig. 13: Sternal injection of ^{mNP}PFCs prior MI. Injection of ^{mNP}PFCs to label all neutrophils in the sternum bone marrow prior inflammation followed by visualization by combined $^{1}H/^{19}F$ MRI in vivo.

Afterwards, a 7-0 Prolene running suture (Ethicon, Norderstedt, Germany) was used to to close the wound. 3 h after injection, the uptake of ^{19}F was visualized by high-resolution MRI.

2.2.2.3.3. Tracking of neutrophils using ^{19}F MRI

Male 10–12-week-old C57BL/6 mice (in total, n = 3) ranging from 20 to 30 g in body weight (BW) were used. After injection of ^{19}F and induction of MI, mice were anesthetized as described above. In vivo $^{1}H/^{19}F$ MRI (as in Figure 14) was used to track the fate of labeled neutrophils to the infarcted regions.

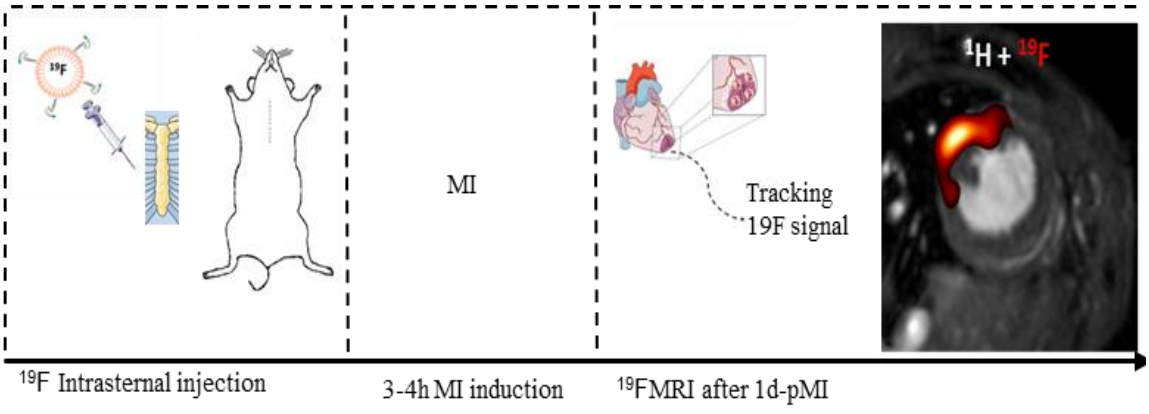

Fig. 14 : In vivo 19F MRI after 24h following the MI. In vivo visualization by combined 1H/19F MRI to track the fate of neutrophils with 19F signals originating in the injected location into the infarcted heart.

Ex vivo $^{1}H/^{19}F$ MRI investigation 24 hours after induction of MI was made after sacrificing the mouse and heart harvesting for the sternum and infarcted heart.

2.2.2.3.4. ^{19}F MRI protocol

As described above, for tracking of neutrophils by ^{19}F MRI, 4 µl of ^{mNP}PFCs were injected into the sternum 1 day prior MI to allow adequate ^{19}F labeling of neutrophils. ^{19}F MRI was recorded with non-gated multislice RARE sequence (3 slices, RARE factor=64, TE=104,4 ms, TR=4.5 s, TA=19.2 min, matrix size (MS=64x64), ST=2 mm, NS=256) for the sternum prior MI and post MI. For MRI analysis, first cine loops were acquired followed, then the resonator was tuned to ^{19}F and anatomical corresponding ^{19}F MR images were acquired. Afterwards, the resonator was retuned to ^{1}H for acquisition of LGE images. The experimental protocol took around 60 min and was well tolerated by all mice, which recovered from anaesthesia within 1-2 min after removal of the nose cone.

2.2.2.4 Flow cytometry analysis

2.2.2.4.1 Bone marrow tissues preparation and analysis

After killing the animals by cervical dislocation, the sternum, tibia, and femur tissues were harvested. The upper layers of all bone marrow tissues were removed and the bones were exposed using a microscope.

Table 9 : List of antibodies used for bone marrow analysis

Target	Fluorochrome	Vendor	Reference	Clone
B220	PE-Cy7	BD Biosciences	552772	RA3-6B2
c-kit	RPE	eBioscience	12-1171-83	2B8
CD11B	APC/Cy7	Biolegends	101226	M1/70
CD45	APC	Biolegends	109814	104
Ly6C	FITC	BD Pharmingen	553104	AL-21
Ly6C	APC	BD Biosciences	560595	AL-21
Ly6G	FITC	Biolegends	127606	1A8
Ly6G	PerCP/Cy5.5	Biolegends	127616	1A8
Ly6G	APC	Biolegends	127614	1A8
Ly6C	PerCP/Cy5.5	Biolegends	128012	HK1.4

The marrow from the sternum was obtained by crushing and by flushing of the long bones (tibia & femur). The cell suspension was prepared by mincing the sternum and femur for 4 min in the buffer and then filtered through a 40-µm cell strainer into a 50-ml Falcon tube. The centrifugation was done at 340 g for 6 min at 5 °C for all samples which were resuspended in 300 µL buffer. The samples were kept at 4 °C until staining.

After homogenization, the preparation was filtered, washed off in buffer, spun, and resuspended in PBS. After staining samples, were fixed (9 min on ice). The list of antibodies used for the experiments in provided in Table 9. All samples were recorded on FACSCanto II (BD Biosciences) and data were analyzed with FlowJo software (FACSDiva 6 or FlowJo 7.1). Cell numbers per sample were calculated as total cells per sample multiplied by the percentage of live cells obtained from the appropriate flow cytometry gate. After gating out the mature myeloid cells were identified as CD45, a subpopulation of myeloid cells was defined as follows: for neutrophils (Ly6G) and monocytes (Ly6C).

2.2.2.5 Statistical analysis

SPSS Statistics software version 29.0.0 (IBM, Armonk, New York, USA) and GraphPad Prism version 9.5 (Graphpad Software Inc., San Diego, California, USA) were used for statistical analysis. For the investigation of the normal distribution, unless otherwise reported, a two-tailed Mann-Whitney U test or a Wilcoxon test for more than two independent groups was used for subgroup comparisons. If the p-value is less than 0.05, the result is considered significant; results with $p<0.01$ are considered highly significant. In addition, all p-values <0.2 were written out in the graphs. The arithmetic mean is given with the associated standard deviation, marked by the symbol "±". Correlations are Spearman correlation for non-normal data and Pearson correlation for normal data. A repeated measure analysis of variance (ANOVA) was used for subgroup comparisons within paired samples. In addition, multiple linear regression was used to examine different covariates and their influence. A robust multiple linear regression was then calculated using bootstrapping. A sample size of 100 samples was chosen.

2.2.2.6 Ethics

Animal experiments were performed in accordance with the European Union guidelines described in the directive 2010/63/EU and were approved by North Rhine Westphalian State Agency for Nature, Environment and Consumer Protection (LANUV = Landesamt für Natur, Umwelt und Verbraucherschutz Nordrhein-Westfalen), Germany. Human studies from healthy humans were conducted and approved by the Ethics Committee of the Heinrich Heine University, Düsseldorf, Germany. All healthy volunteers gave written informed consent to the collection and use of data in this study.

3. Results

3.1. Human

In this study, a cohort of STEMI patients was evaluated at 3 time points after revascularization (1-day, 5-day past STEMI, and 6 months follow-up STEMI). In addition, age-matched healthy volunteers and patients with stable coronary artery diseases (SCADs) were used as separate control groups. All subjects/patients received parametric mapping (T1+T2) of the heart including the closely located sternum. Furthermore, in a subset of STEMI patients to mDixon sequences were employed for the determination of fat/water contents. Data for cardiac function and blood biomarkers were obtained at the same time from the acute STEMI phase to the 6 months follow-up.

3.1.1 Sternal T1 relaxation time

In a first step, a quantitative evaluation of the sternum T1 values based on the mean from regions of interest (ROIs) (Figure 15b; n=193 STEMI patients) was carried out. Analysis of sternal T1 showed a significant increase on the day after STEMI and decreased after 5 days to the 6 months follow-up STEMI (Figure 15c; n=193 STEMI patients).

a)

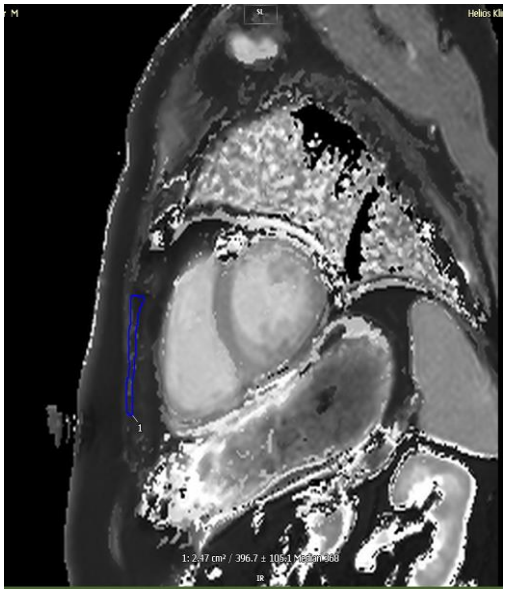

b)

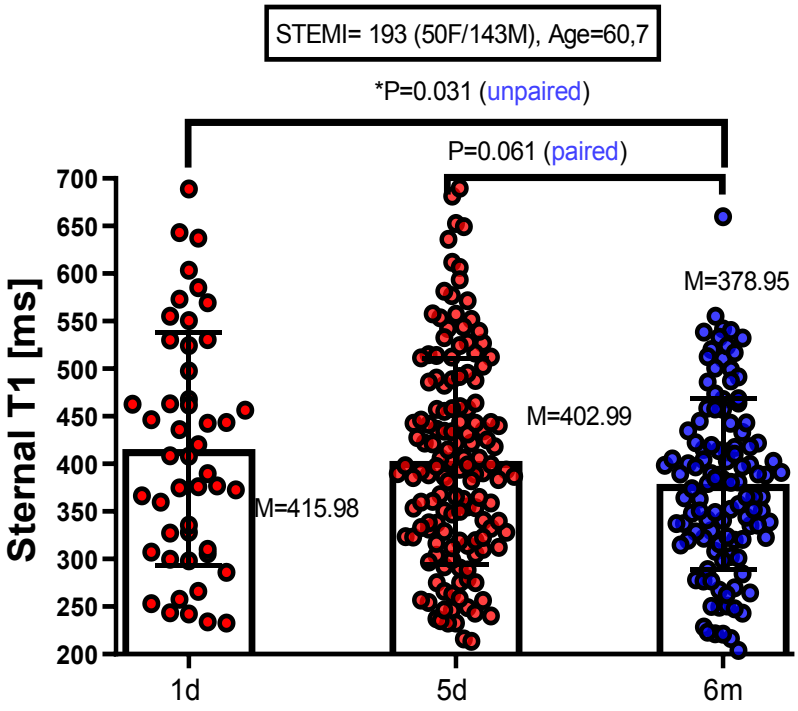

c)

Fig. 15: Sternal T1 of STEMI cohort. T1-weighted MRI image showing: **a**) manually taken ROI of the sternum tissue on T1 map; **b**) Copied ROI from T1-weighted slices for determination of sternal T1; **c**) Distributed values of sternum T1 at day one past STEMI (T1= 415.98 ± 89.49 ms), 5 days after STEMI (402.9 ±108.1 ms) to 6 months follow-up STEMI (378.95 ±121.9 ms). The data is presented as mean ± SD. The evaluation was carried out using two-tailed Mann-Whitney test, for significant $P<0.05$, n=193 patients.

However, due to the high standard deviation and an insufficient delineation of the sternum from surrounding tissue in several cases, we decided to omit further analysis of sternal T1 maps in this context.

3.1.2 Sternal T2 relaxation time

Next, we analyzed T2 as another tissue-specific MR parameter. In Figure 16, a & b, the measurements of the sternum T2 values are based on the mean from regions of interest (ROIs) and taken as maximum by spatial standard deviation inside the ROIs placed on the T2 map.

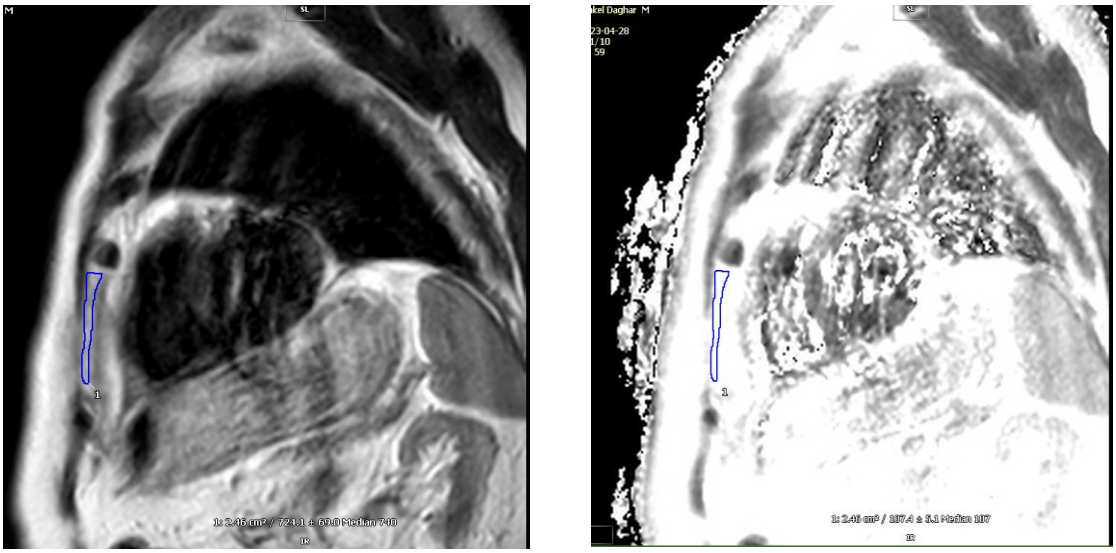

a) b)

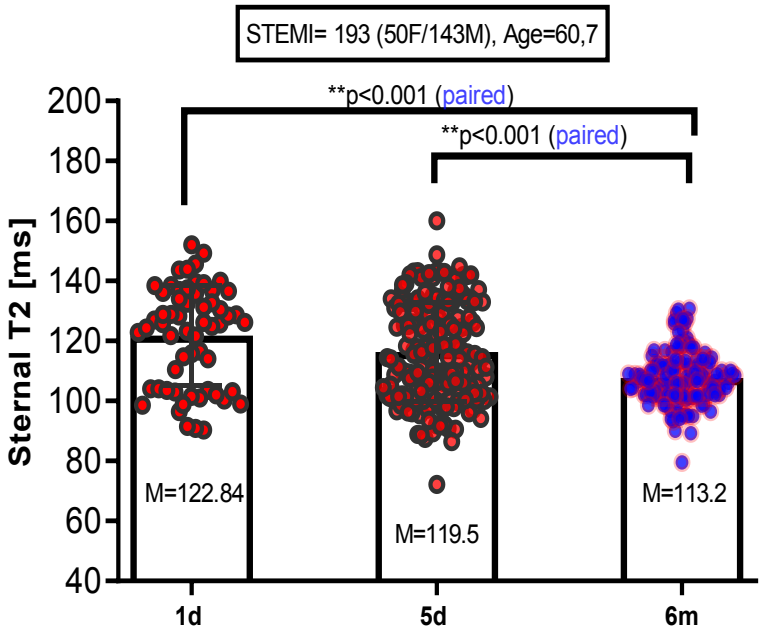

c)

Fig. 16: Sternum T2 of STEMI cohort. T2-weighted MRI image showing: **a**) manually drawn ROI of the sternum tissue; **b**) Copied ROI from T2-weighted slices for determination of sternal T2 **c**) The distributed values of sternal 1 day T2 (T2=122.84 ± 16.45 ms), 5 days of acute STEMI (T2=119.5 ± 16.61 ms), and after 6 months follow-up (T2=113.2 ± 8.8 ms). The data is presented as mean ± SD. The evaluation was carried out using two-tailed Mann-Whitney test, significantly different (P<0.05), n=193 patients.

The sternal T2 values ranged from (T2=122.84 ± 16.45 ms) at day one past STEMI, then decreased after 5 days of STEMI (T2=119.5 ± 16.61 ms), and then significantly dropped after 6 months follow-up (T2=113.2 ± 8.8 ms), which indicates that sternum tissue in the STEMI phase undergoes significant alterations.

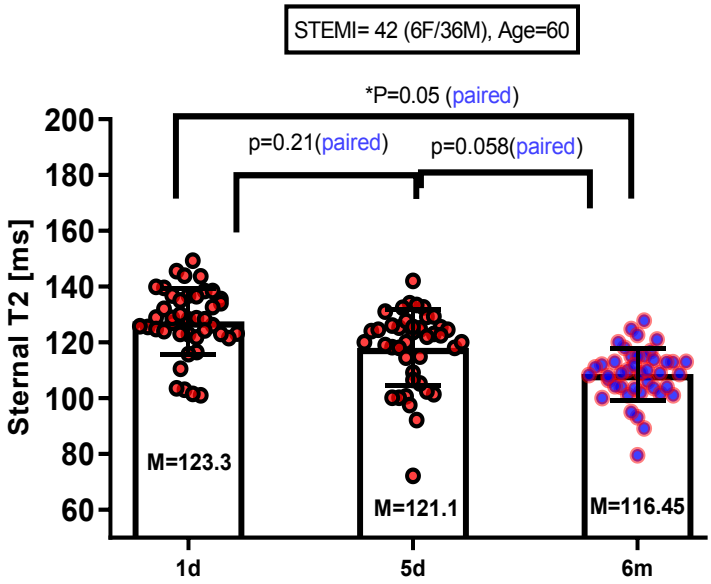

a)

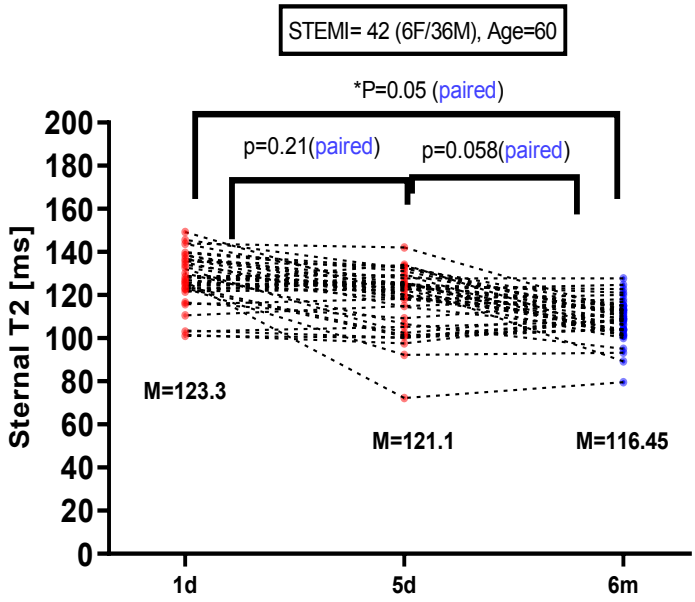

b)

Fig. 17: Sternal T2 time of same STEMI patients at 3 time points. a) Mean and SD of sternal T2 for 42 STEMI patients in 3 points of time, day one of acute STEMI (T2=122.84 ± 11.72 ms), 5 days of acute STEMI (T2=119.5 ± 13.6 ms), and after 6 months follow-up (T2=113.2 ± 9.3 ms); **b**) single plot values of the course of sternal T2 values in the 42 patients receiving repeated CMR imaging after STEMI. The data is presented as mean ± SD. The evaluation was carried out using two-tailed Mann-Whitney test, significantly different ($P<0.05$), n=42 Patients.

By looking at the distributed data in Figure 16c, particularly to the 1 day past STEMI, not all patients were able to receive an MRI on 1 day past STEMI compared to 5 days and 6 months. So, by taking only those STEMI patients who repeated the same protocol on day 1, 5 days, and 6 months past STEMI, the results still show a significant increase in sternum

T2 values (Figure 17a+b) at day one and dropping 5 days to 6 months follow-up.

STEMI patients after 6 months of recovery are very controlled in the clinical trials, thus we also recruited aged-matched healthy volunteers with no history of any cardiac diseases for further comparison with the STEMI cohort. The results revealed similar values for sternal T2 in healthy volunteers as after 6 months of follow-up post STEMI, (as shown in Figure 18) further supporting the notion that the increased T2 values observed at day 1 are STEMI-specific and are approaching baseline in the subsequent healing phase. Additionally, this indicates that 6 months post STEMI is an adequate control for the STEMI cohort study.

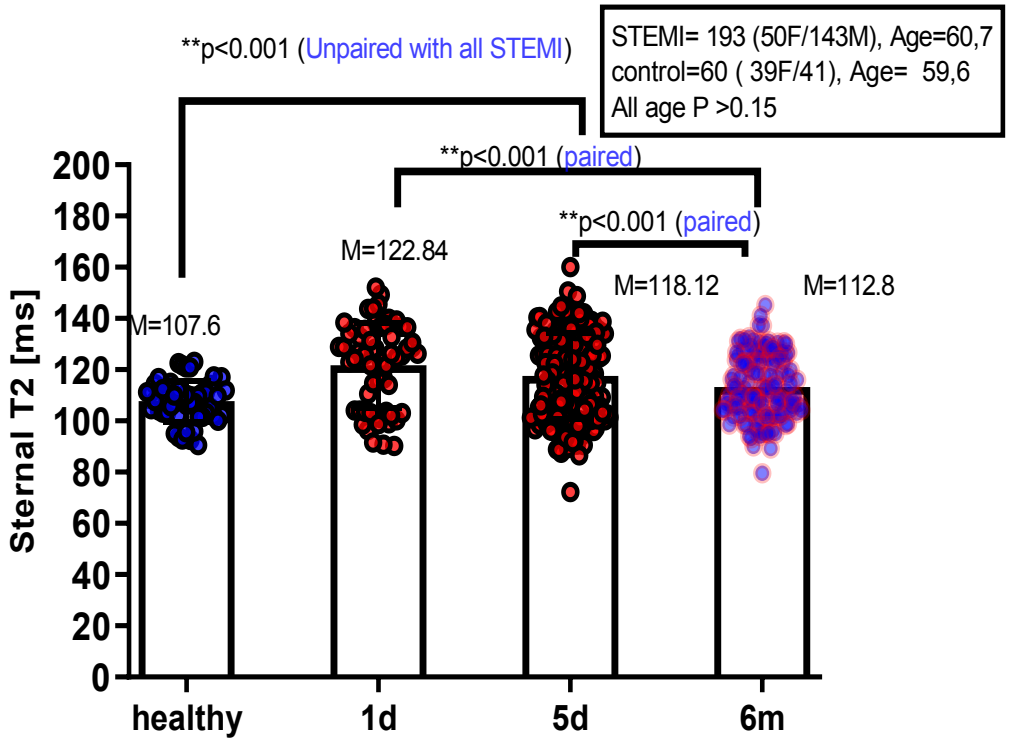

Fig. 18: Sternal T2 of STEMI and healthy volunteers (control). For healthy volunteers (T2=107.6 ± 1.1 ms), day one of acute STEMI (T2=122.84 ± 11.72 ms), 5 days of acute STEMI (T2=119.5 ± 13.6 ms), and after 6 months follow-up (T2=113.2 ± 9.3 ms). The data is presented as mean ± SD. The evaluation was carried out using two-tailed Mann-Whitney test, significantly different (P<0.05), n=193 STEMI patients and n=60 healthy volunteers.

Also, we involved patients with stable coronary artery diseases (SCADs) to investigate the sternum before the acute STEMI event as shown in Figure 19, because patients with SCADs are supposed to develop MI after some time.

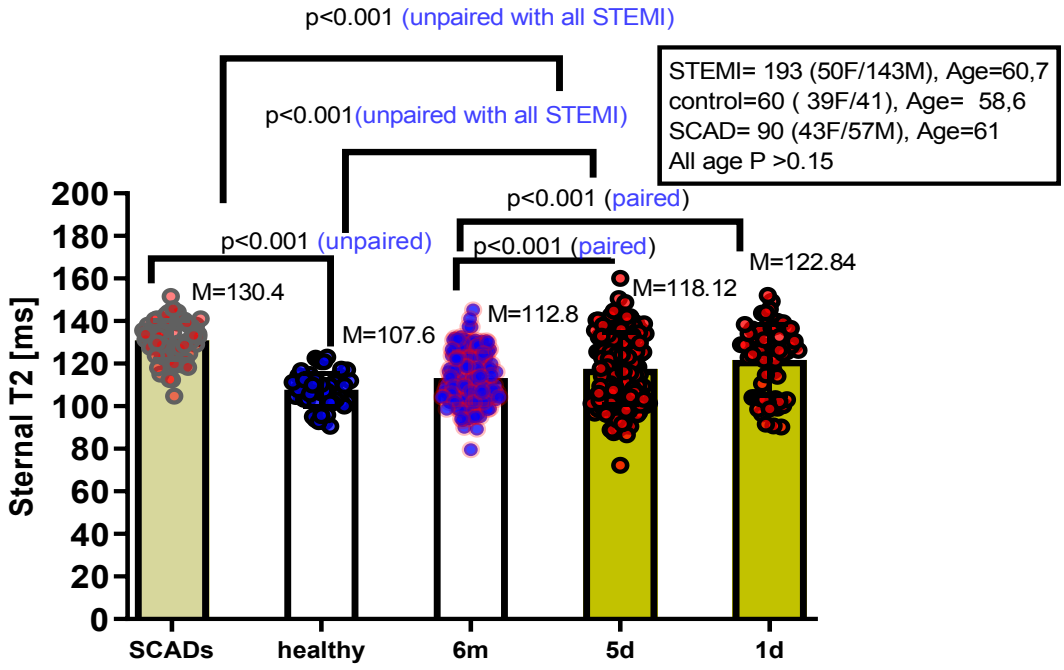

Fig. 19: Sternal T2 of STEMI, control, and SCADs. Sternum for patients with SCADs (T2=130.4 ± 11 ms healthy volunteers (T2=107.6 ± 1.1 ms), day one of acute STEMI (T2=122.84 ± 11.72 ms), 5 days of acute STEMI (T2=119.5 ± 13.6 ms), and after 6 months follow-up (T2=113.2 ± 9.3 ms). The data is presented as mean ± SD. The evaluation was carried out using two-tailed Mann-Whitney test, significantly different (P<0.05), n=73 patients with SCADs, n=60 healthy volunteers, and n=193 for STEMI patients.

Interestingly, the analysis of patients with SCAD revealed that the sternum exhibited the highest values for T2 as compared to all other groups.

3.1.3 Humerus & sternal T2 of STEMI cohort

In order to verify, whether the observed effects are specific for the sternal bone marrow, we extended our analysis in a subset of patients to the humerus bone marrow. The results in Figure 20 show that the humerus has even higher values of T2 (T2=133.2 ± 8.9 ms) than the sternum (T2=105.02±7.9 ms) during acute STEMI. However, these are only very preliminary results and it has to be clarified if this is also only a transient effect, which could be attributed as a consequence of STEMI.

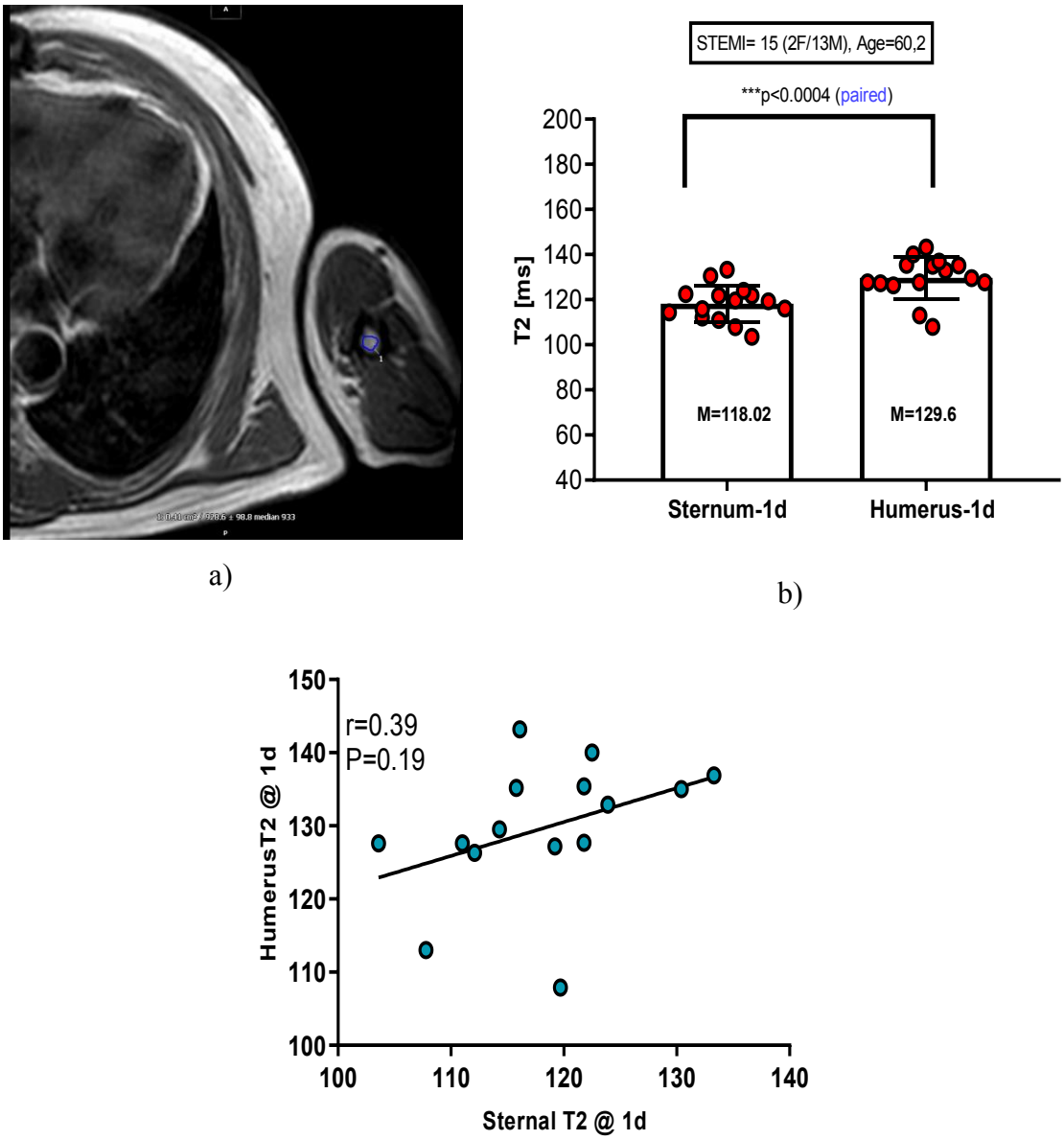

Fig. 20: T2 of sternum and humerus in STEMI . T2-weighted MR image in the first column showing: **a**) Humerus tissue and manually drawn ROI on T2 map; **b**) T2 values of sternal (T2=118.02 ± 7.9 ms) and humerus (T2=129.6 ± 9.3 ms) after one day post STEMI. **c**) Linear regression of sternum and humerus T2 values. The data is presented as mean ± SD. The evaluation was carried out using two-tailed Mann-Whitney test, significantly different (P<0.05), n=15 patients. The correlations were moderate to weak, with Spearman's rhos.

3.1.4 T2 of further tissues after STEMI

Further, we investigated other tissues to see whether further organs were affected in a similar way as the sternum during the STEMI phase and 6 months follow-up, and the result is shown in Table 10.

Table 10 : T2 for adjacent tissues compared to the sternum

Relaxation time for the sternum, liver, spleen, epicardial fat, subcutaneous fat, and heart tissues (infarcted and healthy regions). The evaluation was carried out using two-tailed Mann-Whitney test, significantly different (P<0.05), n=40 STEMI Patients.				
Organ	T2-1D	T2-5D	T2-6M	P value (1D vs 6M)
Sternum	122.1 ± 4.7	116.6 ± 5.2	114.03 ± 5.1	0.001
Liver	64.17 ± 9.6	60.02 ± 9.1	58.4 ± 10.1	0.04
Spleen	95.2 ± 7.3	91.16 ± 6.4	93.6 ± 6.6	0.37
Epicardial fat	141 ± 20.9	137.5 ± 19.2	136.6 ± 23.4	0.99
Subcutaneous fat	140.2 ±4.5	131.5 ± 5.1	129.3 ± 4.7	0.007
Muscle	47.1 ± 47.0	45.9 ± 6.2	44.6 ± 6.6	0.08
Infarcted myocardial tissue	73.8 ± 10.3	65.8 ± 11.4	59.2± 9.8	0.06
Healthy myocardial tissue	64.6 ± 8.6	64.2 ± 8.8	58.2 ± 8.7	0.08

We can see that there are minor changes in T2 for spleen, epicardial fat, Infarcted myocardial tissue, and muscle, which are significantly different. Interestingly, liver and subcutaneous fat showed a similar trend as the sternum, while there was an increase in the T2 for heart tissue indicating the transient development of edema in the acute phase of STEMI.

3.1.5 Sternal fat content

In order to clarify the underlying cause of the transient increase in sternal T2 after STEMI, we further analysed in a subset of patients (n=23) sternal fat content by mDIXON sequences, This subcohort included 23 STEMI patients, with a mean age of 61 years, and a body mass index of 16-26 kg/m^2. Here, lower sternal fat values were observed during the STEMI phase (64.4%) compared to (65.73%) 6 months of follow-up, as shown in Figure 21.

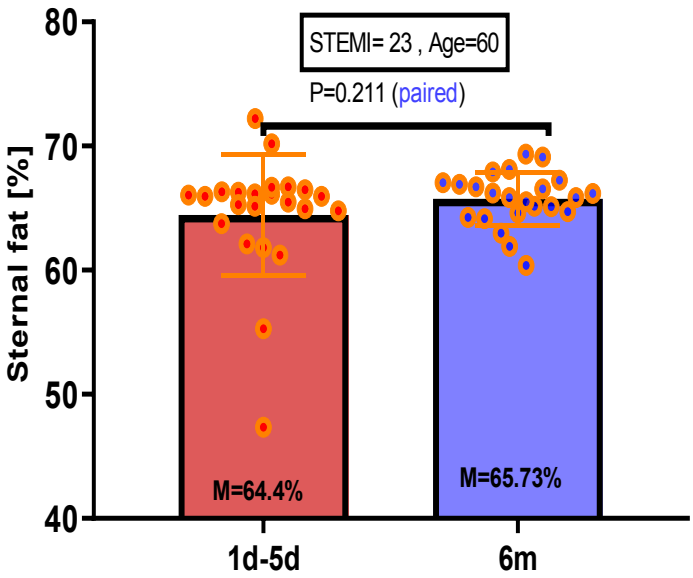

Fig. 21: Sternal fat content in STEMI cohort. Sternal fat value is 64.4% in acute STEMI (1d-5d) and 65.73% after 6 months of follow-up. The data is presented as mean ± SD. The evaluation was carried out using two-tailed Mann-Whitney test, significantly different ($P<0.05$), n=23 patients.

Linear regression of sternal fat and T2 at day 1 post STEMI revealed a significantly inverse correlation (Figure 22, a&c) which (i) excludes an increase of sternal fat as a cause of the transient rise in T2 and (ii) might reflect an enhanced substrate consumption associated with the activation of emergency hematopoiesis.

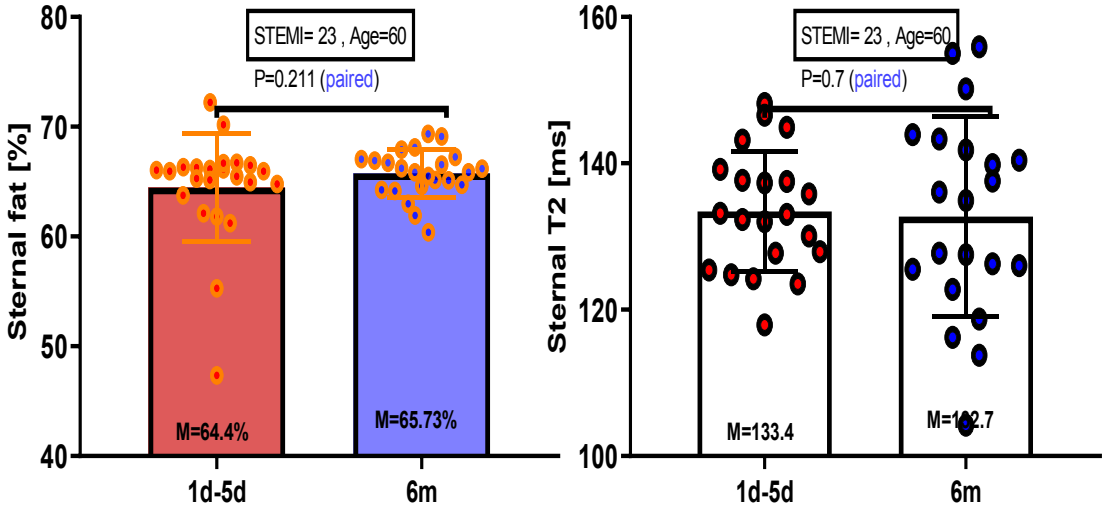

a) b)

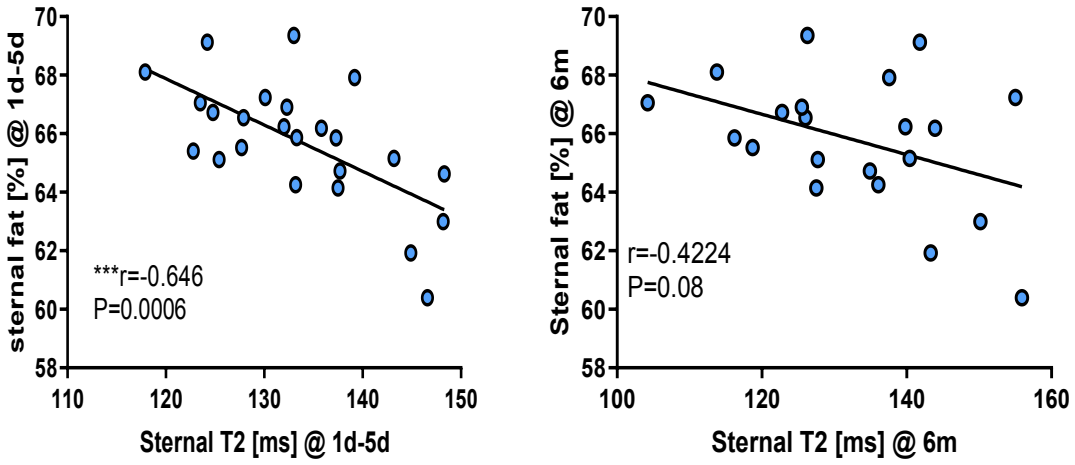

c) d)

Fig. 22: Association between fat content and sternal T2. **a**) Mean and SD of sternal fat content in acute STEMI and 6 months follow-up; **b**) Sternal T2 values in STEMI and 6 months of recovery in the same patients receiving mDIXON fat quantification; **c**) Linear regression between fat content and T2 of the sternum during acute STEMI showed a significant inverse correlation; **d**) Linear regression between fat content and T2 of the sternal after 6 months follow-up did not show a significant correlation. The data is presented as mean ± SD. The evaluation was carried out using two-tailed Mann-Whitney test, significantly different ($P<0.05$), n=23 patients. The correlations were moderate to strong with Spearman's rhos.

3.1.6 STEMI MRI characterization and sternal T2

3.1.6.1 MRI characterization of STEMI cohort

In the following cardiac function, volumes and infarct characteristics that were assessed by MRI on day 5 and 6 months after STEMI are illustrated.

a)

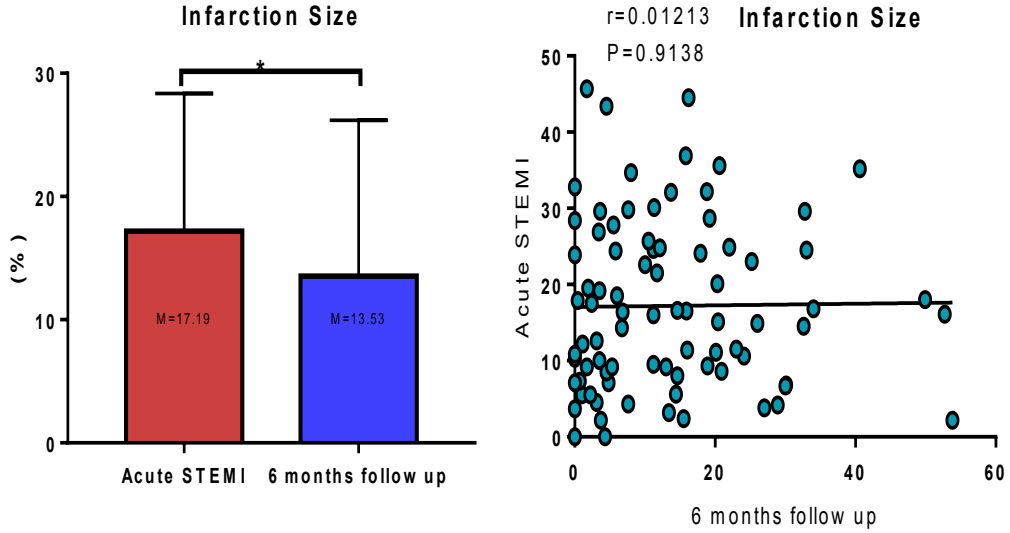

b)

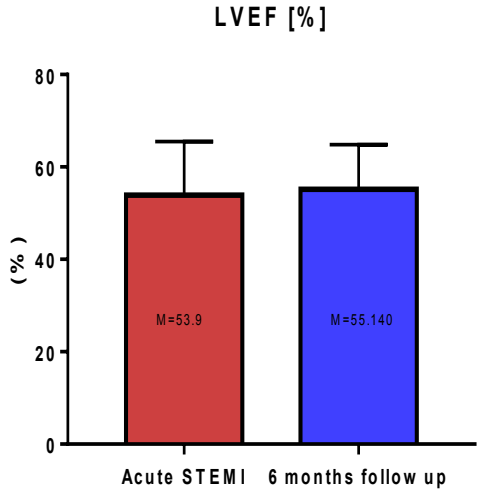
LVEF [%]
(%)
80
60
40
20
0
M=53.9
M=55.140
Acute STEMI
6 months follow up

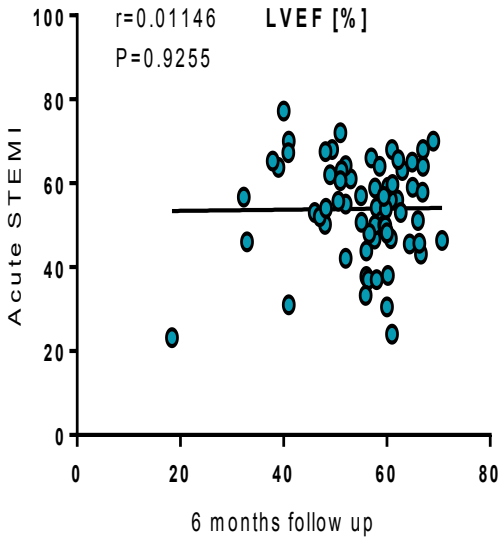
r=0.01146
P=0.9255
LVEF [%]
Acute STEMI
100
80
60
40
20
0
0
20
40
60
80
6 months follow up

c)

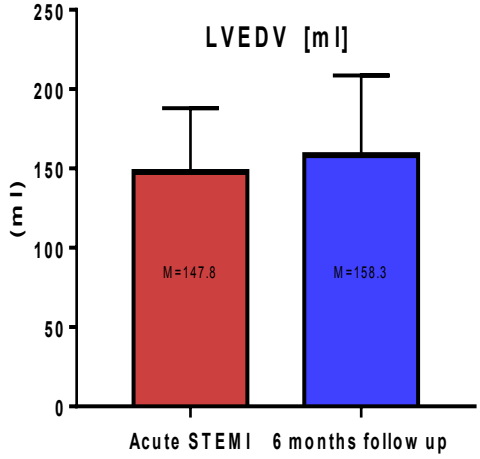
LVEDV [ml]
(ml)
250
200
150
100
50
0
M=147.8
M=158.3
Acute STEMI
6 months follow up

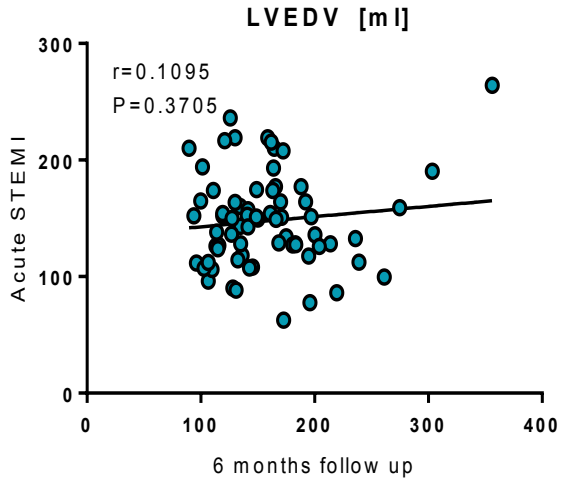
LVEDV [ml]
r=0.1095
P=0.3705
Acute STEMI
300
200
100
0
0
100
200
300
400
6 months follow up

d)

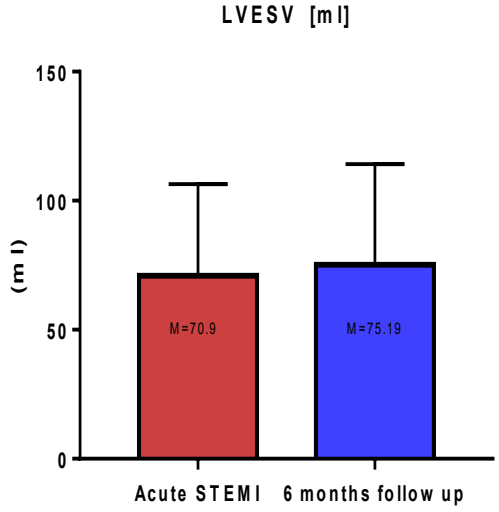
LVESV [ml]
(ml)
150
100
50
0
M=70.9
M=75.19
Acute STEMI
6 months follow up

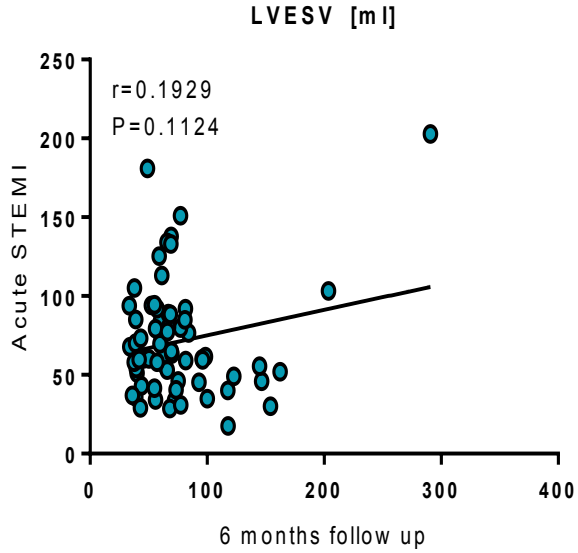
LVESV [ml]
r=0.1929
P=0.1124
Acute STEMI
250
200
150
100
50
0
0
100
200
300
400
6 months follow up

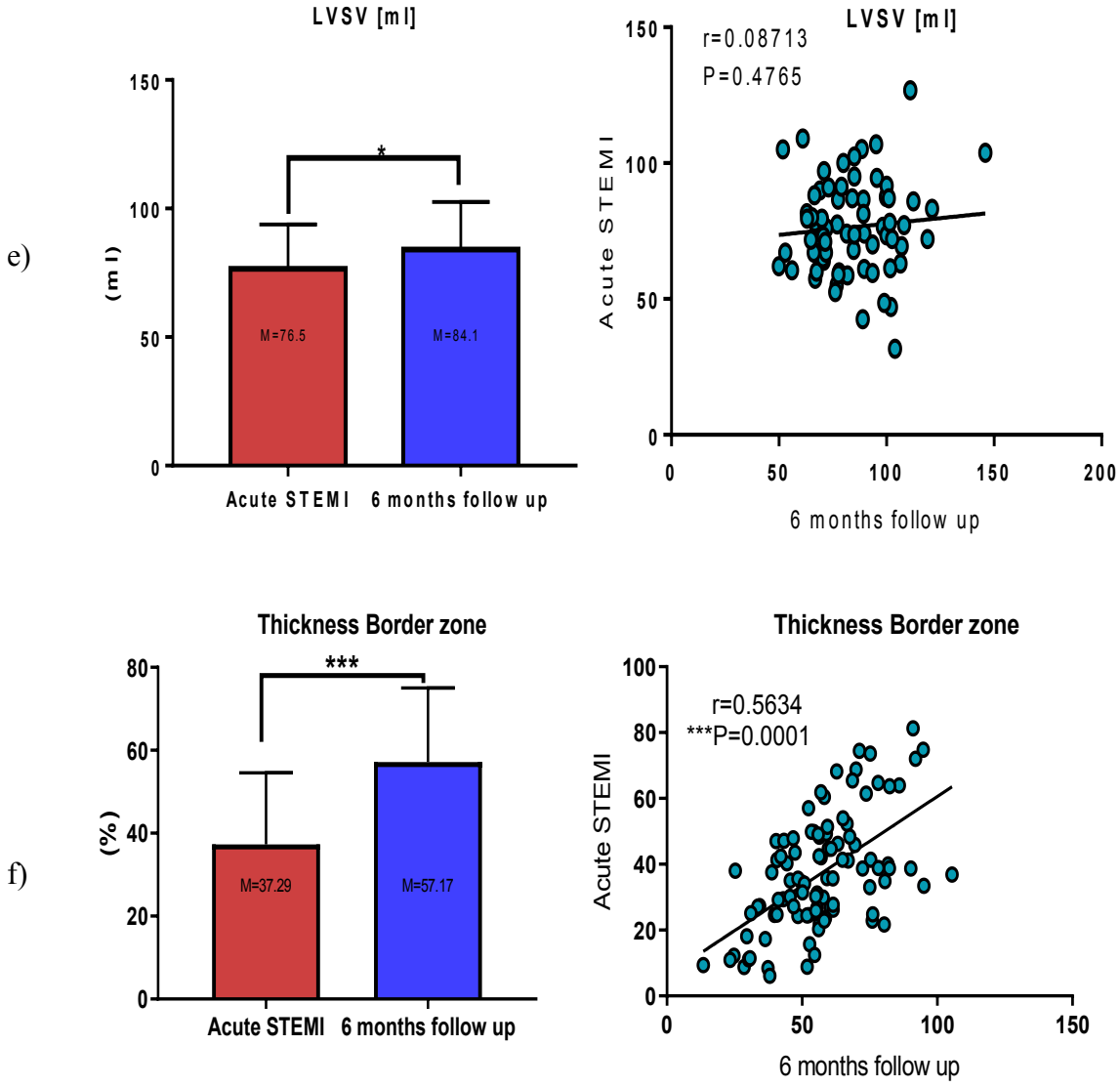

Fig. 23: Cardiac functions for STEMI and 6 months follow-up by MRI. Functional parameters which were calculated include infarction size (**a**), Left ventricular ejection fraction (LVEF) (**b**), end-diastolic volume (LVEDV) (**c**), end-systolic volume (LVESV) (**d**), stroke volume of the left ventricle (LVSV) (**e**), thickness border zone (**f**). The left column shows the mean and SD of cardiac functions in acute STEMI to 6 months follow-up. right column illustrates linear regression between cardiac functions in acute STEMI and 6 months follow-up. Data are presented as mean ± SD, n=193 STEMI patients. The evaluation was carried out using two-tailed Mann-Whitney test, significantly different (P<0.05), n=189 patients. The correlations were weak to strong, with Spearman's rhos.

As expected during the acute phase of STEMI, patients were characterized by a compromised cardiac function as compared to the 6 months follow-up. During this time, there was a significant recovery of left ventricular ejection fraction (LVEF) from 5 day to 6 months after STEMI, although the 5 day LVEF was still in the normal value range as referenced to recent ESC guideline (Figure 23b in acute STEMI = 53.9 % compared to 6 months follow up = 55.14 %). This was accompanied by an increase in stroke volume

(LVSV) (Figure 23e in acute STEMI = 76.5±7 mL than 6 months follow up = 84.1±8 mL) and in wall thickening of the border zone (Figure 23f) of infarction which increased to 57.17 % in 6 months follow-up compared to 37.29% in the acute phase. The results also show moderate increases in end-diastolic volume (LVEDV) (Figure 23c in acute STEMI =147.8±3.4 mL compared to 6 months follow-up=158.3±12 mL) and end-systolic volume (LVESV) (Figure 23d, in acute STEMI=70.9±5 mL than 6 months follow-up =75.19±2 mL). Also, the area of LGE-positive myocardium declined from 17.19% in acute STEMI to 13.57% after 6 months of follow-up.

3.1.6.2 Association of MRI parameters to sternal T2 values

Cardiac volumes and infarct characteristics are of major importance after STEMI for risk assessment, but we lack a complete understanding of its effects in response to the activation of bone marrow during injury. Therefore we used the MRI data and correlated them to the sternum T2 values to characterize their relation to alterations in the sternal bone marrow posts STEMI. As a result, we found a negative significant correlation with edema size (Figure 24a), which might suggest a beneficial effect on increasing sternum T2 values (and enhanced activation of sternal bone marrow) on development of edema.

In addition, for age and BMI (Figure 24b+c) no correlation was found with sternal T2, indicating that these parameters have no impact on the tissue texture in the sternum in the acute phase of STEMI. After STEMI, the size of the infarction is pivotal in estimating the tissue damage, as well as the immune response for removal of tissue debris as well as the subsequent healing phase. , by looking at the correlation with sternum T2 RT (Figure 25 a,b,c), we hypothesize that decrease in sternum T2 RT might reduces scar size.

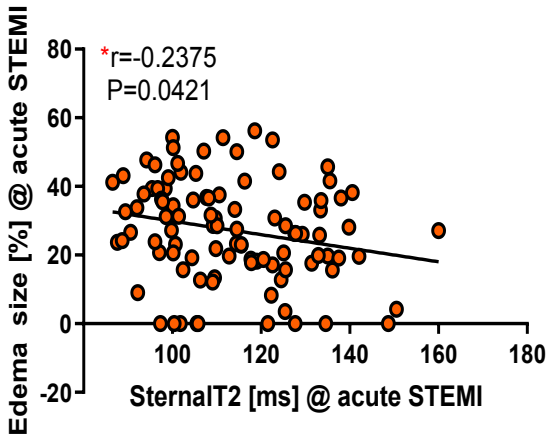

a)

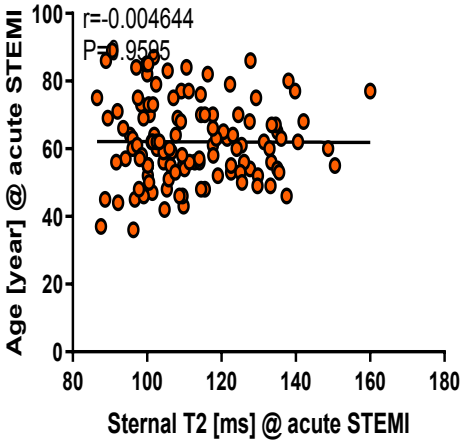

b)

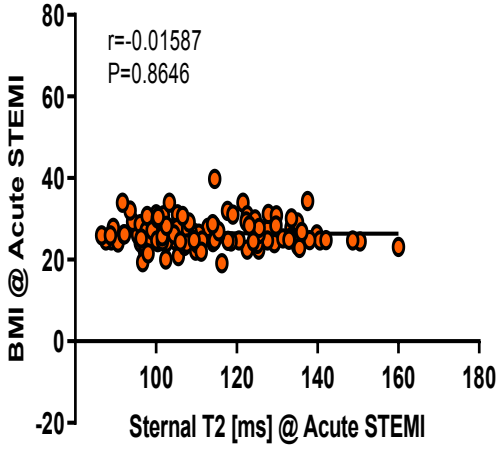

c)

Fig. 24: Linear regression of edema size, age, BMI, and sternal T2. a) Linear regression between edema size (r=-0.2354, P=0.0421) and sternal T2 at 5-day post STEMI; **b**) Linear regression between age (r=-0.004644, P=0.9595) and sternal T2; **c**) Linear regression between BMI (r=-0.01587, P=0.8646) and sternal T2 The evaluation was carried out using two-tailed Mann-Whitney test, significantly different (P<0.05), n=189 patients. The correlations were moderate to weak, with Spearman's rhos.

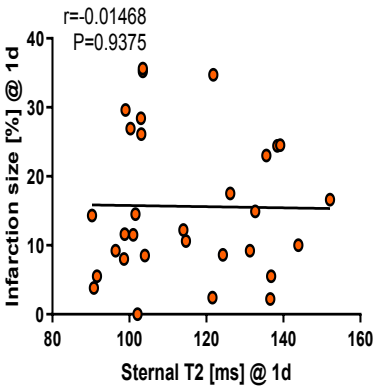

a)

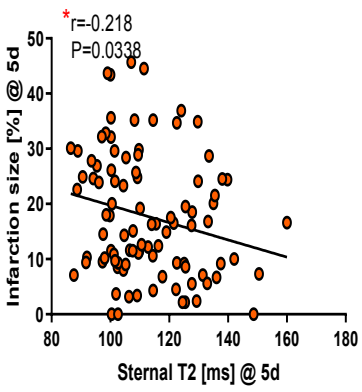

b)

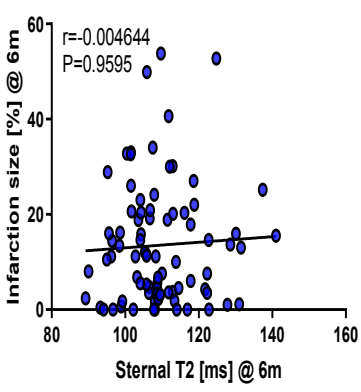

c)

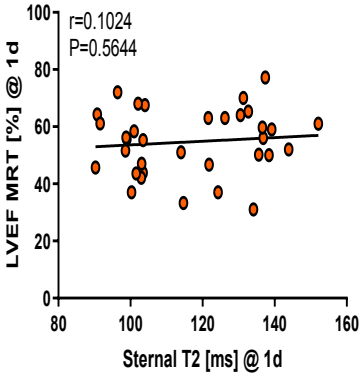
r=0.1024
P=0.5644
LVEF MRT [%] @ 1d
Sternal T2 [ms] @ 1d

d)

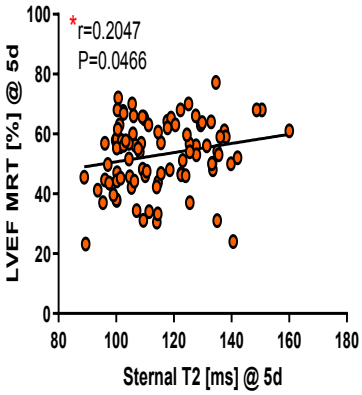
*r=0.2047
P=0.0466
LVEF MRT [%] @ 5d
Sternal T2 [ms] @ 5d

e)

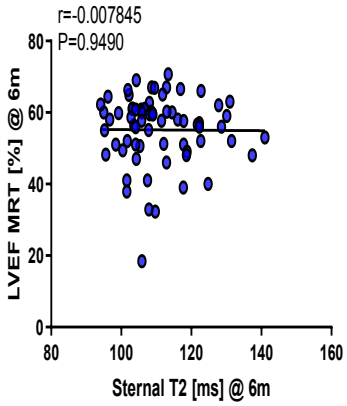
r=-0.007845
P=0.9490
LVEF MRT [%] @ 6m
Sternal T2 [ms] @ 6m

f)

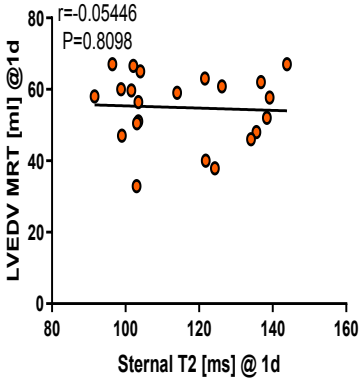
r=-0.05446
P=0.8098
LVEDV MRT [ml] @1d
Sternal T2 [ms] @ 1d

g)

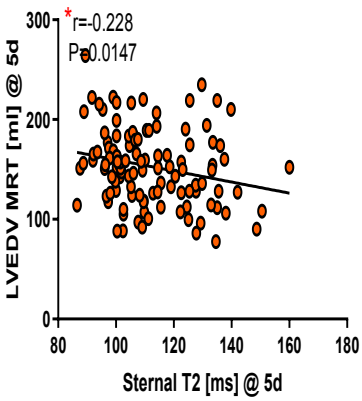
*r=-0.228
P=0.0147
LVEDV MRT [ml] @ 5d
Sternal T2 [ms] @ 5d

h)

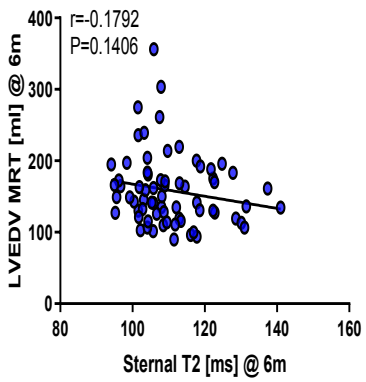
r=-0.1792
P=0.1406
LVEDV MRT [ml] @ 6m
Sternal T2 [ms] @ 6m

i)

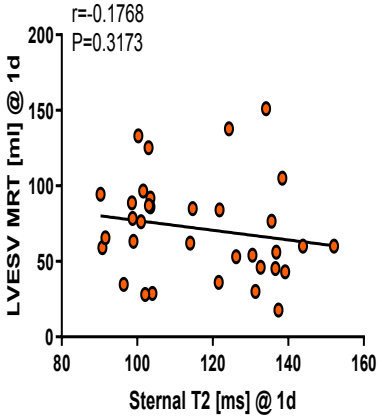
r=-0.1768
P=0.3173
LVESV MRT [ml] @ 1d
Sternal T2 [ms] @ 1d

j)

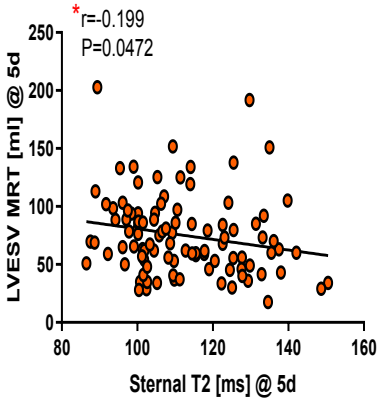
*r=-0.199
P=0.0472
LVESV MRT [ml] @ 5d
Sternal T2 [ms] @ 5d

k)

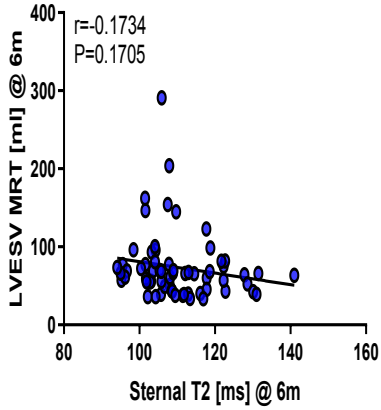
r=-0.1734
P=0.1705
LVESV MRT [ml] @ 6m
Sternal T2 [ms] @ 6m

l)

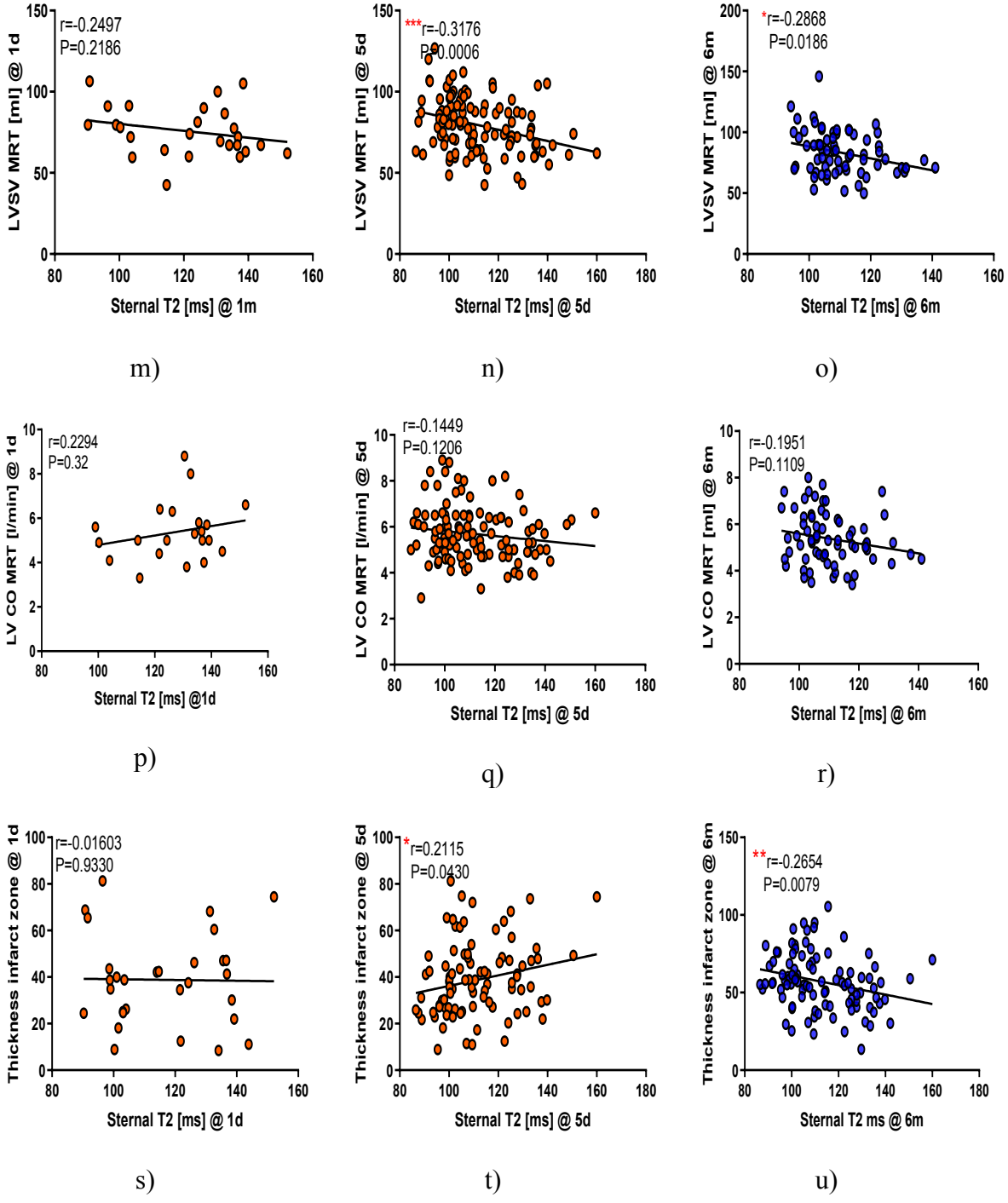

Fig. 25: Linear regression between indices of cardiac infarct size/function and sternal T2. The left column is a linear regression of sternal T2 and cardiac functions at day 1 post-STEMI, the middle column is linear regression for sternal T2 and cardiac functions at day 5 post-STEMI, and the last column is linear regression for sternal T2 and cardiac functions after 6 months follow-up. Analysed parameters were infarct size, left ventricular end-diastolic volume (LVED), left ventricular ejection fraction (LVEF), left ventricular end-systolic volume (LVESV). The evaluation was carried out using two-tailed Mann-Whitney test, significantly different ($P<0.05$), n=189 patients. The correlations were moderate to weak, with Spearman's rhos.

For the majority of the analyzed parameters and sternal T2, we observed no meaningful, consistent correlation, but when calculating Δ of left ventricular end-diastolic volume (ΔLVEDV) [6 months follow-up – day 5 after STEMI] as a measure for the degree of remodeling, there was a significant negative correlation with T2 1 day after STEMI (Figure 26a) but also with ΔT2[day 1 – day 5 after STEMI] (Figure 26b).

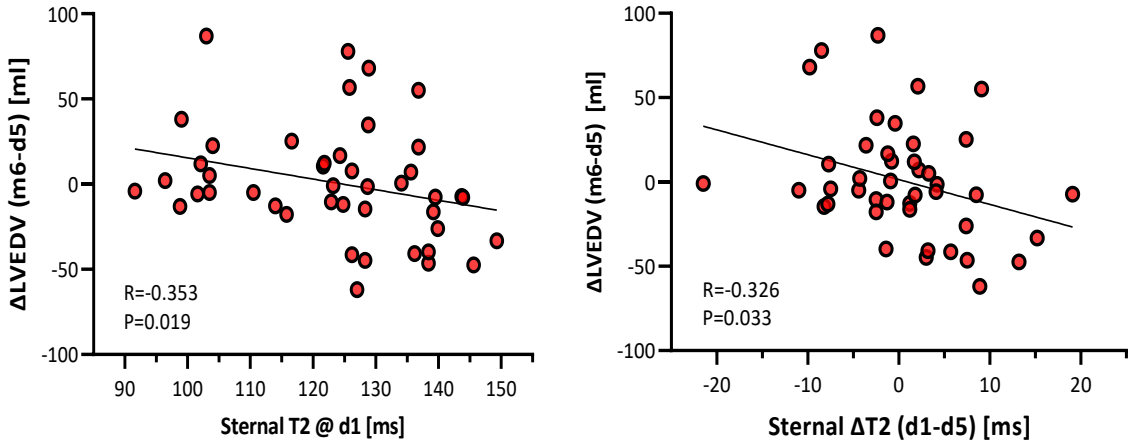

a) b)

Fig. 26: Linear regression of ΔLVEDV with sternal T2. a) linear regression of ΔLVEDV [6 months follow-up – day 1 post-STEMI] with human sternal T2 at day 1; **b**) (left) and linear regression of ΔLVEDV [6 months follow-up – day 1 post-STEMI] with ΔT2[day 5 – day 1 post-STEMI]. The evaluation was carried out using two-tailed Mann-Whitney test, significantly different ($P<0.05$), n=45.

This implies, the higher sternal T2 @d1 and the larger its drop/recovery from d1 to d5, the less the adverse remodeling. Specifically, this drop could be indicative for the temporal limitation of the inflammatory response preventing a detrimental overshoot.

3.1.7 Biomarkers and sternal T2 values

3.1.7.1 Inflammation markers of STEMI cohort

In our cohort of 193 STEMI patients, we also investigated the association between blood inflammation markers in the acute phase (1 day - 5 days of STEMI) and 6 months following STEMI. As expected, we found higher levels of cardiac inflammatory markers in the acute period with recovering values after 6 months of follow-up.

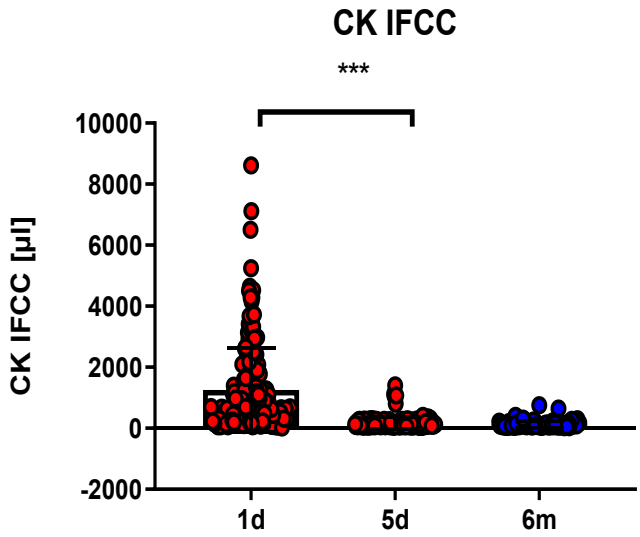
CK IFCC
***
CK IFCC [µl]
10000
8000
6000
4000
2000
0
-2000
1d
5d
6m

a)

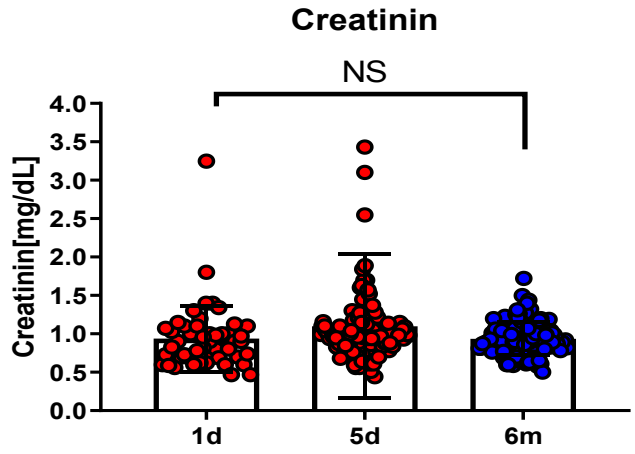
Creatinin
NS
Creatinin[mg/dL]
4.0
3.5
3.0
2.5
2.0
1.5
1.0
0.5
0.0
1d
5d
6m

b)

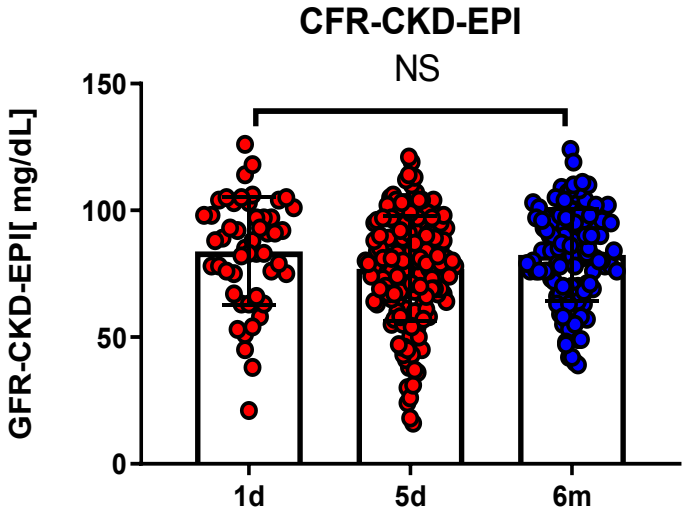
CFR-CKD-EPI
NS
GFR-CKD-EPI[mg/dL]
150
100
50
0
1d
5d
6m

c)

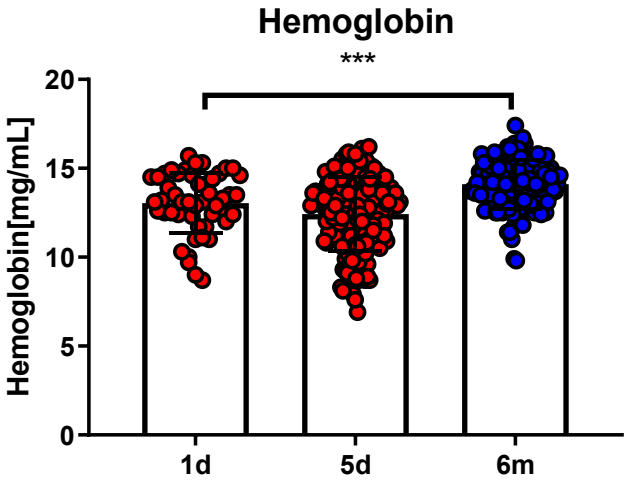
Hemoglobin
***
Hemoglobin[mg/mL]
20
15
10
5
0
1d
5d
6m

d)

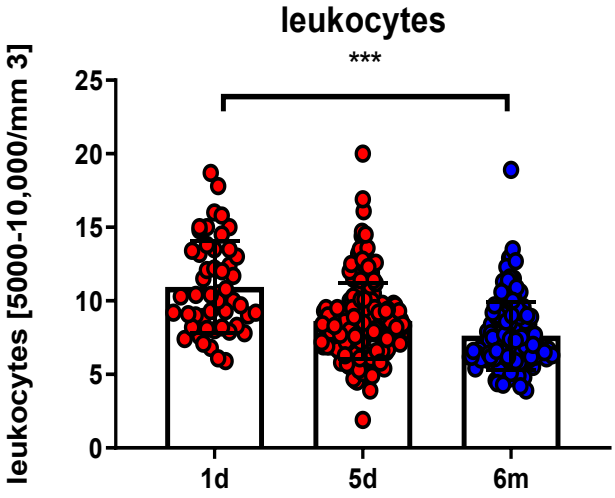
leukocytes
***
leukocytes [5000-10,000/mm 3]
25
20
15
10
5
0
1d
5d
6m

e)

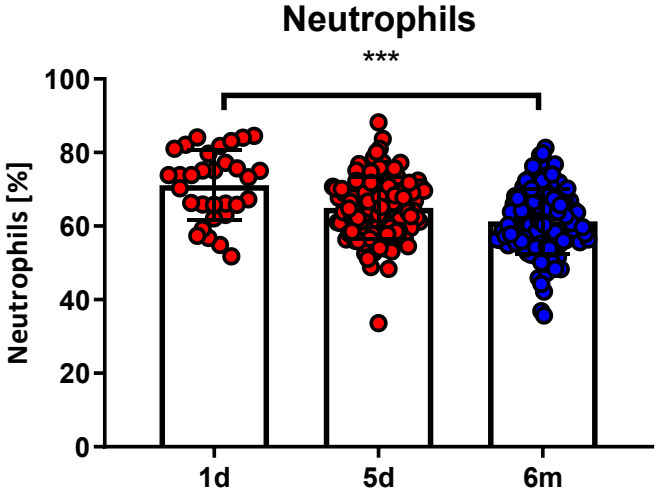
Neutrophils
***
Neutrophils [%]
100
80
60
40
20
0
1d
5d
6m

f)

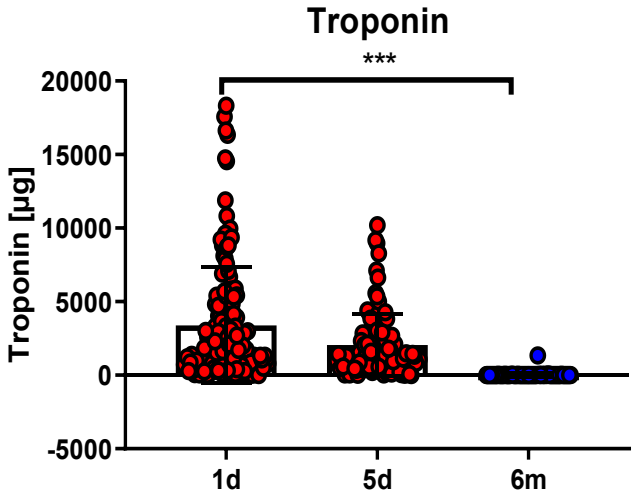

g)

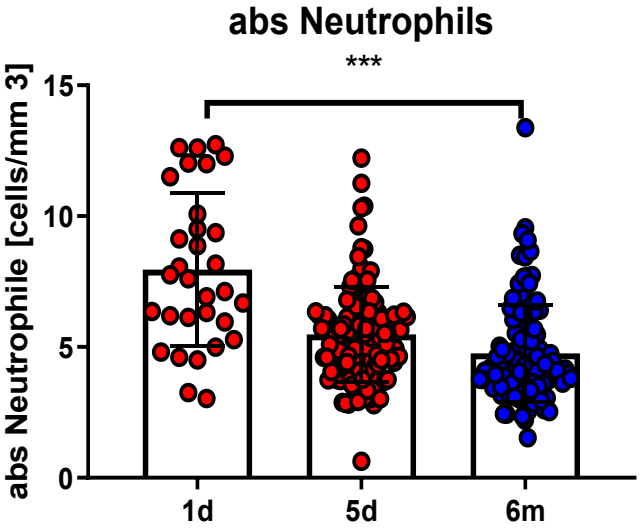

h)

Fig. 27: Time course of various biomarkers after STEMI. **a**) Creatine kinase (CK IFFC); **b**) Creatinin; **c)** Glomerular filtration rate (GFR-CKD-EP); **d**) Hemoglobin; **e**) Leukocytes; **f**) Neutrophils; **g**) Troponin; **i**) Absolute neutrophil numbers. The data are presented as mean and SD for STEMI patients at day 1, day 5, and 6 months follow-up. The evaluation was carried out using two-tailed Mann-Whitney test, significantly different ($P<0.05$), n=189 patients.

The results showed a consistent picture with elevated damage markers, such as creatine kinase and troponin (Figure 27a+g) as well as increased circulating immune cells (leukocytes and neutrophils, Figure 27e+h+f) at day 1 post-STEMI, which all significantly declined over timeThis finding might have been influenced by time as a confounder, as we did not strictly control the sampling time.

3.1.7.2 Association of biomarkers and sternal T2 values

In this section, we examined whether sternal T2 is associated with cardiac inflammation markers investigated in the previous chapter, but for the most widely studied biomarkers of inflammation CRP [139] and troponin [140], we observed no significant correlation with sternal T2. Furthermore, we examined the relationship between the circulating level of immune cells (neutrophils, leukocytes) measured in the acute phase and after 6 months of STEMI since alterations in sternal T2 could be directly related to the production of innate immune cells in the sternum.

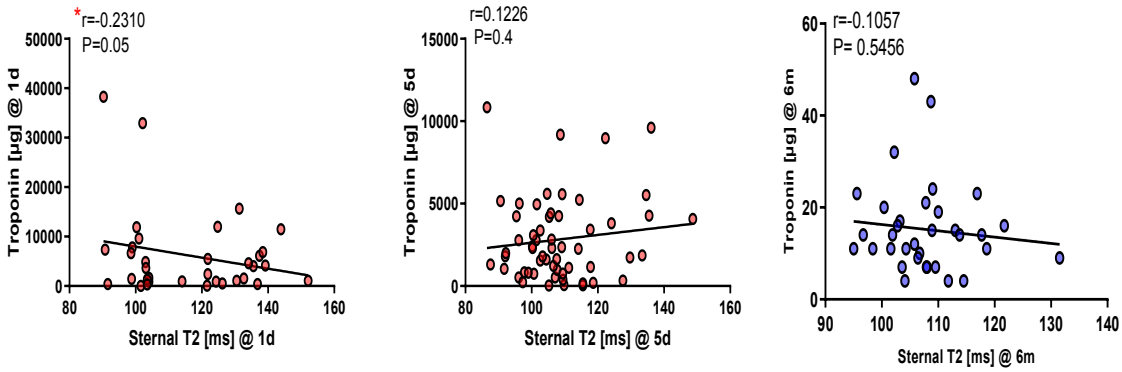

a)

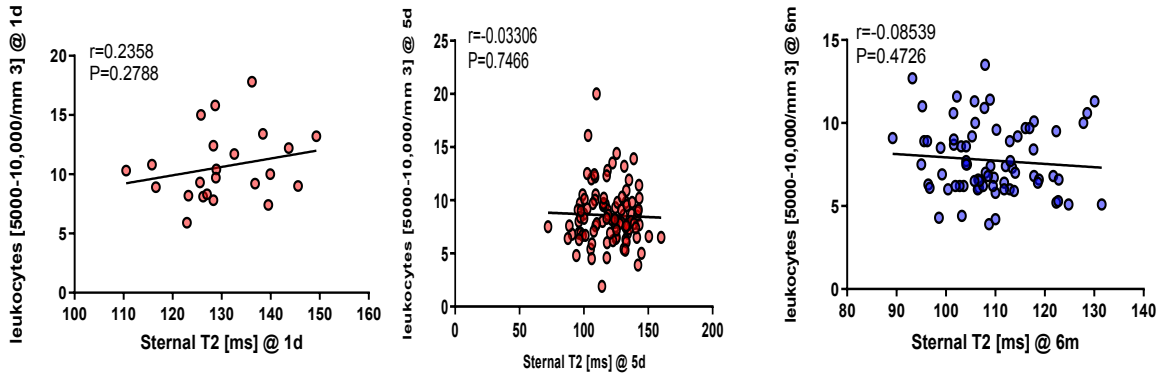

b)

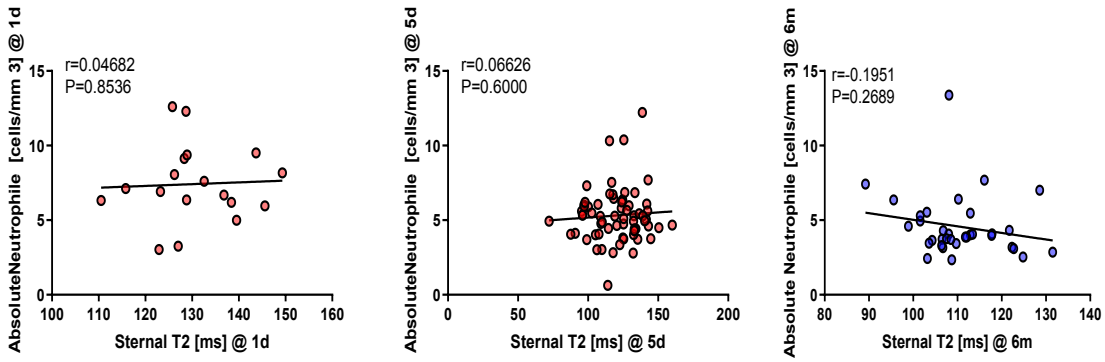

c)

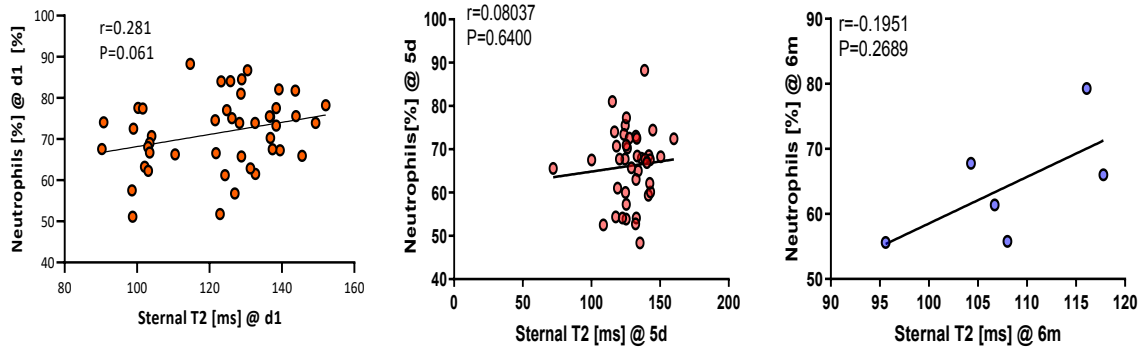

d)

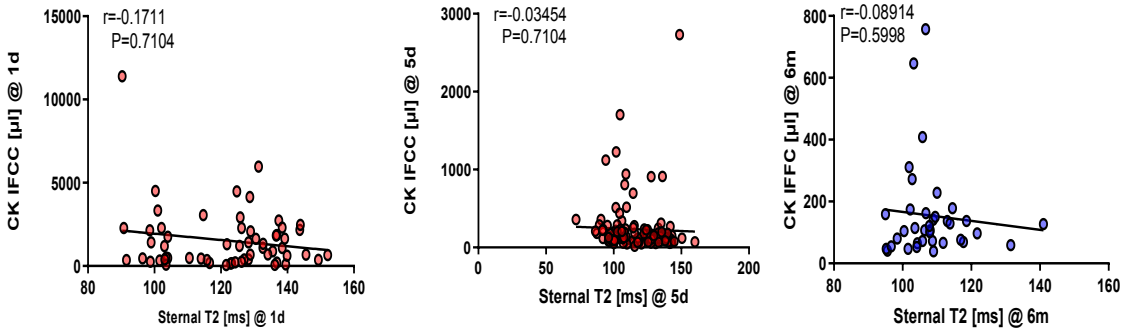

e)

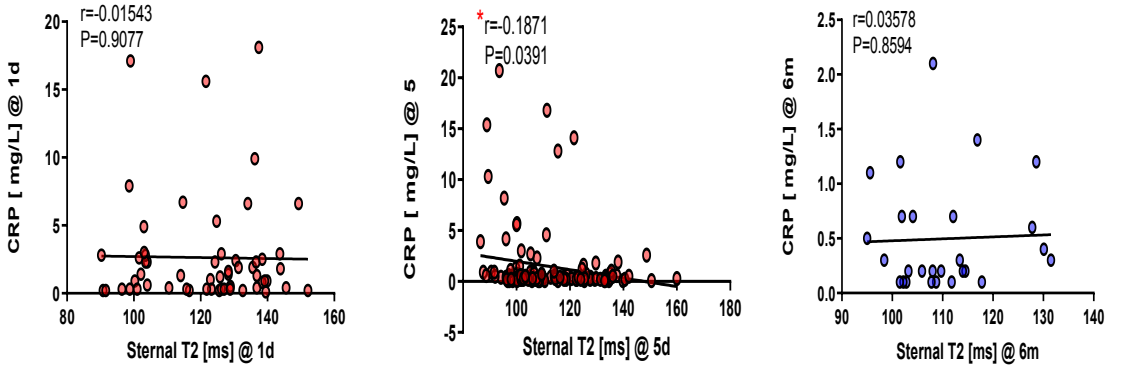

f)

Fig. 28: Linear regression plots of biomarkers and sternal T2. The left column is day one post-STEMI, the middle column represents day 5 post-STEMI and the last column shows 6 months follow-up between sternal T2 and the following measures: **a**) Troponin; **b**) leukocytes, **c**) absolute neutrophil, **d**) neutrophils [%]; **e**) creatine kinase (CK IFFC); **f**) creatinine; **g**) C reactive protein (CRP). Statistically, Spearman's correlation was used between inflammation markers and sternal T2 at acute STEMI (1d-5d) or after 6 months of follow-up events. These correlations were moderate to weak, with Spearman's rhos between ±0.3 and ±0.2 ($p < 0.05$).

The results showed that sternal T2 has a trend to a positive correlation (r=0.281, P=0.061) with the circulating neutrophil levels [%] (Figure 28d) at day 1 post-STEMI which suggests an association of enhanced neutrophil release with rising T2, thus reflecting the degree of emergency hematopoiesis. On the other hand, a trend to a negative correlation was found between sternal T2 and troponin (Figure 28a, r=0.2310, P=0.055) at day 1 post STEMI, which may indicate that troponin concentrations decreased in parallel with the increase in sternal T2 map. However, all other markers (e.g in Figure 28f+g) do not show a consistent correlation with sternal T2.

3.2. Mice

In addition to the human studies described above, a murine model of reperfused MI was longitudinally investigated by MRI at 6 time points, at baseline, and 1 to 22 days after MI. Also, ApoE mice fed a Western fat diet as a model of chronic cardiovascular inflammation were also investigated by MRI before and after the Western diet (WD). T1, T2, and fat/water fraction data were obtained at 9.4T to complement the human data with regard to the bone marrow system during MI. The murine MI experiments were carried out together with Hauke Dietz.

3.2.1 Cardiac function of MI mice model

As described in the section method, our laboratory has established a highly reproducible MI model, which is now used to investigate the alterations in bone marrow properties related to the induction of MI. In a first step, cardiac function was assessed before and after the insult,

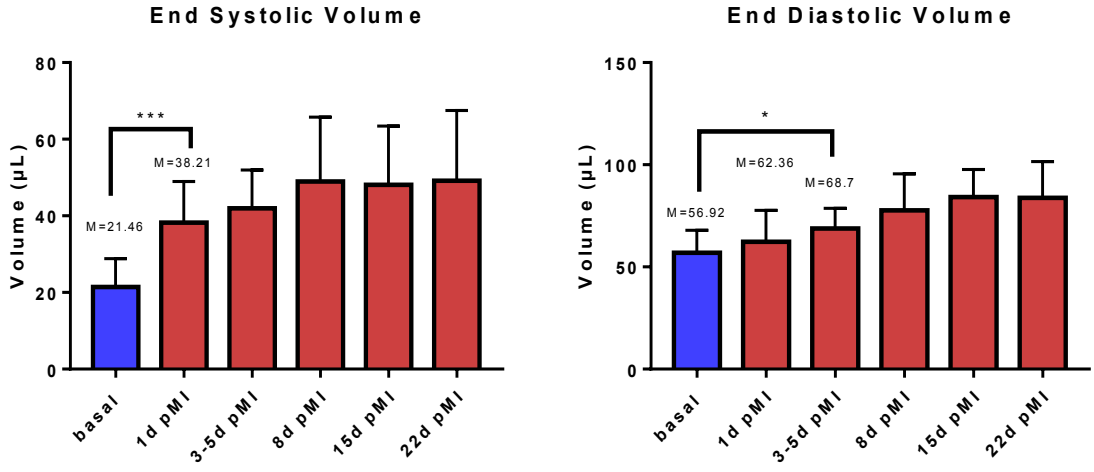

a) b)

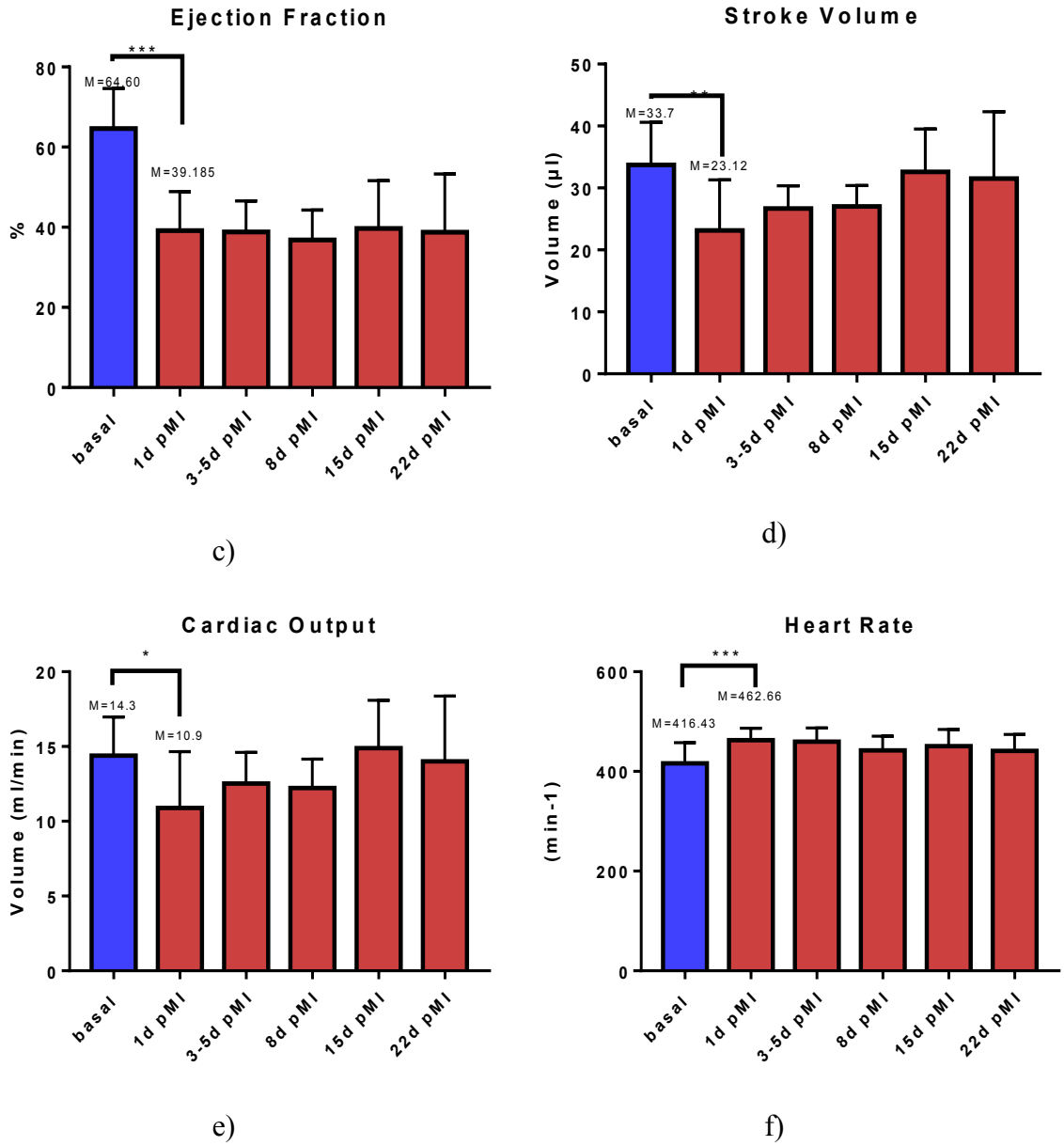

Fig. 29: MRI analyses of cardiac function at baseline and post-MI (1d-22d). Functional parameters which were calculated include end-systolic volume (**a**), end-diastolic volume (**b**), stroke volume (**c**), cardiac output (**d**), ejection fraction (**e**), and heart rate (**f**). Data are presented as mean ± SD. The evaluation was carried out using two-tailed Mann-Whitney test, significantly different ($P<0.05$), n=14 mice.

As expected, induction of MI resulted in a severe deterioration of murine cardiac function with increases in left ventricular end-systolic volume (Figure 29a, basal 21.1±8.32 µL, after 1 day of MI 38.1 ±5.8 µL) as well as end-diastolic volume (Figure 29b, basal 56.92±8.32 µL, after 1 day of MI 62.36 ±5.8 µL) and severely impaired ejection fraction (Figure 29c, basal 64.60±8.32%, 1 day after MI 39.185 ±5.8%) and cardiac output (Figure 29c, basal 14.3±8.32 µL, after 1 day of MI 10.9 ±5.8 µL).

3.2.2 Bone marrow T1 relaxation time

In parallel to cardiac function, also the response of the bone marrow to the induction of MI was verified in this model. In addition to the evaluation in patient data, here we extended the analysis beyond the sternum and included also the long bones femur and tibia to explore whether the marrow of the different bones might exhibit specific reactions to MI. The results show a slight increase in sternal T1 (Figure 30a) at day one post-MI compared to basal, which further raised until 22 days post-MI, but without reaching the level of significance.

The femur T1 reveals an increase 1d post-MI, and a decrease for the tibia compared to basal, as shown in Figure 30b+c. However, similar to the human data the results were characterized by high standard deviations requiring further optimization of the applied sequences to obtain more reliable results.

3.2.3 Bone marrow T2 relaxation time

Quantification of the acquired T2 maps shows that after induction of MI, the sternal T2 (Figure 31a) in mice reacted differently than the long bones (tibia and femur), illustrated in Figure 30b+c. While sternal T2 significantly increased 1 day after MI (Figure 31a, basal 25.5±2.8 ms, 1 d pMI 26.8±3.8 ms), both femoral and tibial T2 sharply declined at this time point as compared to baseline conditions (Figure 31b+c, femur: basal 23.4±2.8 ms, 1 d pMI 21.4±3.8 ms; tibia: basal 26.4±2.2 ms, 1 d pMI 24.1±3.6 ms). Furthermore, comparable to STEMI patients, T2 in the murine sternum was only transiently elevated after MI dropping back to control levels over time, whereas T2 in the long bones remained decreased over the entire observation period.

3.2.4 Bone marrow fat content

Next, we verified whether the activation of emergency hematopoiesis upon MI might be associated with alterations in bone marrow content due to energy consumption for immune cell production. To this end, the fat percentage of the bone marrow in sternum and femur was calculated, as shown in Figure 32a+b.

Interestingly, here a consistent response to the induction of MI could be observed: both sternal and femoral fat content dropped 1 day after MI in a similar manner although the decline in the sternum appeared to be less pronounced and showed a trend to recovery after 22 days post MI (Figure 33a: sternum, basal 21.1%, 1 d pMI 15.2%; b: femur, basal 22.5%, 1 d pMI 10.7%).

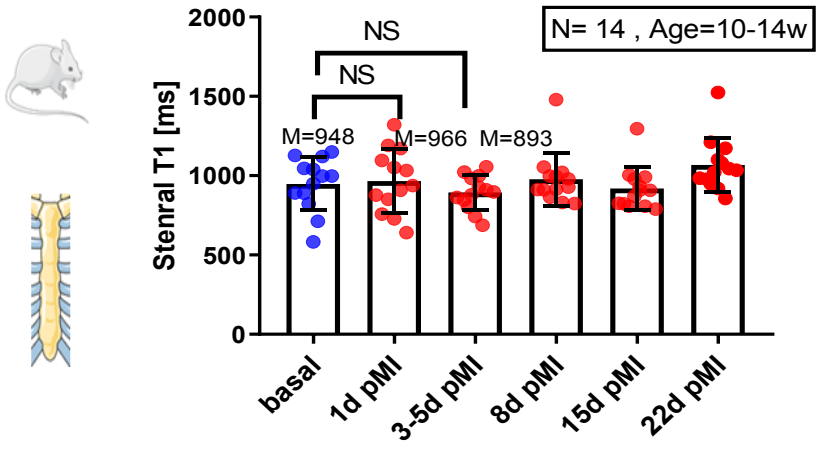

a)

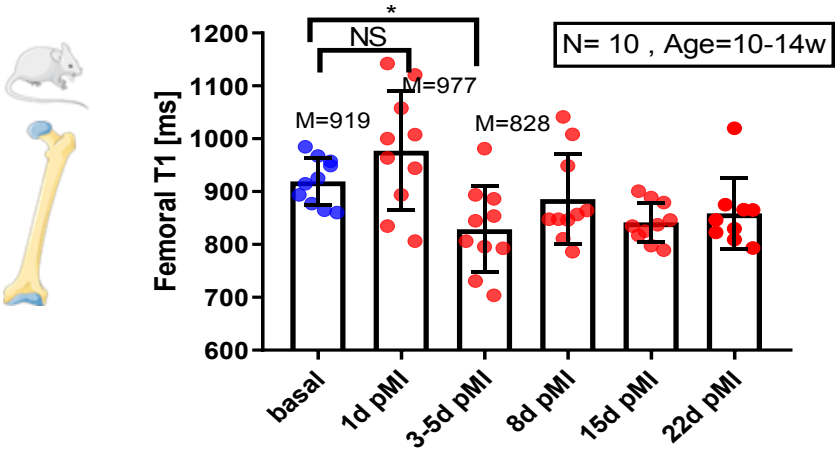

b)

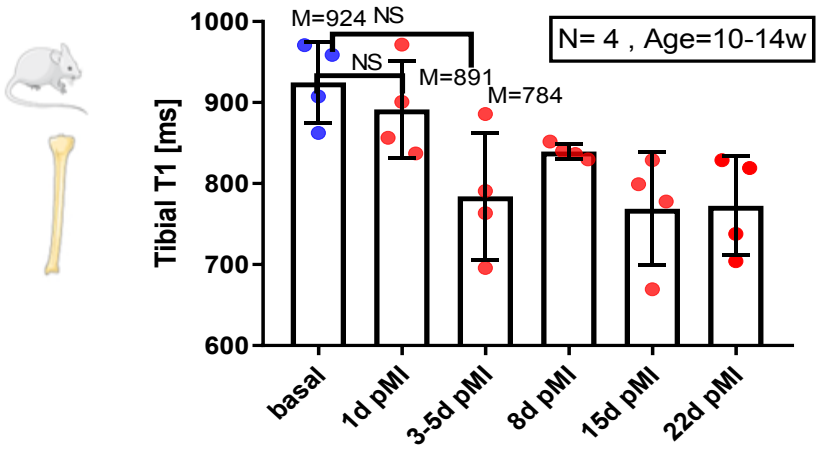

c)

Fig. 30: T1 of bone marrow 1d-22d post-MI. a) Sternal T1 before and at 1 day to 22 post-MI; **b**) Femoral T1 at 1 day to 22 post-MI; **c**) Tibial T1 at 1 day to 22 post-MI. Data are presented as mean ± SD. The evaluation was carried out using two-tailed Mann-Whitney test, significantly different ($P<0.05$), for sternum n=14, femur n=10, and tibia n=4.

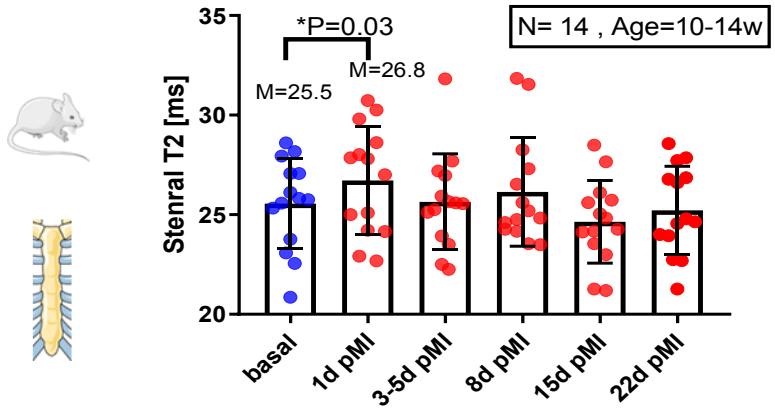

a)

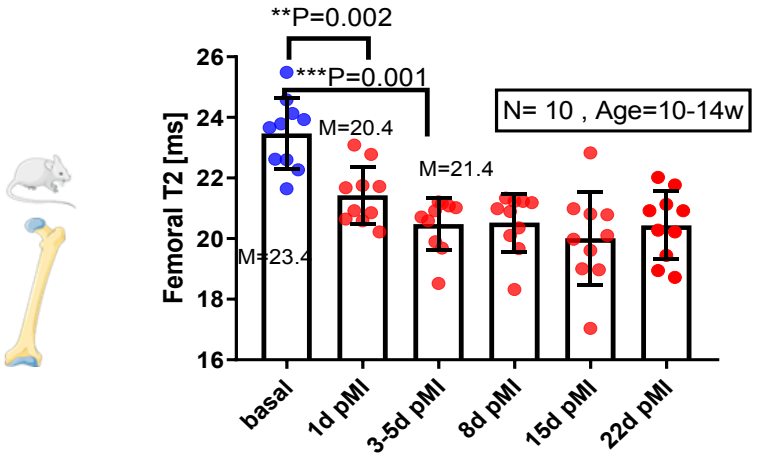

b)

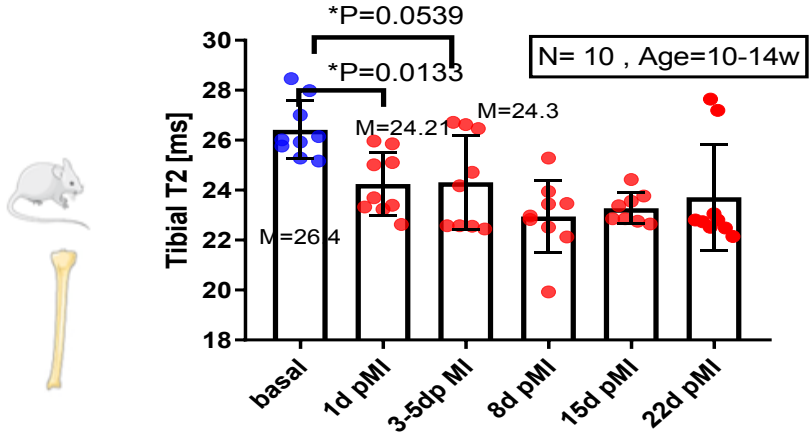

c)

Fig. 31: T2 of bone marrow 1d-22d post-MI. **a**) Sternal T2 before and at 1 day to 22 post-MI; **b**) Femoral T2 at 1 day to 22 post-MI; **c**) Tibial T2 at 1 day to 22 post-MI. Data are presented as mean ± SD. The evaluation was carried out using two-tailed Mann-Whitney test, significantly different ($P<0.05$) for sternum n=14, femur n=10, and tibia n=10.

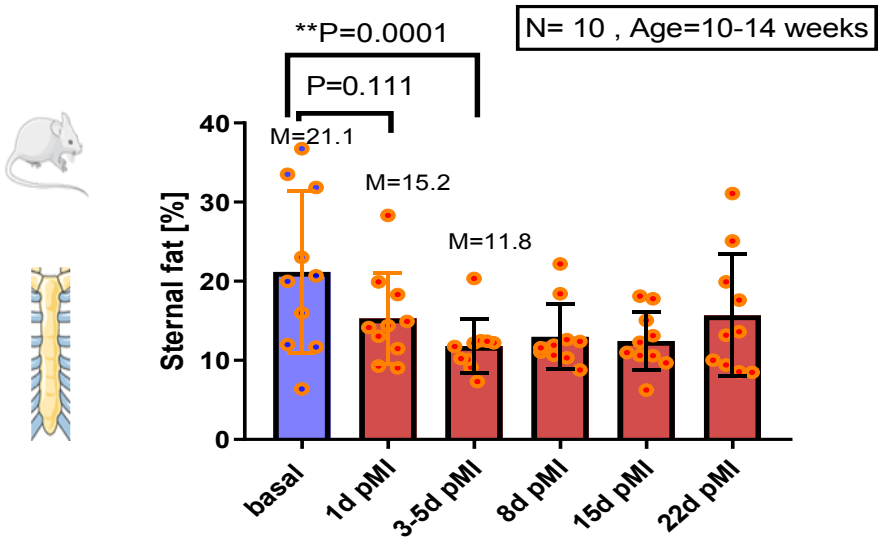

a)

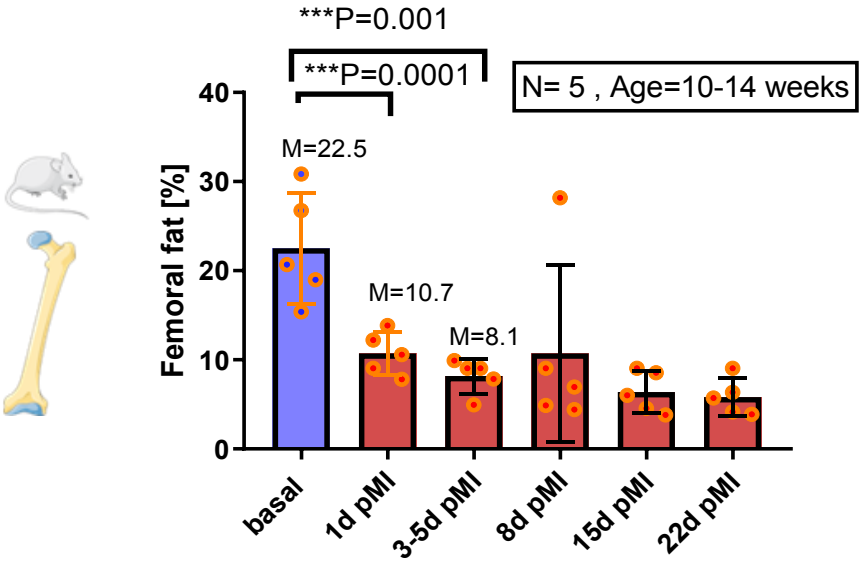

b)

Fig. 32: Fat content of the bone marrow 1d-22d post-MI. a) Sternal fat % at baseline and 1 day to 22 days post-MI; **b**) Femoral fat % at baseline and 1 day to 22 days post-MI. Data are presented as mean ± SD. The evaluation was carried out using two-tailed Mann-Whitney test, significantly different ($P<0.05$), for sternum n=10, and femur n=5.

3.2.5 Heart function and sternal T2

When investigating potential associations between cardiac function and sternal T2 values 1d post-MI, we found only lose, little meaningful correlations (Figure 33). While there were trends towards increased T2 with enhanced heart frequencies and decreased end-

diastolic volumes (EDV, Figure 33a+b), a significant negative correlation was only observed between end-systolic volume (ESV) and sternal T2 (Figure 33c).

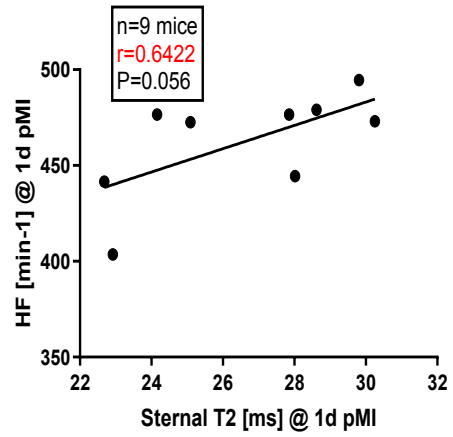

a)

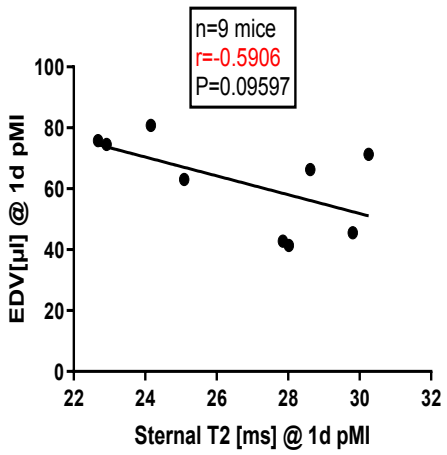

b)

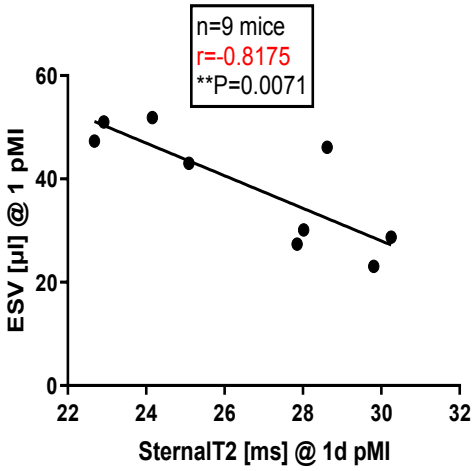

c)

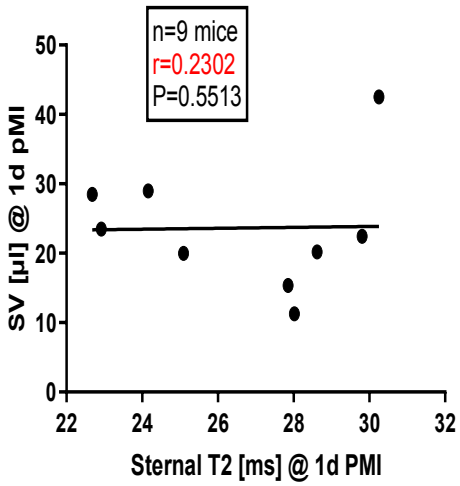

d)

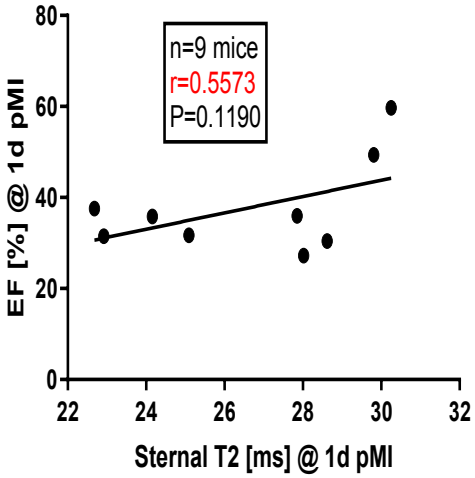

e)

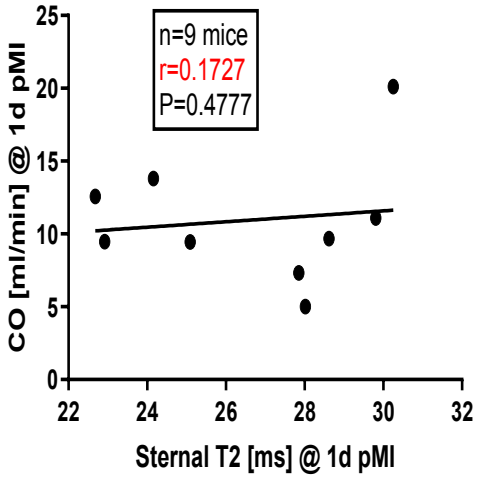

f)

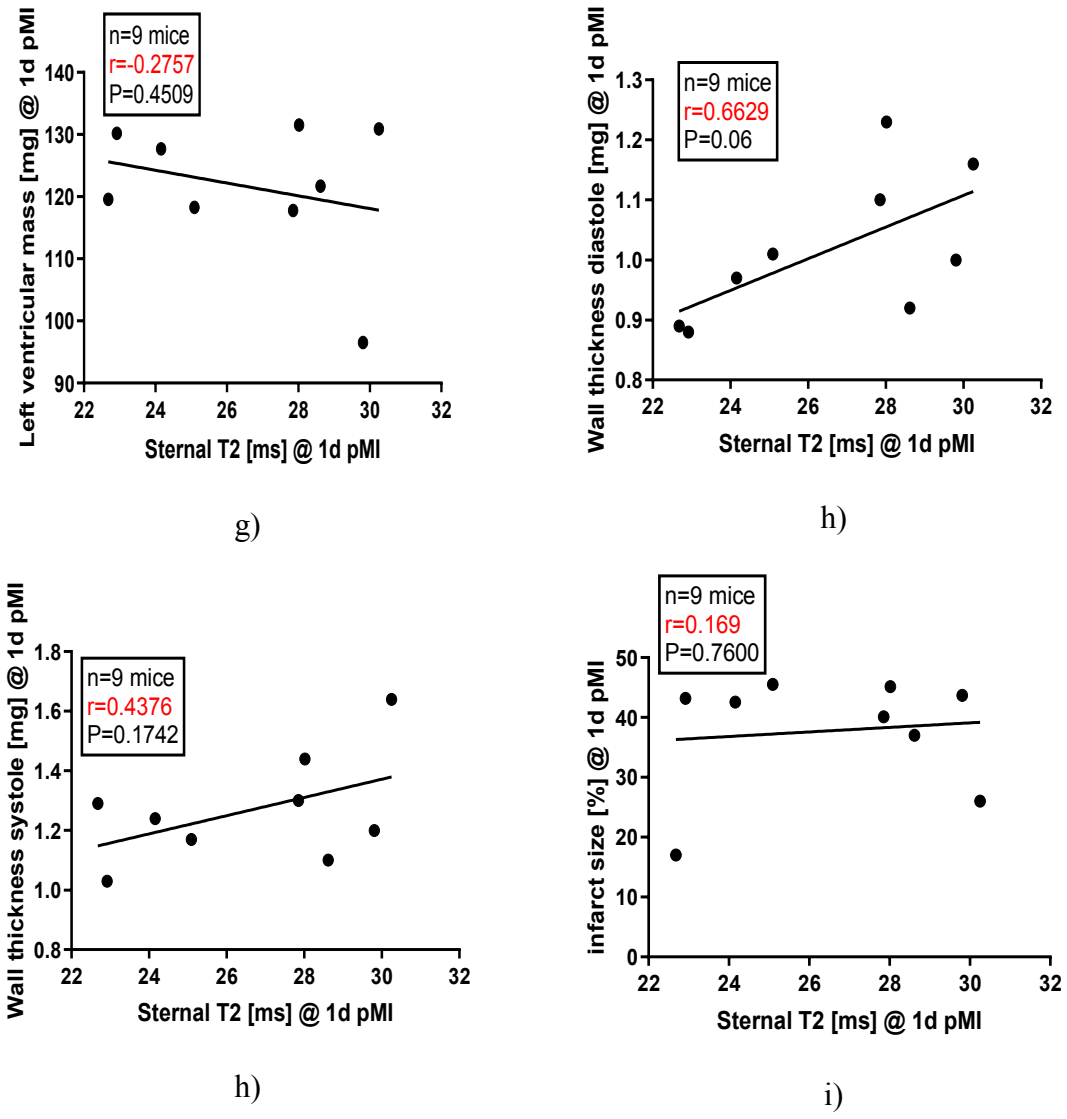

Fig. 33: Correlation plots of cardiac functions and sternal T2. Linear regression between sternal T2 at day 1 post-MI and **a**) heart failure (HF); **b**) end-diastolic volume (EDV); **c**) end-systolic volume (ESV); **d**) stroke volume (SV); **e**) ejection fraction (EF); **f**) Cardiac output (CO); **g**) left ventricular mass; **h**) wall thickness systole; **i**) infarct size (IS). These correlations were moderate to weak, with Spearman's rhos. The evaluation was carried out using two-tailed Mann-Whitney test, significantly different ($P<0.05$) for all n=9.

3.2.6 Correlation of bone marrow T2 and fat content

In order to explore the underlying cause of the altered T2 values in the bone marrow in response to MI, we verified its relation to the respective fat content. Here, we obtained for both sternum and femur T2 highly significant negative correlations (sternum: r=-0.804; P=0.005; femur: r=-0.9; P=0.0053) with their fat content at day 1 post-MI (Figure 34a+b). Of note, a similar association was also found in the human setting excluding increased fat levels as a reason for the increase in sternal T2 and suggesting for both bones an enhanced energy turnover with raised fat consumption during emergency hematopoiesis upon MI.

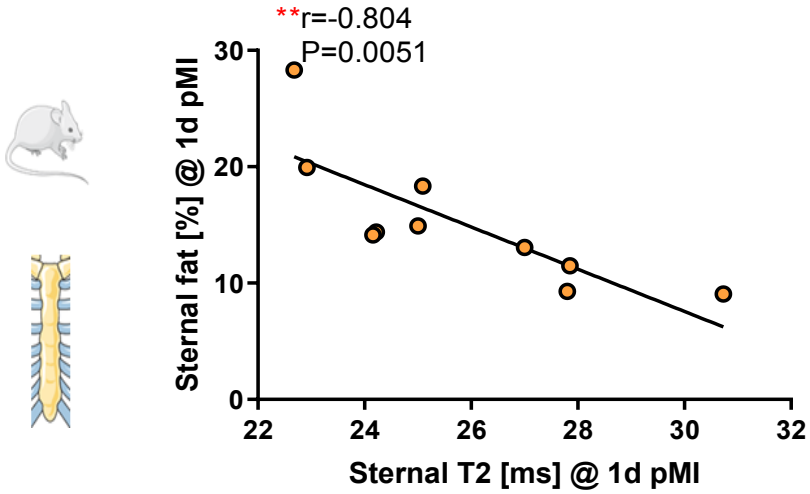

a)

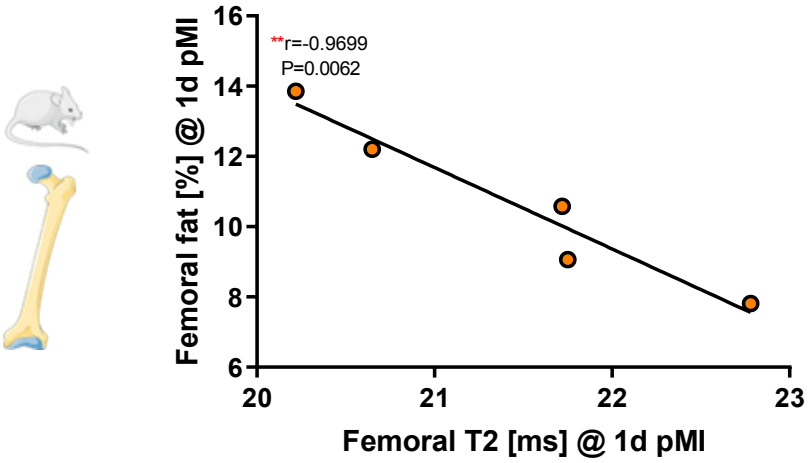

b)

Fig. 34: Correlation plots between T2 and fat of bone marrow. a) Linear regression of sternal T2 and fat contents at 1-day post-MI; **b**) Linear regression of femoral T2 and fat content at 1-day post-MI. These correlations were high to moderate with Spearman's rhos. The evaluation was carried out using two-tailed Mann-Whitney test, significantly different ($P<0.05$) for n=9 (sternum), and femur n=5 (femur).

3.2.5 Flow cytometric analysis of bone marrow

To explore if the differences in tissue properties as indicated by the distinct alterations of bone marrow T2 post MI is also reflected on the immunological level, we analysed neutrophil numbers in the sternum, femur, and tibia 3h and 1 day after infarction.

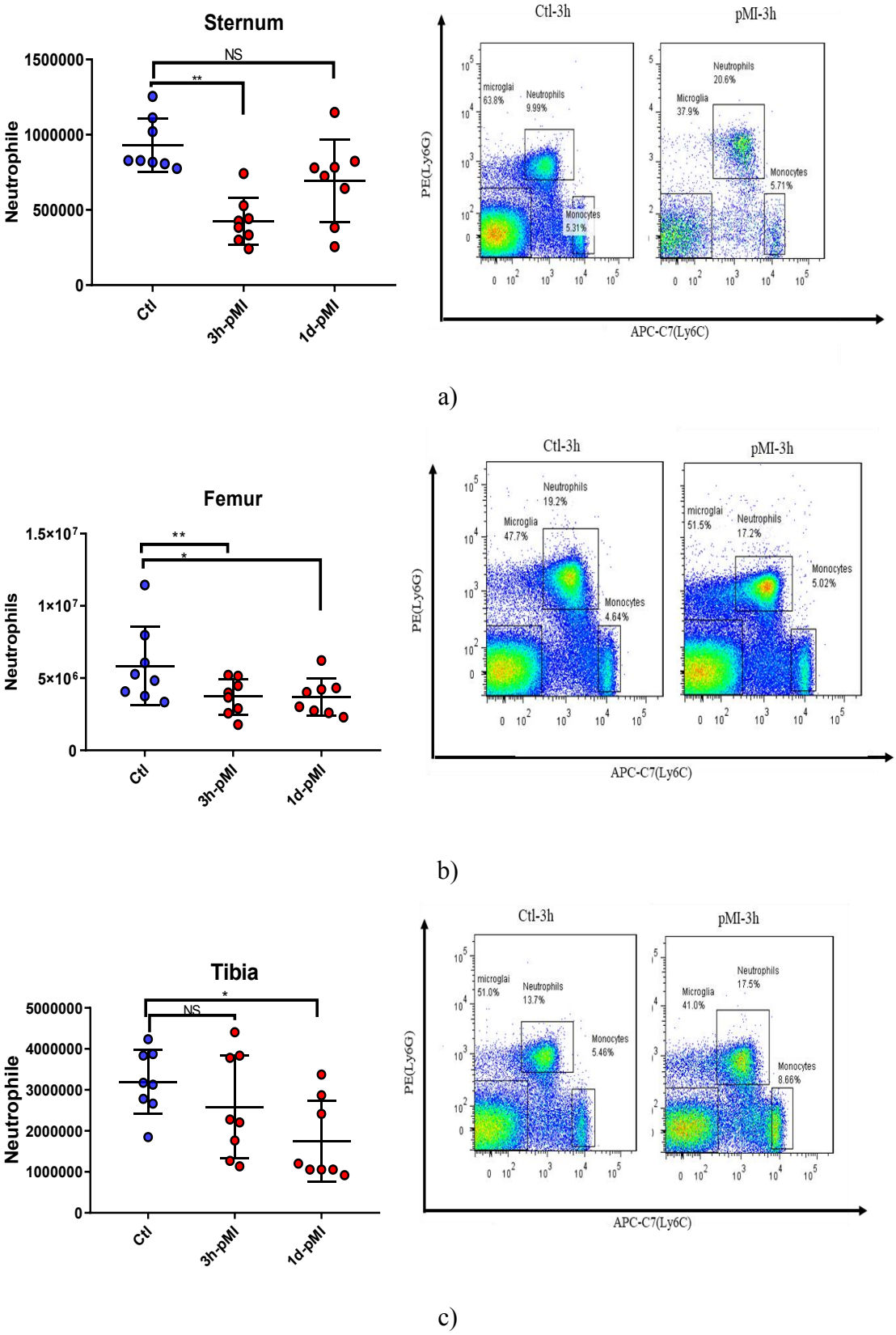

Fig. 35: Flow cytometry of the bone marrow after MI. Representative dot plots and calculated neutrophil numbers under baseline and 3 h to 1d after MI for **a**) sternum; **b**) femur; **c**) tibia., two-tailed Mann-Whitney test (control n=8, 3 h post-MI n=8, and 1 day after infarction n=8). Data are presented as mean ± SD.

The results of this experiment indeed revealed differential immune cell release patterns post-MI for the individual bones investigated: While the sternum showed an early sharp decline in neutrophil numbers and only a strongly mitigated response after 24 hours (Figure 35a), the femur exhibited a moderate but persisting drop in neutrophil levels over time (Figure 35b), whereas the tibia did not show significant neutrophil release until d1 after AMI (Figure. 35c).

3.2.6 Tracking of neutrophils using ^{19}F MRI

After confirming the release of neutrophils from the sternum after MI by flow cytometry, we next aimed to track the fate of sternum neutrophils also in vivo by ^{1}H/^{19}F MRI.

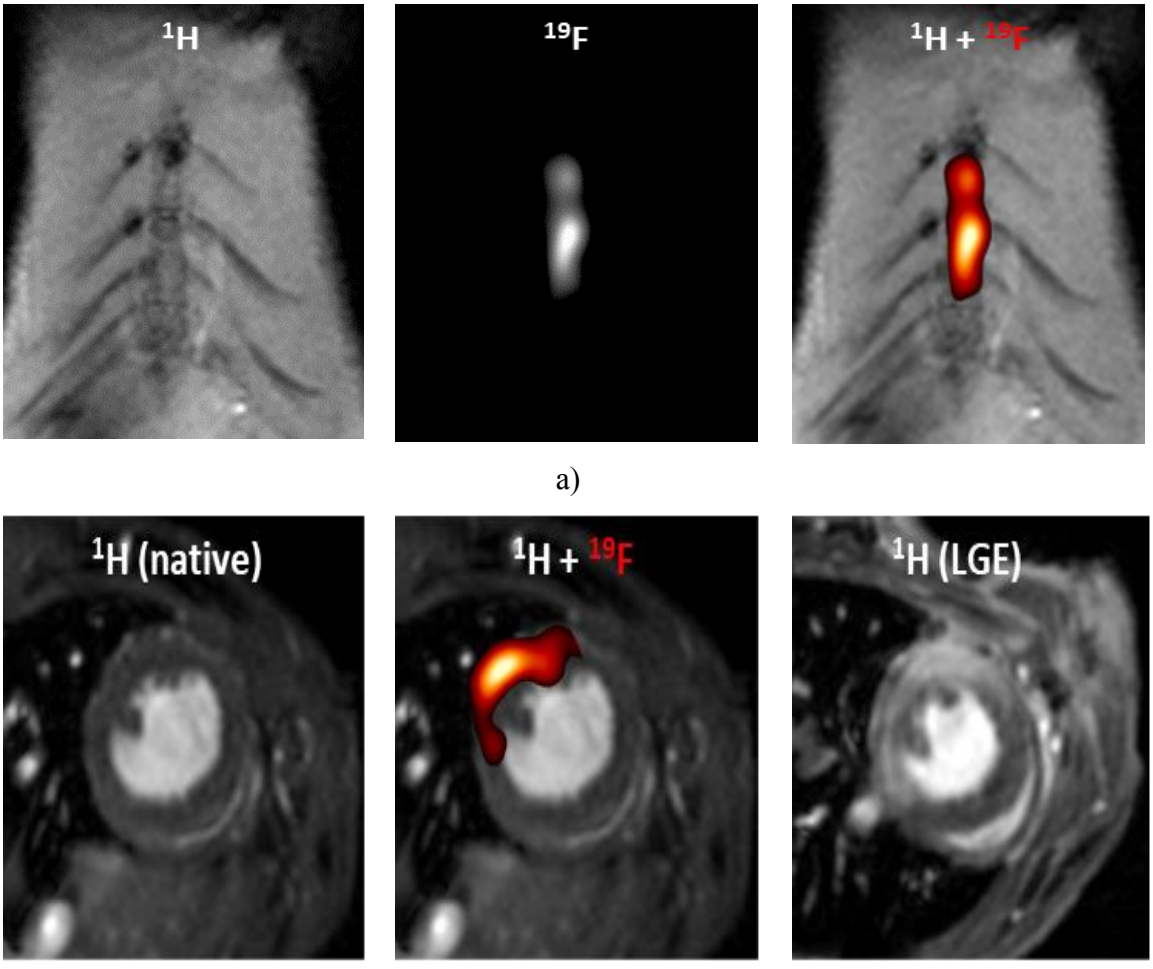

Fig. 36: Dynamic tracking of ^{mNP}PFCs prior to upon MI. a) Injection of 4 µl mNPPFCs in 3 segments of the sternum using a precision (Hamilton) syringe prior inflammation followed by in vivo visualization by combined 1H/19F MRI, resulting in a strong 19F uptake by sternum bone marrow neutrophils with 19F signals originating in the injected location; **b**) Heart in vivo visualization after 24 hrs following MI, indicating an egress of neutrophils from the sternum and appearance of mNPPFCs in the infarcted heart, as determined by combined 1H/19F MRI. Mice data n=3 mice (a,b).

To this end, 1 day prior induction of AMI ^{mNP}PFCs [141] (~2-4 µl) were injected directly into the sternum. Subsequent $^{1}H/^{19}F$ MRI confirmed the labeling of neutrophils in the middle sternal segments (Figure 36a) and follow-up 1 day after AMI unequivocally demonstrated the trafficking of ^{19}F-labeled neutrophils into the infarcted heart with matching patterns of LGE-positive myocardium (Figure 36b).

3.2.7 ApoE mice model for patients with SCADs

Given the striking results found in the MRI examination of humans, in that patients with stable coronary artery disease (SCAD) exhibited the highest sternal T2 values, we finally investigated ApoE mice exposed to a Western diet as a murine model for humans with SCAD. In the first set of experiments, cardiac parameters (Figure 37) were assessed revealing no major effects of the diet on cardiac morphology and function.

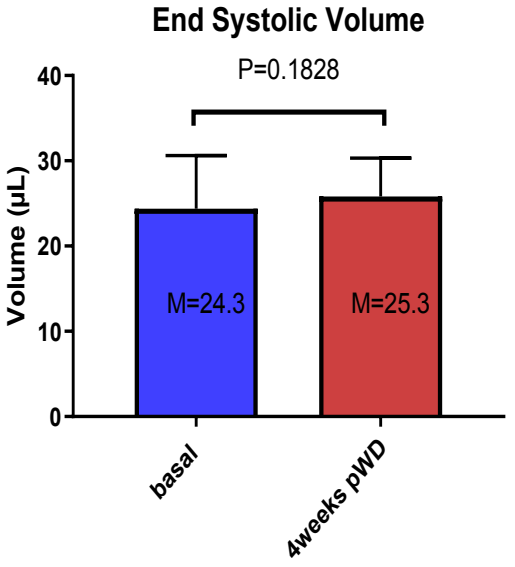

a)

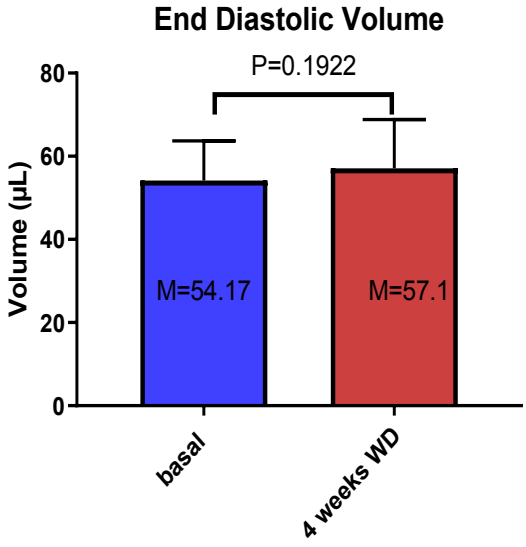

b)

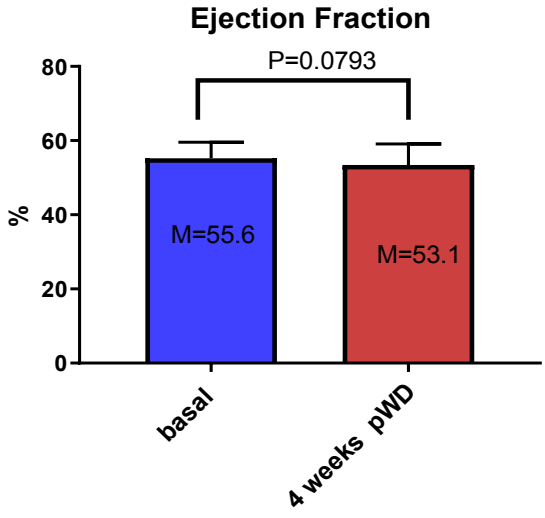

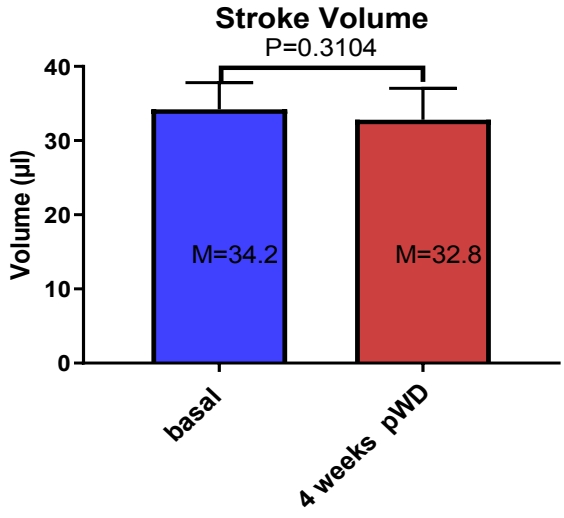

c) d)

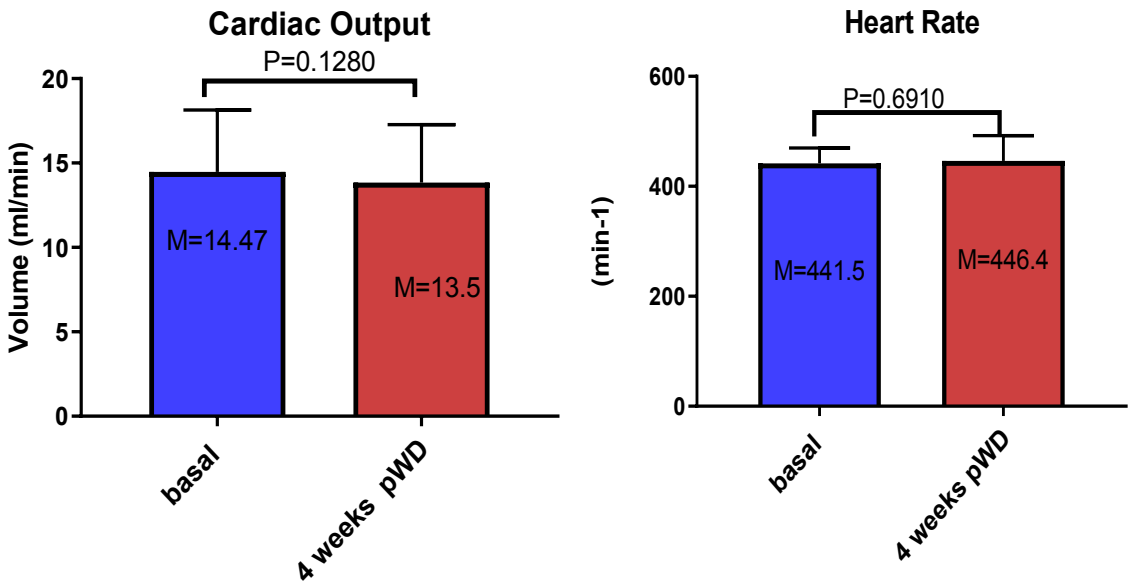

e) f)

Fig. 37: MRI analyses of the ApoE before and after WD. Functional parameters which were calculated include end-systolic volume (**a**), end-diastolic volume (**b**), stroke volume (**c**), cardiac output (**d**), ejection fraction (e), and heart rate (**f**). Data are presented as mean ± SD, n=11 mice. The evaluation was carried out using two-tailed Mann-Whitney test.

Secondly, T2 maps from sternum, femur, and tibia were acquired at baseline and 4 weeks after the Western diet. As a control, both C57BL/6J and ApoE mice fed a chow diet were employed to account for diet, genotype as well as aging effects.

Interestingly, the sternum of ApoE mice was already characterized under baseline conditions by slightly higher T2 values as compared to C57BL/6J mice which increased further during the diet (Figure 38a, before WD, T2= 32.5±2 ms, 4 weeks after WD 33.5±3.8 ms). Femoral T2 also tended to be higher in the transgenic group but here the diet did not cause a further raise (Figure 38b, femur basal 32.7±2 ms, 4 weeks pWD 32.4±6.2 ms).

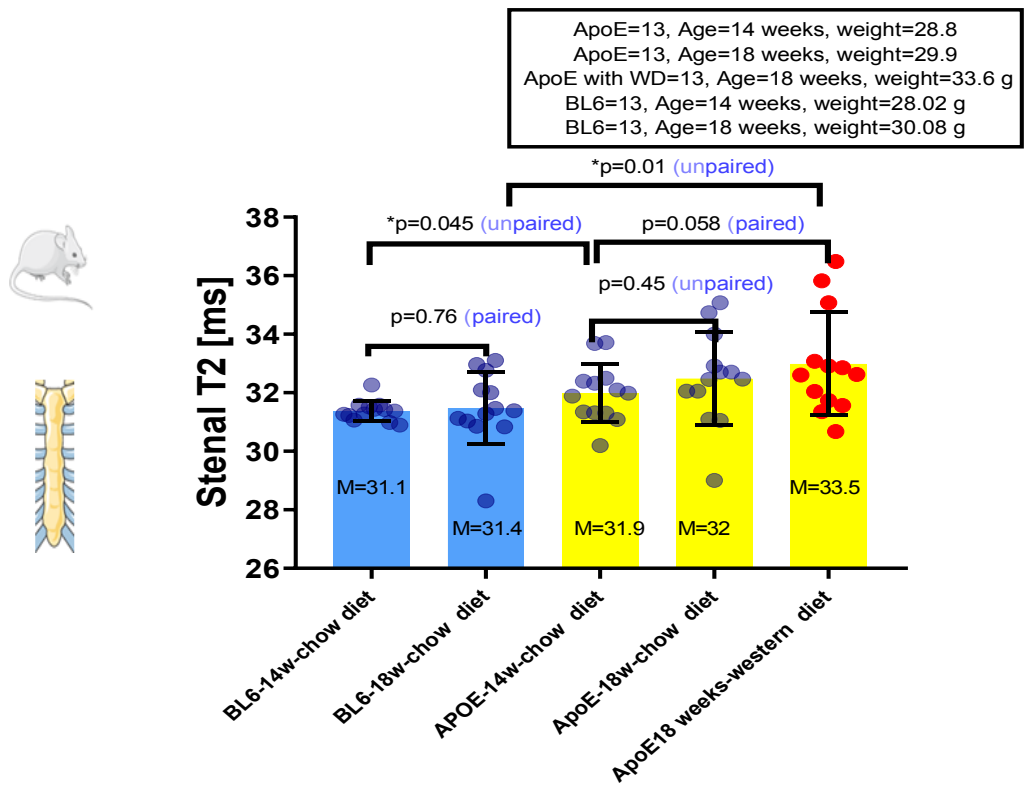
ApoE=13, Age=14 weeks, weight=28.8
ApoE=13, Age=18 weeks, weight=29.9
ApoE with WD=13, Age=18 weeks, weight=33.6 g
BL6=13, Age=14 weeks, weight=28.02 g
BL6=13, Age=18 weeks, weight=30.08 g
*p=0.01 (unpaired)
*p=0.045 (unpaired)
p=0.058 (paired)
p=0.45 (unpaired)
p=0.76 (paired)
Stenal T2 [ms]
38
36
34
32
30
28
26
M=31.1
M=31.4
M=31.9
M=32
M=33.5
BL6-14w-chow diet
BL6-18w-chow diet
APOE-14w-chow diet
ApoE-18w-chow diet
ApoE18 weeks-western diet

a)

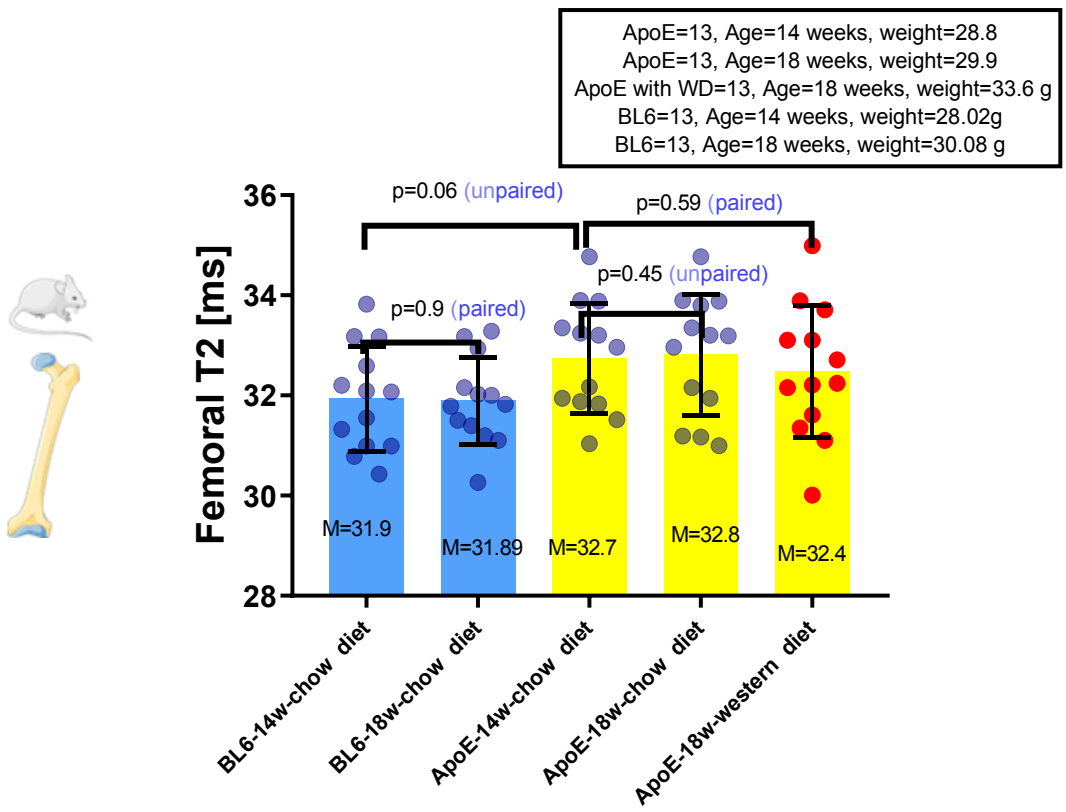
ApoE=13, Age=14 weeks, weight=28.8
ApoE=13, Age=18 weeks, weight=29.9
ApoE with WD=13, Age=18 weeks, weight=33.6 g
BL6=13, Age=14 weeks, weight=28.02g
BL6=13, Age=18 weeks, weight=30.08 g
p=0.06 (unpaired)
p=0.59 (paired)
p=0.45 (unpaired)
p=0.9 (paired)
Femoral T2 [ms]
36
34
32
30
28
M=31.9
M=31.89
M=32.7
M=32.8
M=32.4
BL6-14w-chow diet
BL6-18w-chow diet
ApoE-14w-chow diet
ApoE-18w-chow diet
ApoE-18w-western diet

b)

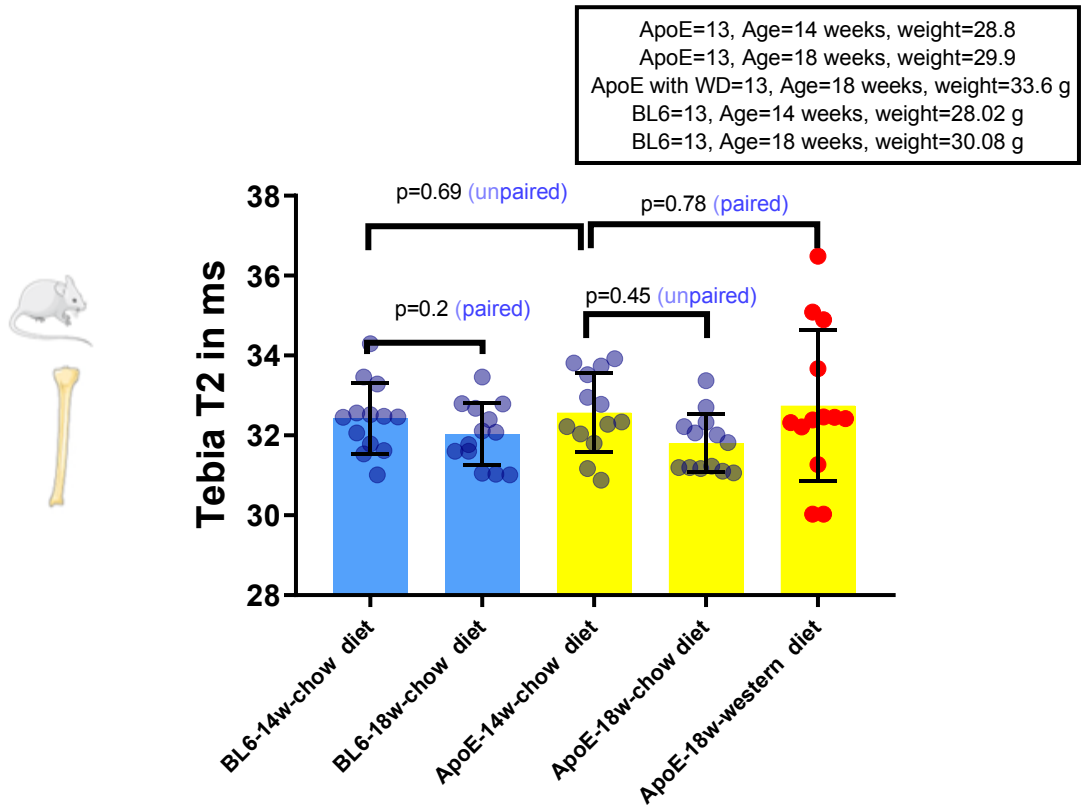

c)

Fig. 38: Sternal T2 of ApoE mice fed Western diet. a) Sternal T2 of ApoE before and after 4w of WD compared to wild type mice fed normal chow diet; **b**) Femoral T2 of ApoE before and after 4w of WD compared to wild type mice fed normal chow diet; **c**) Tibial T2 of ApoE before and after 4w of WD compared to wild type mice fed a normal chow diet. Data are presented as mean ± SD. The evaluation was carried out using two-tailed Mann-Whitney test, for n=13.

Finally, T2 of the tibia did not seem to be effected neither by genotype, diet nor age – at least over the observation period of the present study. Taken together, the results in ApoE mice reflected the findings in humans with SCAD with raising sternal T2 in dependence of the severity of the model used.

4. Discussion

4.1. Overview

As already pointed out in the introduction, the research findings to date regarding an association between the bone marrow system and myocardial infarction are based on limited clinical studies, mostly from retrospective studies and meta-analyses, in which the incidences of cardiovascular events in patients with MI were examined. In this limited framework, we first initiated different multiparametric MRI protocols to study the bone marrow system in parallel to functional cardiac analysis. With this, we characterized the properties of the bone marrow within the sternum in STEMI patients to identify potential surrogate parameters for the activation of the immune system and hematopoietic changes at MRI system level after AMI. In addition, animal experimental models of AMI were compared with data from clinical studies. Together, the results of the present work characterize for the first time noninvasively the bone marrow system after AMI and the stage of inflammation in humans and mice.

In summary, we found for both species a specific response in the sternum in that sternal T2 transiently increased after AMI while the long bones exhibited an opposite behaviour. This went along with a very early release of neutrophils from the sternum contributing to the transiently rised neutrophil levels in the blood post AMI. ^{19}F-labelling of neutrophils in the sternum prior MI revealed their direct trafficking into the infarcted myocardium. While we observed no correlation between sternal T2 with infarct size (IS), serum troponin levels, CRP or lymphocytes, we noticed a strong trend towards a positive correlation with circulating neutrophil numbers 1 day after STEMI. Determination of sternal fat post AMI showed in both humans and mice an inverse correlation with T2. Together, this suggests an association of enhanced substrate turnover and neutrophil release with rising T2, jointly reflecting the degree of emergency hematopoiesis. Taking the increase in left ventricular end-diastolic volume as a measure for the degree of remodeling, we found a significant negative correlation with sternal T2 at d1 as well as with ΔT2 (d1–d5 after STEMI) implying, the higher sternal T2 at d1 and the larger its drop/recovery from d1 to d5, the less the adverse remodeling. Specifically, this drop could be indicative for the temporal limitation of the inflammatory response preventing a detrimental overshoot. Overall, our results suggest a strong early activation of sternal emergency hematopoiesis for quick

removal of debris and its subsequent rapid de-activation as beneficial for the remodelling of the human heart after STEMI. In conclusion, we provided first evidence for a heart-sternum axis after AMI by demonstrating the egress of neutrophils from the sternum into the acutely infarcted myocardium and revealed that intensity and timing of sternal emergency hematopoiesis are crucial for the healing process. Visualization of this systemic signal could help develop new levels of precision medicine for immunomodulatory therapy for AMI.

4.2. T2 relaxometry and fat content of bone marrow

We here applied T2 mapping for a comprehensive characterization of the bone marrow upon myocardial infarction in human and mice. The proximity of the sternum to the heart enabled us to investigate the tissue properties of the sternal bone marrow in the Düsseldorf STEMI cohort by analysis of cardiac short-axis T2 maps covering the sternum (Figure 5). In this prospective study [142], a significant increase in sternal T2 on the day after STEMI was observed, which decreased again after 5 days and continued to approach baseline values of age-matched healthy controls during a follow-up period of 6 months (Figure 18). Experimental induction of reperfused AMI in male C57Bl/6J mice and longitudinal monitoring resulted in similar findings in the murine setting with a transient increase of sternal T2 at day one after AMI (Figure 30a). Importantly, this rise in T2 was specific for the sternal bone marrow, since parallel measurements of the tibia demonstrated an opposite behavior (Figure 30c). The distinct behavior of T2 in sternum and tibia indicates a different bone marrow microenvironment in the both bones, which one is in proximity to the inflammation site (sternum), and other is far (tibia). When inflammation occurred in the heart, the bone marrow had a high propensity to recruit immune cells from all bone marrow parts generally and from the nearest tissue at an early stage specifically [80]. Thus, the increase in sternal T2 most likely reflects the early activation of hematopoiesis to supply the demand of heart during AMI.

To analyse the fat content of the bone marrow, the mDixon package was used in the STEMI cohort and the proton density fat fraction (PDFF) in AMI mouse model. Activation of the bone marrow for the formation and release of immune cells into the circulation is assumed to be associated with substantial metabolic turnover. This will result in an enhanced consumption of fat to match the increased energy demand which in turn will rise perfusion for substrate supply and this will alter the tissue properties in a way that is prone for readout by MR. These changes will impact the homogeneity of the local magnetic field and thereby

tissue relaxation times, which is the cause for the alterations described in the previous chapter. Furthermore, substrate consumption can alter the tissue fat content. The results in humans (Figure 21, n=24) indeed revealed a lower fat content in the sternum at d1 after STEMI compared to 6 months follow-up. Experimental MI in mice essentially led to the same findings with a drop in sternal fat upon MI and a return to baseline values in the course of the observation period (Figure 32a, n=10). Of note, linear regression of the patient data demonstrated a highly significant inverse correlation of sternal fat and T2 (Figure 22c), excluding an enhanced fat content as underlying cause for the transient increase T2 upon AMI. Rather, this indicates an enhanced substrate turnover in the sternal bone marrow required for the increased immune cell production and release upon AMI. The alterations in tissue texture resulting in the T2 increase during activation of sternal emergency hematopoiesis are most likely due to an increase of the water fraction as has been observed in lumbar hematopoietic bone marrow [143].

An interesting additional finding of this study is that patients with stable coronary artery disease (SCAD) exhibited the highest sternal T2 values (Figure 19) of all groups investigated. The same was true for ApoE mice, which already under basal conditions exhibited rised sternal T2 values (Figure 38a)as compared to age and weight-matched C56BL/6J mice. This effect was even enhanced when ApoE mice were subjected to a high-fat diet, which was intended to serve as a mouse model for accelerated atherosclerosis [144]. Again, these observations were specific for the sternum, since the data for the long bones were less consistent as shown in Figure 38b+c . Femoral T2 also tended to be higher in ApoE mice but here the diet did not cause a further raise, while T2 of the tibia did not appear to be dependent on either genotype or diet. Taken together, it might be assumed that the chronic low-grade inflammation present in SCAD patients and as well in ApoE mice (which is exacerbated by high-fat diets) leads to a constantly increased hematopoiesis which is reflected by raised T2 levels in the sternum in both species.

4.3. Sternal emergency hematopoiesis after AMI

The extensive ischemic injury during AMI triggers a massive immune response and a rapid release of neutrophils migrating to the injured tissue. However, persisting inflammation and elevated circulating neutrophils have been associated with poor outcomes after AMI, yet all studies of immunomodulatory therapy in AMI have yielded neutral results so far [145]. This is most likely due to the lack of knowledge about the quality of activated emergency hematopoiesis and how this systemic signal influences the course of AMI, raising the need for depiction of the immune response not only in blood samples but also

at its site of origin and target tissue. For emergency hematopoiesis, the marrow of the long bones is expected to play a major role, but the sternum is haematopoietically active as well, retains its activity into old age [146] and is anatomically located in close vicinity to the heart (Figure 5).

In this context, our worked focused on early events (3h to d1 post AMI) and neutrophils as cell population considered to be first responder to the injured heart. Also generally in the setting of inflammation, neutrophils contribute to the first line of defense and early reach the inflammatory foci [147]. In the heart, particularly after MI, neutrophils contribute to removal of the necrotic tissue [78], but also to the initiation of the healing process [148]. However, there is little knowledge about the contribution of individual bone marrow segments to the neutrophil release under steady state or after myocardial infarction. The results of the present study unequivocally show a differential behavior of the distinct hematopoietic niches both on the tissue texture level (sternal T2 vs. tibia T2) as well as in their neutrophil content as determined by flow cytometric analyses: Whereas the tibia did not show significant neutrophil release until d1 after AMI, the corresponding response of the sternum was detectable as early as 3 hours after AMI (Figure 35a+c). These data show that after infarction, the different bone marrow segments are characterized by their own signatures for the release of immune cells into the bloodstream. The close proximity of the sternum to the injured heart might furthermore encourage the hypothesis that immune cells may infiltrate the injured site by a direct route (as observed in the brain after stroke [76]) rather than via the circulation. In this context, it would be valuable to explore the quantitative contribution of the sternal neutrophils to the overall immune response and also whether sternal and tibial neutrophils are differentially responsive to distinct cytokines released after MI, which might explain the time-shifted immune cell release from sternum and long bones.

To corroborate that the early drop of neutrophil numbers in the sternum was indeed caused by trafficking of sternal neutrophils into the infarcted heart, we used a direct labeling approach lately published by our group [149]. Compared to other imaging modalities utilized for visualization of neutrophils [150 ,151], this method allows a non-invasive and longitudinal tracking of neutrophils using background-free ^{19}F MRI in combination with perfluorocarbons specifically targeting murine neutrophils (^{mNP}PFCs). In the present setting, ^{mNP}PFCs we injected directly into the sternum of mice followed by ^{19}F MRI confirming the presence of a specific ^{19}F accumulation in the sternum (Figure 36a). Subsequent induction of AMI, led to the appearance of ^{19}F signals in the infarcted heart

showing excellent colocalization with LGE patterns of ischemic myocardium (Figure 36b). These results unequivocally demonstrate that sternal neutrophils contribute to the first wave of immune cell infiltration after AMI. However, on the base of these findings it cannot be decided whether this contribution is mediated via the bloodstream or other (direct) routes. For this, additional experiments with dedicated light sheet microscopy techniques are required, which are currently under planning with external cooperation partners.

4.4. Heart remodeling after AMI

In terms of clinical decision making, an important finding of the present work is the correlation of sternal T2 values in the early phase post STEMI with the outcome after 6 months of follow-up. In contrast to experimental AMI in mice, baseline values are usually not available in humans, which makes a comparison of absolute measurements obtained after follow-up more or less useless because individual baselines before STEMI might be very different. To overcome this issue. we took the increase in left ventricular end-diastolic volume (ΔLVEDV; 6 months follow-up – d5 after STEMI) as a measure for the individual degree of remodeling, and found significant negative correlations with T2 as well as ΔT2 (d1–d5 after STEMI; Figure 26a+b). These results can be interpreted as follows: the stronger the initial hematopoietic response (reflected in high sternal T2 at day 1 post STEMI) and the sharper its decline within the next days (mirrored in a large T2 drop from d1 to d5), the less the adverse remodelling. Thus, for the clinician, the degree of this drop could be indicative for an ongoing or already attenuated inflammation and guide an adequate therapeutic intervention to prevent a detrimental overshoot of the immune response. Thus, an early MRI re-investigation of STEMI patients after the insult including T2 mapping and mDixon of the sternum could help to assess the current inflammatory state for individualized precision medicine.

4.5. Limitations

The present work represents the first MRI approach to investigate non-invasively the tissue properties of distinct bone marrow compartments in mice and humans after AMI. For this, data from clinical studies and experimental mice models were evaluated. In this thesis, we had limited sources (such as time, coronavirus restrictions) which made it difficult to carry out some analyses with greater depth. We were constrained by time, so that data from STEMI patients were analysed which were originally not recruited to fit to the design of

the present study. This resulted in the certain limitation that the sternum was only analysed in short axis slices acquired for functional analyses and that no other bone marrow segments could be evaluated. From a prospective point-of-view, it would be desirable to include more scanning protocols with specific orientation to the sternum as well as the long bones and an extensive patients' recruitment with larger cohorts. As stated in our results, there is a correlation between elevation of sternal T2 relaxation time and neutrophils, but no association with other biomarkers. This may be related to the heterogenous patient collective which may by compromised also by other cardiovascular events, so that alterations in some inflammation markers may not only be driven by the acute MI. Here, it would be beneficial for future analyses to control all potential factors influencing the markers and to classify the patients accordingly.

For the murine studies, also some limitations have to be taken into account. It is generally known that findings from animal research can only be transferred to the complex pathophysiological processes in humans with reservations. First of all, there is a fundamental difference in the pathophysiological origin of the infarction. While myocardial ischemia in humans is often based on inflammation of an atherosclerotic plaque with subsequent plaque rupture and thrombotic vascular occlusion, this central inflammatory component is missing in the mice model used in this study. Another aspect that has to mentioned is the fact that MI mostly affects elderly people, whereas the animal experimental results are obtained from young mice [152]. Accordingly, the initial situation with regard to underlying inflammatory processes before the onset of MI is very different in mice and humans and can therefore also differentially shape the healing process thereafter. In addition, it must be considered that there are species-specific differences in inflammation and cellular response in the context of bone marrow characterization. These considerations emphasize that the results of the mouse model can only be transferred to humans to a limited extent.

The large focus of this thesis was on alterations of sternal T2 relaxation time as consequence of AMI. However, as mentioned above, putative comorbidities may have also impact on the individual inflammatory and thereby on sternal tissue properties as well as its T2. Although we carried out some control animal experiments with ApoE mice (plus/minus Western diet) to account for this, we did not explore in detail the hematopoietic response in the sternum by histology, which indeed warrants further investigation in the future. Furthermore, an association between cardiac outcome and sternum T2 was found

in STEMI patients, but not further evaluated in mice. Here, the statistical power in the

(compared to patients) relative low n-numbered animal studies was too low to allow for meaningful conclusions. This the more, since experimental induction of MI in mice results in very similar individual infarct sizes (compared to the broad range in humans), which clearly hampers significant correlation analyses. For this, additional studies with modified ischemia/reperfusion times to induce differential cardiac injury would be required.

4.6. Future directions

In light of the limitations discussed above, we wish to extend the present work with respect to the following:

- Increase patient numbers with other bone marrow compartments included.
- Further characterize the temporal contribution of sternum vs. long bones (and other hematopoietic niches) to the immune cell release after AMI.
- How best to combine inflammation markers and bone marrow relaxation time to create a predictive indicator for the outcome after myocardial infarction.
- Extend human study populations and investigate bone marrow properties in the context of other diseases.
- Modify animal models to map the diversity of the patient collectives.

In the future, I foresee the use of our MRI protocols for the assessment of bone marrow properties in patients to early guide clinical decision-making after cardiovascular events. Specifically, in STEMI patients the increase of sternum T2 might be used as a surrogate marker for the immune response after AMI to mitigate further damage via modification of ongoing inflammatory processes.

4.7. Conclusion

To address the role of the sternum after AMI, we investigated its tissue characteristics in STEMI patients and a murine model of reperfused AMI by non-invasive MRI. We demonstrate that in both species alterations in the MRI relaxation time T2 can serve as *in vivo* readout for the degree of emergency hematopoiesis in the sternum. In humans, we found the higher sternal T2 immediately after AMI and the larger its drop/recovery thereafter, the less the adverse remodeling – suggesting this drop as indicative for the temporal limitation of the inflammatory response preventing a detrimental overshoot. Experiments in mice showed that the T2 response after AMI is specific to the sternal bone marrow and is associated with a very early neutrophil release compared with the long bones. Furthermore, ^{19}F-labelling experiments corroborated the direct trafficking of sternal neutrophils into the infarcted myocardium.

Taken together, we provide first evidence for a heart-sternum axis after AMI by demonstrating the egress of neutrophils from the sternum into the acutely infarcted myocardium and revealed that intensity and timing of sternal emergency hematopoiesis are crucial for the healing process. Non-invasive visualization of this systemic signal could help develop new levels of precision medicine for immunomodulatory therapy of AMI. However, further investigations are required to further support this notion.

Bibliography

[1] Kaptoge S, Pennells L, De Bacquer D, et al. World Health Organization cardiovascular disease risk charts: revised models to estimate risk in 21 global regions. Lancet Glob Health 2019; 7: e1332–e1345.

[2] Timmis A, Townsend N, Gale CP, et al. European Society of Cardiology: Cardiovascular Disease Statistics 2019. Eur Heart J 2020; 41: 12–85.

[3] Bansilal S, Castellano JM, Fuster V. Global burden of CVD: focus on secondary prevention of cardiovascular disease. Int J Cardiol 2015; 201: S1–S7.

[4] Roth GA, Mensah GA, Johnson CO, et al. Global Burden of Cardiovascular Diseases and Risk Factors, 1990–2019. J Am Coll Cardiol 2020; 76: 2982–3021.

[5] He J, Liu D, Zhao L, et al. Myocardial ischemia/reperfusion injury: Mechanisms of injury and implications for management (Review). Exp Ther Med 2022; 23: 430.

[6] Hoffman JIE, Buckberg GD. The Myocardial Oxygen Supply:Demand Index Revisited. J Am Heart Assoc 2014; 3: e000285.

[7] Thygesen K, Alpert JS, Jaffe AS, et al. Third Universal Definition of Myocardial Infarction. Circulation 2012; 126: 2020–2035.

[8] Smilowitz NR, Redel-Traub G, Hausvater A, et al. Myocardial Injury After Noncardiac Surgery: A Systematic Review and Meta-Analysis. Cardiol Rev 2019; 27: 267–273.

[9] Sutton MGStJ, Sharpe N. Left Ventricular Remodeling After Myocardial Infarction: Pathophysiology and Therapy. Circulation 2000; 101: 2981–2988.

[10] Ambrose JA, Singh M. Pathophysiology of coronary artery disease leading to acute coronary syndromes. F1000Prime Rep; 7. Epub ahead of print 14 January 2015. DOI: 10.12703/P7-08.

[11] Libby P, Buring JE, Badimon L, et al. Atherosclerosis. Nat Rev Dis Primer 2019; 5: 56.

[12] Lusis AJ. Atherosclerosis. Nature 2000; 407: 233–241.

[13] Hansson GK, Hermansson A. The immune system in atherosclerosis. Nat Immunol 2011; 12: 204–212.

[14] Sciarra L, Golia P, Palamà Z, et al. Patients with left bundle branch block and left axis deviation show a specific left ventricular asynchrony pattern: Implications for left ventricular lead placement during CRT implantation. J Electrocardiol 2018; 51: 175–181.

[15] Brenner E, Pechriggl E, Zwierzina M, et al. Case report: a common trunk of the coronary arteries. Surg Radiol Anat 2017; 39: 455–459.

[16] Thygesen K, Alpert JS, Jaffe AS, et al. Fourth Universal Definition of Myocardial Infarction (2018). J Am Coll Cardiol 2018; 72: 2231–2264.

[17] McCarthy CP, Kolte D, Kennedy KF, et al. Patient Characteristics and Clinical Outcomes of Type 1 Versus Type 2 Myocardial Infarction. J Am Coll Cardiol 2021; 77: 848–857.

[18] Vogel B, Claessen BE, Arnold SV, et al. ST-segment elevation myocardial infarction. Nat Rev Dis Primer 2019; 5: 39.

[19] Lu L, Liu M, Sun R, et al. Myocardial Infarction: Symptoms and Treatments. Cell Biochem Biophys 2015; 72: 865–867.

[20] Kingma JG. Myocardial Infarction: An Overview of STEMI and NSTEMI Physiopathology and Treatment. World J Cardiovasc Dis 2018; 08: 498–517.

[21] Manari A, Varani E, Guastaroba P, et al. Long-term outcome in patients with ST segment elevation myocardial infarction and multivessel disease treated with culprit-only, immediate, or staged multivessel percutaneous revascularization strategies: Insights from the REAL registry: Acute Myocardial Infarction in Multivessel Disease. Catheter Cardiovasc Interv 2014; 84: 912–922.

[22] Cortell A, Sanchis J, Bodí V, et al. Non-ST-Elevation Acute Myocardial Infarction With Normal Coronary Arteries: Predictors and Prognosis. Rev Esp Cardiol Engl Ed 2009; 62: 1260–1266.

[23] Jeremias A. The utility of troponin measurement to detect myocardial infarction:

review of the current findings. Vasc Health Risk Manag 2010; 691.

[24] Thygesen K, Alpert JS, Jaffe AS, et al. Third universal definition of myocardial infarction. Eur Heart J 2012; 33: 2551–2567.

[25] Chiu A. Troponin-I, myoglobin, and mass concentration of creatine kinase-MB in acute myocardial infarction. QJM 1999; 92: 711–718.

[26] Ibanez B, James S, Agewall S, et al. 2017 ESC Guidelines for the management of acute myocardial infarction in patients presenting with ST-segment elevation. Eur Heart J 2018; 39: 119–177.

[27] Cervellin G, Rastelli G. The clinics of acute coronary syndrome. Ann Transl Med 2016; 4: 191–191.

[28] Henrikson CA, Howell EE, Bush DE, et al. Chest Pain Relief by Nitroglycerin Does Not Predict Active Coronary Artery Disease. Ann Intern Med 2003; 139: 979.

[29] Aldous SJ. Cardiac biomarkers in acute myocardial infarction. Int J Cardiol 2013; 164: 282–294.

[30] Beamish D, Maniuk T, Mukarram M, et al. Role of Creatine Kinase in the Troponin Era: A Systematic Review. West J Emerg Med 2021; 22: 1291–1294.

[31] Vanhaverbeke M, Veltman D, Pattyn N, et al. C-reactive protein during and after myocardial infarction in relation to cardiac injury and left ventricular function at follow-up. Clin Cardiol 2018; 41: 1201–1206.

[32] Legger GE, Dermer CWE, Brunger AF, et al. The relation between C-reactive protein and serum amyloid A in patients with autoinflammatory diseases. Pediatr Rheumatol 2022; 20: 106.

[33] Tapp LD, Shantsila E, Wrigley BJ, et al. TLR4 expression on monocyte subsets in myocardial infarction. J Intern Med 2013; 273: 294–305.

[34] Blanken AB, Agca R, Van Sijl AM, et al. Arterial wall inflammation in rheumatoid arthritis is reduced by anti-inflammatory treatment. Semin Arthritis Rheum 2021; 51: 457–463.

[35] Harjunpää H, Llort Asens M, Guenther C, et al. Cell Adhesion Molecules and Their

Roles and Regulation in the Immune and Tumor Microenvironment. Front Immunol 2019; 10: 1078.

[36] Pollack A, Kontorovich AR, Fuster V, et al. Viral myocarditis—diagnosis, treatment options, and current controversies. Nat Rev Cardiol 2015; 12: 670–680.

[37] Salvatici M, Cardinale D, Colombo A, et al. Cancer Cardiotoxicity and Cardiac Biomarkers. In: Preedy VR, Patel VB (eds) Biomarkers in Cancer. Dordrecht: Springer Netherlands, pp. 73–105.

[38] Cardinale D, Ciceri F, Latini R, et al. Anthracycline-induced cardiotoxicity: A multicenter randomised trial comparing two strategies for guiding prevention with enalapril: The International CardioOncology Society-one trial. Eur J Cancer 2018; 94: 126–137.

[39] Cardinale D, Cipolla CM. Chemotherapy-induced cardiotoxicity: importance of early detection. Expert Rev Cardiovasc Ther 2016; 14: 1297–1299.

[40] Cardinale D, Sandri MT. Detection and monitoring of cardiotoxicity by using biomarkers: Pros and cons. Prog Pediatr Cardiol 2015; 39: 77–84.

[41] Walker HK, Hall WD, Hurst JW (eds). Clinical Methods: The History, Physical, and Laboratory Examinations. 3rd ed. Boston: Butterworths, http://www.ncbi.nlm.nih.gov/books/NBK201/ (1990, accessed 28 July 2023).

[42] Savarese G, Becher PM, Lund LH, et al. Global burden of heart failure: a comprehensive and updated review of epidemiology. Cardiovasc Res 2023; 118: 3272–3287.

[43] Pfeffer MA, Braunwald E. Ventricular remodeling after myocardial infarction. Experimental observations and clinical implications. Circulation 1990; 81: 1161–1172.

[44] Bouredji Z, Argaw A, Frenette J. The inflammatory response, a mixed blessing for muscle homeostasis and plasticity. Front Physiol 2022; 13: 1032450.

[45] Swirski FK, Nahrendorf M. Cardioimmunology: the immune system in cardiac homeostasis and disease. Nat Rev Immunol 2018; 18: 733–744.

[46] Bönner F, Gastl M, Nienhaus F, et al. Regional analysis of inflammation and

contractile function in reperfused acute myocardial infarction by in vivo 19F cardiovascular magnetic resonance in pigs. Basic Res Cardiol 2022; 117: 21.

[47] Stumpf C, Sheriff A, Zimmermann S, et al. C-reactive protein levels predict systolic heart failure and outcome in patients with first ST-elevation myocardial infarction treated with coronary angioplasty. Arch Med Sci 2017; 5: 1086–1093.

[48] Weiss L. The structure of bone marrow. Functional interrelationships of vascular and hematopoietic compartments in experimental hemolytic anemia: An electron microscopic study. J Morphol 1965; 117: 467–537.

[49] Psaila B, Lyden D, Roberts I. Megakaryocytes, malignancy and bone marrow vascular niches. J Thromb Haemost 2012; 10: 177–188.

[50] Kopp H-G, Avecilla ST, Hooper AT, et al. The Bone Marrow Vascular Niche: Home of HSC Differentiation and Mobilization. Physiology 2005; 20: 349–356.

[51] Lucas D, Salomonis N, Grimes HL. Unraveling bone marrow architecture. Nat Cell Biol 2020; 22: 5–6.

[52] Loder BF, Mutschler B, Ray RJ, et al. B Cell Development in the Spleen Takes Place in Discrete Steps and Is Determined by the Quality of B Cell Receptor–Derived Signals. J Exp Med 1999; 190: 75–90.

[53] Sitnicka E. From the Bone Marrow to the Thymus: The Road Map of Early Stages of T-Cell Development. Crit Rev Immunol 2009; 29: 487–530.

[54] Gang EJ, Bosnakovski D, Figueiredo CA, et al. SSEA-4 identifies mesenchymal stem cells from bone marrow. Blood 2007; 109: 1743–1751.

[55] Hardouin P, Pansini V, Cortet B. Bone marrow fat. Joint Bone Spine 2014; 81: 313–319.

[56] Kim SC, Krynyckyi BR, Machac J, et al. Patterns of Red Marrow in the Adult Femur. Clin Nucl Med 2006; 31: 739–741.

[57] Gonzalez FM, Mitchell J, Monfred E, et al. Knee MRI patterns of bone marrow reconversion and relationship to anemia. Acta Radiol 2016; 57: 964–970.

[58] Travlos GS. Histopathology of Bone Marrow. Toxicol Pathol 2006; 34: 566–598.

[59] Itkin T, Gur-Cohen S, Spencer JA, et al. Distinct bone marrow blood vessels differentially regulate haematopoiesis. Nature 2016; 532: 323–328.

[60] Heidt T, Sager HB, Courties G, et al. Chronic variable stress activates hematopoietic stem cells. Nat Med 2014; 20: 754–758.

[61] Da Silva EZM, Jamur MC, Oliver C. Mast Cell Function: A New Vision of an Old Cell. J Histochem Cytochem 2014; 62: 698–738.

[62] Kondo M. Lymphoid and myeloid lineage commitment in multipotent hematopoietic progenitors: Roles of bone marrow microenvironment. Immunol Rev 2010; 238: 37–46.

[63] Zhao E, Xu H, Wang L, et al. Bone marrow and the control of immunity. Cell Mol Immunol 2012; 9: 11–19.

[64] A multiscale model of the bone marrow and hematopoiesis. Math Biosci Eng 2011; 8: 643–658.

[65] Kricun ME. Red-yellow marrow conversion: Its effect on the location of some solitary bone lesions. Skeletal Radiol 1985; 14: 10–19.

[66] Gurevitch O, Slavin S, Feldman AG. Conversion of red bone marrow into yellow – Cause and mechanisms. Med Hypotheses 2007; 69: 531–536.

[67] Muguruma Y, Yahata T, Miyatake H, et al. Reconstitution of the functional human hematopoietic microenvironment derived from human mesenchymal stem cells in the murine bone marrow compartment. Blood 2006; 107: 1878–1887.

[68] O'Malley DP, Smith L, Fedoriw Y. Benign Causes of Bone Marrow Abnormalities Including Infections, Storage Diseases, Systemic Disorders, and Stromal Changes. In: Hematopathology. Elsevier, pp. 184-209.e1.

[69] Poulton TB, Murphy WD, Duerk JL, et al. Bone marrow reconversion in adults who are smokers: MR Imaging findings. Am J Roentgenol 1993; 161: 1217–1221.

[70] Arbabi A. A quantitative analysis of the structure of human sternum. J Med Phys 2009; 34: 80.

[71] Jena S, Chawla S. The Anatomy and Physiology of Laboratory Mouse. In: Nagarajan

P, Gudde R, Srinivasan R (eds) Essentials of Laboratory Animal Science: Principles and Practices. Singapore: Springer Singapore, pp. 159–185.

[72] Kaushansky K. Lineage-Specific Hematopoietic Growth Factors. N Engl J Med 2006; 354: 2034–2045.

[73] Veldhuis-Vlug AG, Rosen CJ. Clinical implications of bone marrow adiposity. J Intern Med 2018; 283: 121–139.

[74] Ito K, Ito K. Metabolism and the Control of Cell Fate Decisions and Stem Cell Renewal. Annu Rev Cell Dev Biol 2016; 32: 399–409.

[75] Rossi DJ, Jamieson CHM, Weissman IL. Stems Cells and the Pathways to Aging and Cancer. Cell 2008; 132: 681–696.

[76] Herisson F, Frodermann V, Courties G, et al. Direct vascular channels connect skull bone marrow and the brain surface enabling myeloid cell migration. Nat Neurosci 2018; 21: 1209–1217.

[77] Swirski FK, Nahrendorf M. Leukocyte Behavior in Atherosclerosis, Myocardial Infarction, and Heart Failure. Science 2013; 339: 161–166.

[78] Jickling GC, Liu D, Ander BP, et al. Targeting Neutrophils in Ischemic Stroke: Translational Insights from Experimental Studies. J Cereb Blood Flow Metab 2015; 35: 888–901.

[79] Iadecola C. Brain-Immune Interactions and Ischemic Stroke: Clinical Implications. Arch Neurol 2012; 69: 576.

[80] Courties G, Moskowitz MA, Nahrendorf M. The Innate Immune System After Ischemic Injury: Lessons to Be Learned From the Heart and Brain. JAMA Neurol 2014; 71: 233.

[81] Offner H, Subramanian S, Parker SM, et al. Experimental Stroke Induces Massive, Rapid Activation of the Peripheral Immune System. J Cereb Blood Flow Metab 2006; 26: 654–665.

[82] Tschöpe C, Müller I, Xia Y, et al. NOD2 (Nucleotide-Binding Oligomerization Domain 2) Is a Major Pathogenic Mediator of Coxsackievirus B3-Induced Myocarditis. Circ Heart Fail 2017; 10: e003870.

[83] Miteva K, Pappritz K, Sosnowski M, et al. Mesenchymal stromal cells inhibit NLRP3 inflammasome activation in a model of Coxsackievirus B3-induced inflammatory cardiomyopathy. Sci Rep 2018; 8: 2820.

[84] Huang C-H, Vallejo JG, Kollias G, et al. Role of the Innate Immune System in Acute Viral Myocarditis. Basic Res Cardiol 2009; 104: 228–237.

[85] Nahrendorf M, Swirski FK. Monocyte and Macrophage Heterogeneity in the Heart. Circ Res 2013; 112: 1624–1633.

[86] Liu P, Aitken K, Kong Y-Y, et al. The tyrosine kinase p56lck is essential in coxsackievirus B3-mediated heart disease. Nat Med 2000; 6: 429–434.

[87] Shi Y, Fukuoka M, Li G, et al. Regulatory T Cells Protect Mice Against Coxsackievirus-Induced Myocarditis Through the Transforming Growth Factor β–Coxsackie-Adenovirus Receptor Pathway. Circulation 2010; 121: 2624–2634.

[88] Baldeviano GC, Barin JG, Talor MV, et al. Interleukin-17A Is Dispensable for Myocarditis but Essential for the Progression to Dilated Cardiomyopathy. Circ Res 2010; 106: 1646–1655.

[89] Van Den Brink H, Doubal FN, Duering M. Advanced MRI in cerebral small vessel disease. Int J Stroke 2023; 18: 28–35.

[90] Małkiewicz A, Dziedzic M. Rekonwersja szpiku – obrazowanie fizjologicznych zmian szpiku w codziennej praktyce. Pol J Radiol 2012; 77: 45–50.

[91] Grønningsæter IS, Ahmed AB, Vetti N, et al. Bone Marrow Abnormalities Detected by Magnetic Resonance Imaging as Initial Sign of Hematologic Malignancies. Clin Pract 2018; 8: 1061.

[92] Małkiewicz A, Dziedzic M. Bone marrow reconversion - imaging of physiological changes in bone marrow. Pol J Radiol. 2012 Oct;77(4):45-50. doi: 10.12659/pjr.883628. PMID: 23269936; PMCID: PMC3529711.

[93] Ríos-Navarro C, Gavara J, Núñez J, et al. EpCAM and microvascular obstruction in patients with STEMI: a cardiac magnetic resonance study. Rev Esp Cardiol Engl Ed 2022; 75: 384–391.

[94] Panopoulos S, Mavrogeni S, Vlachopoulos C, et al. Cardiac magnetic resonance

imaging before and after therapeutic interventions for systemic sclerosis-associated myocarditis. Rheumatology 2023; 62: 1535–1542.

[95] O'Brien AT, Gil KE, Varghese J, et al. T2 mapping in myocardial disease: a comprehensive review. J Cardiovasc Magn Reson 2022; 24: 33.

[96] Tang R, Tang G, Hua T, et al. mDIXON-Quant technique diagnostic accuracy for assessing bone mineral density in male adult population. BMC Musculoskelet Disord 2023; 24: 125.

[97] Kaolawanich Y, Azevedo CF, Kim HW, et al. Native T1 Mapping for the Diagnosis of Myocardial Fibrosis in Patients With Chronic Myocardial Infarction. JACC Cardiovasc Imaging 2022; 15: 2069–2079.

[98] Reyngoudt H, Baudin P, Carlier PG, et al. New Insights into the Spread of MRS - Based Water T2 Values Observed in Highly Fatty Replaced Muscles. J Magn Reson Imaging 2023; jmri.28669.

[99] Piechnik SK, Ferreira VM, Lewandowski AJ, et al. Normal variation of magnetic resonance T1 relaxation times in the human population at 1.5 T using ShMOLLI. J Cardiovasc Magn Reson 2013; 15: 13.

[100] Jo Y, Kim J, Park CH, et al. Guideline for Cardiovascular Magnetic Resonance Imaging from the Korean Society of Cardiovascular Imaging—Part 1: Standardized Protocol. Korean J Radiol 2019; 20: 1313.

[101] Mewton N, Liu CY, Croisille P, et al. Assessment of Myocardial Fibrosis With Cardiovascular Magnetic Resonance. J Am Coll Cardiol 2011; 57: 891–903.

[102] Radunski UK, Lund GK, Stehning C, et al. CMR in Patients With Severe Myocarditis. JACC Cardiovasc Imaging 2014; 7: 667–675.

[103] Moon JC, Messroghli DR, Kellman P, et al. Myocardial T1 mapping and extracellular volume quantification: a Society for Cardiovascular Magnetic Resonance (SCMR) and CMR Working Group of the European Society of Cardiology consensus statement. J Cardiovasc Magn Reson 2013; 15: 92.

[104] Piechnik SK, Ferreira VM, Dall'Armellina E, et al. Shortened Modified Look-Locker Inversion recovery (ShMOLLI) for clinical myocardial T1-mapping at 1.5

and 3 T within a 9 heartbeat breathhold. J Cardiovasc Magn Reson 2010; 12: 69.

[105] Chow K, Flewitt JA, Green JD, et al. Saturation recovery single-shot acquisition (SASHA) for myocardial T 1 mapping: SASHA for T 1 Mapping. Magn Reson Med 2014; 71: 2082–2095.

[106] Messroghli DR, Greiser A, Fröhlich M, et al. Optimization and validation of a fully-integrated pulse sequence for modified look-locker inversion-recovery (MOLLI) T1 mapping of the heart. J Magn Reson Imaging 2007; 26: 1081–1086.

[107] Hardy PA, Henkelman RM, Bishop JE, et al. Why fat is bright in rare and fast spin-echo imaging. J Magn Reson Imaging 1992; 2: 533–540.

[108] Dixon WT. Simple proton spectroscopic imaging. Radiology 1984; 153: 189–194.

[109] Eggers H, Brendel B, Duijndam A, et al. Dual-echo Dixon imaging with flexible choice of echo times: Dual-Echo Dixon Imaging. Magn Reson Med 2011; 65: 96–107.

[110] Ma J. Dixon techniques for water and fat imaging. J Magn Reson Imaging 2008; 28: 543–558.

[111] Huijgen WHF, Van Rijswijk CSP, Bloem JL. Is fat suppression in T1 and T2 FSE with mDixon superior to the frequency selection-based SPAIR technique in musculoskeletal tumor imaging? Skeletal Radiol 2019; 48: 1905–1914.

[112] Day RA, Estabrook DA, Wu C, et al. Systematic Study of Perfluorocarbon Nanoemulsions Stabilized by Polymer Amphiphiles. ACS Appl Mater Interfaces 2020; 12: 38887–38898.

[113] Wu L, Liu F, Liu S, et al. Perfluorocarbons-Based 19F Magnetic Resonance Imaging in Biomedicine. Int J Nanomedicine 2020; Volume 15: 7377–7395.

[114] Grapentin C, Barnert S, Schubert R. Monitoring the Stability of Perfluorocarbon Nanoemulsions by Cryo-TEM Image Analysis and Dynamic Light Scattering. PLOS ONE 2015; 10: e0130674.

[115] Mühle J, Ganesan AL, Miller BR, et al. Perfluorocarbons in the global atmosphere: tetrafluoromethane, hexafluoroethane, and octafluoropropane. Atmospheric Chem Phys 2010; 10: 5145–5164.

[116] Rodrigues RM, Guan X, Iñiguez JA, et al. Perfluorocarbon nanoemulsion promotes the delivery of reducing equivalents for electricity-driven microbial CO2 reduction. Nat Catal 2019; 2: 407–414.

[117] Güden-Silber T, Temme S, Jacoby C, et al. Biomedical 19F MRI Using Perfluorocarbons. In: García Martín ML, López Larrubia P (eds) Preclinical MRI. New York, NY: Springer New York, pp. 235–257.

[118] Krafft MP, Riess JG. Chemistry, Physical Chemistry, and Uses of Molecular Fluorocarbon−Hydrocarbon Diblocks, Triblocks, and Related Compounds—Unique "Apolar" Components for Self-Assembled Colloid and Interface Engineering. Chem Rev 2009; 109: 1714–1792.

[119] Holland GN, Bottomley PA, Hinshaw WS. 19F magnetic resonance imaging. J Magn Reson 1969 1977; 28: 133–136.

[120] Bulte JWM. Hot spot MRI emerges from the background. Nat Biotechnol 2005; 23: 945–946.

[121] Ye Y-X, Basse-Lüsebrink TC, Arias-Loza P-A, et al. Monitoring of Monocyte Recruitment in Reperfused Myocardial Infarction With Intramyocardial Hemorrhage and Microvascular Obstruction by Combined Fluorine 19 and Proton Cardiac Magnetic Resonance Imaging. Circulation 2013; 128: 1878–1888.

[122] Balducci A, Wen Y, Zhang Y, et al. A novel probe for the non-invasive detection of tumor-associated inflammation. OncoImmunology 2013; 2: e23034.

[123] Van Heeswijk RB, Pellegrin M, Flögel U, et al. Fluorine MR Imaging of Inflammation in Atherosclerotic Plaque in Vivo. Radiology 2015; 275: 421–429.

[124] Eitel I, De Waha S, Wöhrle J, et al. Comprehensive Prognosis Assessment by CMR Imaging After ST-Segment Elevation Myocardial Infarction. J Am Coll Cardiol 2014; 64: 1217–1226.

[125] Eitel I, Desch S, Fuernau G, et al. Prognostic Significance and Determinants of Myocardial Salvage Assessed by Cardiovascular Magnetic Resonance in Acute Reperfused Myocardial Infarction. J Am Coll Cardiol 2010; 55: 2470–2479.

[126] Reindl LM, Albinger N, Bexte T, et al. Immunotherapy with NK cells: recent

developments in gene modification open up new avenues. OncoImmunology 2020; 9: 1777651.

[127] Ding Z, Tan K, Alter C, et al. Cardiac injection of USSC boosts remuscularization of the infarcted heart by shaping the T-cell response. J Mol Cell Cardiol 2023; 175: 29–43.

[128] Hermann S, Kuhlmann MT, Starsichova A, et al. Imaging Reveals the Connection Between Spontaneous Coronary Plaque Ruptures, Atherothrombosis, and Myocardial Infarctions in HypoE/SRBI −/− Mice. J Nucl Med 2016; 57: 1420–1427.

[129] Zhang S, Picard MH, Vasile E, et al. Diet-Induced Occlusive Coronary Atherosclerosis, Myocardial Infarction, Cardiac Dysfunction, and Premature Death in Scavenger Receptor Class B Type I-Deficient, Hypomorphic Apolipoprotein ER61 Mice. Circulation 2005; 111: 3457–3464.

[130] Temme S, Grapentin C, Quast C, et al. Noninvasive Imaging of Early Venous Thrombosis by 19 F Magnetic Resonance Imaging With Targeted Perfluorocarbon Nanoemulsions. Circulation 2015; 131: 1405–1414.

[131] Gantert M, Lewrick F, Adrian JE, et al. Receptor-Specific Targeting with Liposomes In Vitro Based on Sterol-PEG1300 Anchors. Pharm Res 2009; 26: 529–538.

[132] Wang X, Temme S, Grapentin C, et al. Fluorine-19 Magnetic Resonance Imaging of Activated Platelets. J Am Heart Assoc 2020; 9: e016971.

[133] Heijman E, De Graaf W, Niessen P, et al. Comparison between prospective and retrospective triggering for mouse cardiac MRI. NMR Biomed 2007; 20: 439–447.

[134] Coolen BF, Geelen T, Paulis LEM, et al. Three-dimensional T 1 mapping of the mouse heart using variable flip angle steady-state MR imaging: 3D T 1 MAPPING OF THE MOUSE HEART. NMR Biomed 2011; 24: 154–162.

[135] Haberkorn SM, Jacoby C, Ding Z, et al. Cardiovascular Magnetic Resonance Relaxometry Predicts Regional Functional Outcome After Experimental Myocardial Infarction. Circ Cardiovasc Imaging 2017; 10: e006025.

[136] Bönner F, Jacoby C, Temme S, et al. Multifunctional MR monitoring of the healing process after myocardial infarction. Basic Res Cardiol 2014; 109: 430.

[137] Ebner B, Behm P, Jacoby C, et al. Early Assessment of Pulmonary Inflammation by 19 F MRI In Vivo. Circ Cardiovasc Imaging 2010; 3: 202–210.

[138] Flögel U, Temme S, Jacoby C, et al. Multi-targeted 1H/19F MRI unmasks specific danger patterns for emerging cardiovascular disorders. Nat Commun 2021; 12: 5847.

[139] Martínez VB, González-Juanatey JR. Markers of Inflammation and Cardiovascular Disease: Clinical Applications of C-Reactive Protein Determination. Am J Cardiovasc Drugs 2009; 9: 3–7.

[140] Sandoval Y, Apple FS, Mahler SA, et al. High-Sensitivity Cardiac Troponin and the 2021 AHA/ACC/ASE/CHEST/SAEM/SCCT/SCMR Guidelines for the Evaluation and Diagnosis of Acute Chest Pain. Circulation 2022; 146: 569–581.

[141] Bouvain P, Ding Z, Kadir S, et al. Non-invasive mapping of systemic neutrophil dynamics upon cardiovascular injury. Nat Cardiovasc Res 2023; 2: 126–143.

[142] Bönner F, Jung C, Polzin A, et al. SYSTEMI - systemic organ communication in STEMI: design and rationale of a cohort study of patients with ST-segment elevation myocardial infarction. BMC Cardiovasc Disord 2023; 23: 232.

[143] Altehoefer C, Schmid A, Büchert M, et al. Characterization of hematopoietic bone marrow in male professional cyclists by magnetic resonance imaging of the lumbar spine: Lumbar MRI in Male Professional Cyclists. J Magn Reson Imaging 2002; 16: 284–288.

[144] Getz GS, Reardon CA. Animal models of atherosclerosis. Arterioscler Thromb Vasc Biol 2012; 32: 1104–1115.

[145] Stähli BE, Klingenberg R, Heg D, et al. Mammalian target of rapamycin inhibition in patients with ST-segment elevation myocardial infarction. J Am Coll Cardiol 2022; 80: 1802–1814.

[146] Pinho S, Frenette PS. Haematopoietic stem cell activity and interactions with the niche. Nat Rev Mol Cell Biol 2019; 20: 303–320.

[147] Kruger P, Saffarzadeh M, Weber ANR, et al. Neutrophils: Between Host Defence, Immune Modulation, and Tissue Injury. PLOS Pathog 2015; 11: e1004651.

[148] Shi Y, Leak RK, Keep RF, et al. Translational Stroke Research on Blood-Brain

Barrier Damage: Challenges, Perspectives, and Goals. Transl Stroke Res 2016; 7: 89–92.

[149] Bouvain P, Ding Z, Kadir S, et al. Non-invasive mapping of systemic neutrophil dynamics upon cardiovascular injury. Nat Cardiovasc Res 2023; 2: 126–143.

[150] Gross S, Gammon ST, Moss BL, et al. Bioluminescence imaging of myeloperoxidase activity in vivo. Nat Med 2009; 15: 455–461.

[151] Wu M, Zhang H, Tie C, et al. MR imaging tracking of inflammation-activatable engineered neutrophils for targeted therapy of surgically treated glioma. Nat Commun 2018; 9: 4777.

[152] Jugdutt BI, Dhalla NS. Cardiac remodeling: molecular mechanisms. New York: Springer, 2013.

Special Thanks

Now I would like to thank everyone who supported me in the preparation of this work.

First and foremost, I would like to thank Prof. Dr. Ulrich Flögel and Prof. Dr. med. Florian Bönner for the years of support, the inspiration and the always valuable tips and advice.

I thank the Institute for experimental cardiovascular imaging and molecular cardiology by Prof. Dr Ulrich Flöge, making the work possible. Many thanks to the staff at the institute. In particular, I would like to thank all for the help, good training in the laboratory and the support with the animal work.

My greatest thanks go to my wife and family. Thank you from the bottom of my heart for your constant support, encouragement and confidence.